COMPUTATIONAL STUDY OF NEMS SWITCHES BASED ON GRAPHENE MATERIALS

A Thesis

Submitted in partial fulfillment of the requirements for the award of the degree of

DOCTOR OF PHILOSOPHY

in

Electronics and Communication Engineering

By

Rekha Chaudhary

11719574

Supervised By

Dr. Prasantha R. Mudimela

LOVELY PROFESSIONAL UNIVERSITY
PUNJAB
2021

DECLARATION

I hereby declare that the thesis entitled "Computational Study of NEMS Switches Based on Graphene Materials" is submitted by me for the Degree of Doctor of Philosophy in Electronics and Communication Engineering is the result of my original and independent research work carried out under the guidance of Dr. Prasantha R. Mudimela, Associate Professor, Lovely Professional University, Punjab. It has not been submitted for the award of any degree, diploma, associateship, fellowship of any University or Institution.

Place: Phagwara

Date:

Signature of the Candidate

CERTIFICATE

This thesis entitled "Computational Study of NEMS Switches Based on Graphene Materials" submitted by Rekha Chaudhary of Lovely Professional University is a record of bona fide research work done by her and it has not been submitted for the award of any degree, diploma, associateship, fellowship of any University/Institution.

Place: Phagwara

Date:

Signature of the Guide

ABSTRACT

Low pull-in voltage and good radio frequency (RF) performance are the key design parameters for the RF NEMS switch. The thesis work proposes design and modelling of graphene materials-based RF NEMS switch.

Firstly, the finite element modelling (FEM) of graphene oxide (GO) as fixed-fixed beam structure in NEMS switch have been performed for the first time. The analysis of different performance parameters has investigated for standard and perforated switch structures to ensure the mechanical reliability. The reduction in the actuation voltage and von Mises stress have observed by using perforated beam.

Secondly, the RF analysis of Graphene-GO based NEMS shunt switch has evaluated. The RF performance analysis has performed for both monolayer and multilayer GO beam along with graphene electrode. It is evident from the results that monolayer GO needs low pull-in voltage, acquires high downstate capacitance, and high switching speed. Nevertheless, multilayer GO also shows improved RF performance with high switching speed. On the other hand, design and analysis of the different bridge structures-based graphene NEMS switch have studied to identify that which bridge structure requires least pull-in voltage. The results show that different bridges have different spring stiffness, get actuated at different actuation voltages and hinge structure bridge requires least pull-in voltage. Also, analysis of hinge structure-based GO NEMS switch has been carried for different design parameters. The design parameters of NEMS switch have been varied and again the bridge dimensions with least pull-in voltage have investigated. Moreover, the performance of the switch structure that exhibits minimum pull-in voltage at RF was evaluated. The results state that actuation voltage and von Mises stress exhibit a negative correlation with beam length and positive correlation with beam thickness and air gap. Furthermore, a long and thin suspended beam requires low actuation voltage and undergoes less von Mises stress. The intense effect of von Mises stress occurs at beam edges, perforation corners, and beam-top electrode interface due to edge termination effect. The results demonstrate that GO provides low pull-in voltage, withstands low von Mises stress and good RF performance. These benefits make GO a better choice for beam material in RF NEMS switch.

Also, the comparison between the performance analysis of graphene and graphene derivative-based NEMS switch has studied. The effect of manipulating the beam length and reduction in elastic modulus on pull-in voltage has presented in the study. It has been found that reduction in elastic modulus lower the actuation voltage without much fall in restoring force than increasing the beam length. Moreover, the finite element analysis (FEA) of single material beam (graphene), and composite beams (graphene/RGO, graphene/GO) has performed. The composite beam has less Young's modulus in comparison with single beam. This in turn yields lower pull-in voltage than single beam. Based on the study, it can be concluded that composite beam concept is a good choice to reduce both elastic modulus and pull-in voltage.

Finally, from application perspective, universal logic gates NAND and NOR along with NOT and XOR are successfully implemented using graphene cantilever structures. The very high electrical conductivity makes graphene a good choice as cantilever beam for this work. The designed graphene cantilever actuates at very low voltage and possesses high switching speed. The simulated logic gates could enable to implement different digital circuits using cantilever switches.

So, in this research work graphene materials based NEMS shunt switches have been modelled and verified. It has been found that proposed switch exhibits low pull-in voltage, undergoes less von Mises stress, high switching speed, and good RF performance as compared to existing switch structures. Furthermore, different digital logic gates with high switching speed have successfully implemented using proposed switch structures.

Keywords: GO, RGO, Graphene, Nanoelectromechanical systems (NEMS), RF NEMS switch, S-parameters, Hinge structure, Digital logic gates, FEM

ACKNOWLEDGEMENT

First and foremost, I am thankful to almighty for making things possible at the right time. I owe my success to my supervisor and would like to sincerely thank Dr. Prasantha R. Mudimela for his guidance. I greatly appreciate his support, positive attitude, and his vast knowledge in a wide range of topics. His guidance not only in terms of giving ideas and solving research problems, but also in terms of giving freedom to do research in my own ways has proved to be useful and invaluable. I am deeply influenced by my supervisor's way of guidance and sincerely thankful for standing by my side in tough times.

I would like to thank my husband Mahender Singh Kaswan, for his unconditional love, support and encouragement. Last but not least, I would like to thank my family (especially my father, Mr. Maan Singh) and my friends for their continuous love and support.

Finally, special thanks to all the people who helped me in direct and indirect ways to accomplish this work.

TABLE OF CONTENTS

DECLARATION……………………………………………………………………II

CERTIFICATE…………………………………………………………………..III

ABSTRACT ……………………………………………………………………...IV-V

ACKNOWLEDGEMENT…………………………………………………….VI

TABLE OF CONTENTS………………………………………………….VII-X

LIST OF TABLES……………………………………………………………..XI

LIST OF FIGURES………………………………………………………..XII-XIV

LIST OF ABBREVATIONS…………………………………………………XV

CHAPTER 1: INTRODUCTION……..…………………………………1-16

1.1 Need of new material……………………………………………………….1

1.2 RF MEMS switches…………………………………………………………...2

1.3 RF MEMS switch mechanism………………………………………………...3

1.4 Basic operating principle……………………………………………………...4

1.5 RF MEMS switch structures………………………………………………….4

1.5.1 Series contact type…………………………………………5

1.5.2 Shunt capacitive type……………………………………...5

1.6 Electromagnetic modelling of MEMS switch…………………………………6

1.6.1 MEMS shunt capacitive switch description……………….7

1.7 MEMS switch design parameters……………………………………………..8

1.7.1 Pull-in voltage……………………………….................8

1.7.2 von Mises stress…………………………………………...8

1.7.3 MEMS capacitance………………………………………..9

1.7.4 Series resistance…………………………………………...9

1.7.5 Inductance………………………………………………..10

1.7.6 S-parameters……………………………………………..10

1.7.7 Eigenfrequency Analysis………………………………...11

1.8 Methods to reduce pull-in voltage…………………………………………...12

1.8.1 Use of low spring constant structures……………………12

1.8.2 Change the device dimensions…………………………...13

1.8.3 Other materials with low elastic modulus………………..13

1.9 NEMS switch……………………………………………………………...13
1.9.1 Graphene oxide………………………………………..14
1.9.2 Reduced Graphene oxide ……………………………...14
1.10 Thesis outline……………………………………………………………15

CHAPTER 2: LITERATURE SURVEY………………………………...…….17-36

2.1 Different actuation mechanism-based RF MEMS switch……………………17
2.2 Low spring constant structures-based RF MEMS switch…………………...20
2.3 High K dielectric based RF MEMS switch…………………………………25
2.4 Fabrication processes-based RF MEMS switch……………………………..27
2.5 RF MEMS switches developed for specific bands…………………………..30
2.6 Development of NEMS switches…………………………………………….31
2.7 Research Gaps………………………………………………………………35
2.8 Problem formulation………………………………………………………...36

CHAPTER 3: FEM MODELLING OF GO BASED NEMS SWITCH…..….37-51

3.1 Device Geometry Description of double clamped GO-Graphene…………..37
3.1.1 Pull-in analysis………………………………………..38
3.1.2 FEM simulations of GO-based NEMS switch..…………39
3.2 Results and Discussions……………………………………………………..41
3.2.1 Standard and perforated beam structure……………….…41
3.3 Device Geometry Description of double clamped GO-Gold……………….46
3.4 Results and Discussions…………………………………………………….48
3.5 Summary……………………………………………………………………51

CHAPTER 4: RF ANALYSIS OF G/GO BASED NEMS SWITCH……….52-57

4.1 RF NEMS switch……………………………………………………………52
4.2 Design parameters…………………………………………………………...52
4.3 FEA of GO-based NEMS switch…………………………………………….54

4.4 Eigenfrequency analysis and actuation speed……………………………….54
4.5 S-parameters……………………………………………………………………55
4.6 Summary…………………………………………………………………….56

CHAPTER 5: NEMS SWITCH WITH DIFFERENT BRDIGE STRUCTURES……………………………………………………………..58-61

5.1 Different bridge structures……………………………………………………..58
5.2 Results and discussion…………………………………………………………59
5.3 Summary……………………………………………………………………….61

CHAPTER 6: OPTIMIZATION OF DESIGN PARAMETERS…………….62-69

6.1 Geometrical description of NEMS switch…………………………………..62
6.2 Effect of different parameters……………………………………………63
6.2.1 Suspended beam length…………………………………………63
6.2.2 Suspended beam thickness………………………………………63
6.2.3 Air gap………………………………………………………………...63
6.3 Results and Discussion……………………………………………………….64
6.4 von Mises stress analysis…………………………………………………66
6.5 Eigenfrequency Analysis……………………………………………………..68
6.6 RF Performance analysis……………………………………………………..68
6.7 Summary……………………………………………………………………...69

CHAPTER 7: GRAPHENE DERIVATIVE BASED COMPOSITE BEAM NEMS SWITCHES...70-83

7.1 Background…………………………………………………………………70
7.2 Selection of Suspended beam Material……………………………………...71
7.3 Analysis of Single material double clamped beam…………………………71
7.4 FEA of proposed structure…………………………………………………..72
7.5 Analysis of Graphene/RGO Composite beam………………………………75
7.6 Analysis of Graphene/GO Composite beam………………………………...76
7.7 Modal analysis of single material beam and composite beams……………..77
7.8 Summary……………………………………………………………………82

CHAPTER 8: GRAPHENE CANTILEVER BASED DIGITAL LOGIC GATES……………………………………………………………………..84-93

8.1 Background……………………………………………………………84

8.2 Device dimensions and operating principle…………………………………85

8.3 Logic gate implementation………………………………………………….86

8.3.1 NOT gate…………………………………………….86

8.3.2 NOR gate…………………………………………….87

8.3.3 NAND gate…………………………………………...88

8.3.4 XOR gate……………………………………………..89

8.4 Results and discussions……………………………………………………89

8.4.1 NOT gate implementation……………………………90

8.4.2 NOR gate implementation……………………………90

8.4.3 NAND gate implementation…………………………92

8.4.4 XOR gate implementation……………………………92

8.5 Switching speed……………………………………………………………..93

8.6 Summary…………………………………………………………………….93

CHAPTER 9: CONCLUSION AND FUTURE SCOPE……………….........94-98

9.1 Conclusion……………………………………………………….........94

9.2 Future scope………………………………………………………......97

BIBLIOGRAPHY……………………………………………………………...99-107

LIST OF PUBLICATIONS……………………………………………………108

LIST OF TABLES

1. Pull-in voltage for different actuation mechanisms…………………………..20
2. Different hinge structures……………………………………………………21
3. Other switch performance having different dimensions and different materials…………………………………………………………………...34
4. Dimensions of standard and perforated GO beam……………………………38
5. GO beam and electrode dimensions…………………………………………..48
6. Circularly perforated beam dimensions………..……………………………48
7. Obtained eigen frequencies……………………………………...………49
8. Dimensions of proposed switch………………………………………………53
9. Eigenfrequency analysis……………………………………………………...55
10. RF performance of simulated switch …………….………………………..56
11. NEMS switch device dimensions…………………………………………….59
12. Actuation voltage for different bridge structures……………………………..60
13. Suspended GO beam dimensions……………………………………..…...63
14. Dimensions of GO-based switch by varying different design parameters……65
15. von Mises stress analysis results for different design parameters……………67
16. Variation in performance parameters of single material graphene beam………………………………………………………………….…73
17. Variation in performance parameters by changing the Elastic Modulus………………………………………………………………………74
18. Single material beam and Composite beam performance parameters…………………………………………………………………79
19. Comparison of device performance parameters……………………………...82
20. Dimensions of graphene cantilever…………………………………………..85
21. Truth table of NOT gate………………………………………………………87
22. Truth table of NOR gate………………………………………………………88
23. Truth table of NAND gate……………………………………………………88
24. Truth table of XOR gate………………………………………………………89
25. Proposed switch comparison with existing work…………………………..96

LIST OF FIGURES

1. MEMS series contact switch (a) OFF state (b) ON state……………………..........5
2. MEMS shunt capacitive switch (a) ON state (b) OFF state……………………6
3. MEMS switch (a) Side view (b) Top view (c) CLR model of the switch configuration…………………………………………………………………...7
4. Perforated structure……………………………………………………...12
5. Various meander structures…………………………………………………...12
6. Schematic view of RF-MEMS switch with movable contact pad……………..22
7. Meander structure proposed……………………………………….........23
8. 3D view of helix spring structure MEMS switch ……………………………25
9. Working of Torsional bridge switch……………………………….............29
10. Simplified figure of GO NEMS switch………………………………………38
11. Top view of perforated GO beam…………………………………..............38
12. Basic steps of finite element method………………………………………….39
13. The von Mises stress of graphene NEMS switch with and without perforations…………………………………………………………………...41
14. Schematic diagram of standard beam structure in down state………………..42
15. Schematic diagram of perforated beam in down state………………………...42
16. The von Mises stress of GO NEMS switch with and without perforations…………………………………………………………………...43
17. Contour plot of von Mises stress for standard and perforated GO beam structure……………………………………………………………………44
18. Electric field distribution GO beam structure…………………………………44
19. Total capacitance in down state………………………………………………45
20. Variation in Capacitance plot for standard and perforated GO NEMS Switch…………………………………………………………………...46
21. GO/gold NEMS switch……………………………………………………47
22. GO/gold double clamped beam………………………………………………47
23. (a) Intact GO beam in downstate (b) Circularly perforated beam in down state………………………………………………………………………...48
24. Gap vs applied voltage plot…………………………………………………..49
25. First six eigen modes of intact structure……………………………………50
26. First six eigen modes of perforated beam……………………………….........50
27. GO-based RF NEMS switch…………………………………………………52
28. Top view of GO-based RF NEMS switch……………………………………53
29. Side view of total displacement for 30 nm gap………………………………..54
30. Pull-in analysis for 30 nm gap………………………………………………...54
31. First three eigenfrequency modes mono/multilayer GO NEMS switch……………………………………………………………………55
32. Obtained (a) Insertion loss (b) Isolation of GO NEMS switch……………….56
33. NEMS switch with intact beam structure…………………..........................58
34. Different graphene bridge structures…………………………………………59

35. Total displacement of different structures (a) structure-1 (b) structure-2 (c) structure-3 (d) structure-4 (e) structure-5……………..................................60
36. Downstate capacitances……………………………………………………61
37. GO-based NEMS shunt switch (a). Schematic diagram (b). Top view…………………………………………………………………….62
38. Simulated GO-based NEMS shunt switch during (a) On state (b) Off state……………………………………………………………………...64
39. Variation in pull-in voltage by varying (a) GO length (b) GO thickness (c) Air gap………..…………………………………………………………...65
40. Pull-in voltage trends against different design parameters of the NEMS switch……………………………………………………………………66
41. Von Mises contour plot………………………………..………………...66
42. Side view of electric field distribution……………………………………...67
43. First six eigenfrequency modes GO NEMS switch…………………………...68
44. S-parameters analysis of GO NEMS switch (a). Insertion loss (b). Isolation……………………………………………………………………69
45. Top view of NEMS switch…………………………………………………72
46. Simulated graphene NEMS switch…………………………………………...72
47. Effect of variation of beam length of Single material Graphene beam on (a) Restoring force (b) Spring constant for different beam length……………......73
48. Comparison between the results obtained for (a) restoring force (b) pull-in voltage (c) spring constant using two different methods……………………...74
49. Schematic diagram of (a). single material (b). composite beam NEMS switch……………..…………………………………………………….75
50. Simulated graphene/RGO NEMS switch…………………………….........76
51. Simulated graphene/GO NEMS switch……………………………………76
52. Composite beam and its equivalent single material beam……………….......77
53. Eigenfrequency analysis of single material beam and composite beams…………………………………………………………………78
54. Effect of variation of beam length of single material graphene beam on (a) Switching time and pull-in voltage (b). Release time and pull-in voltage (c). Restoring force and pull-in voltage………………………………………...79
55. Effect of variation of beam length of graphene/RGO composite beam on (a) Switching time and pull-in voltage (b). Release time and pull-in voltage (c). Restoring force and pull-in voltage………………………………………...80
56. Effect of variation of beam length of graphene/GO composite beam on (a) Switching time and pull-in voltage (b). Release time and pull-in voltage (c). Restoring force and pull-in voltage………………………………………...80
57. Single material vs Composite material (a) Beam length vs pull-in voltage (b). Beam length vs Restoring force (c). Beam length vs switching time (d). Beam length vs release time……………………………………………………81
58. Cantilever operation in upstate………………………………..………...86
59. Cantilever operation in downstate…………………………………………86
60. NOT gate structure…………………………………………………………87

61. NOR gate structure……………………………………………………………87
62. NAND gate structure…………………………………………………………88
63. XOR gate structure……………………………………………………………89
64. 3D model of NOT gate (a) when $V_1 = 0$ (b) when $V_1 = 1$……………………90
65. 3D model of NOR gate (a) when V_1V_2= 00 (b) when V_1V_2= 01 (c) when V_1V_2= 10 (d) when V_1V_2= 11………………………………………………………...91
66. 3D model of NAND gate (a) when V_1V_2= 00 (b) when V_1V_2= 01 (c) when V_1V_2= 10 (d) when V_1V_2= 11…………………………………………………92
67. 3D model of XOR gate (a) when V_1V_2= 00 (b) when V_1V_2= 01 (c) when V_1V_2= 10 (d) when V_1V_2= 11………………………………………………………...93
68. Fabrication Process flow of proposed RF NEMS switch……………………98
69. Fabrication Process flow of cantilever NEMS shunt switch (XOR gate) …….99

LIST OF ABBRIVATIONS

2D	Two-Dimensional
3D	Three-Dimensional
BiCMOS	Bipolar Complementary Metal-oxide-semiconductor
CVD	Chemical Vapor Deposition
CMOS	Complementary Metal-oxide-semiconductor
CPW	Co-Planar Waveguide
FEA	Finite Element Analysis
FET	Field Effect Transistor
FEM	Finite Element Method
GO	Graphene Oxide
HF	High Frequency
HFSS	High Frequency Structure Simulator
IC	Integrated Circuit
LF	Low Frequency
LPCVD	Low Pressure Chemical Vapor Deposition
MEMS	Microelectromechanical Systems
MOSFET	Metal-oxide-semiconductor Field Effect Transistor
MIM	Metal–insulator–metal
MMIC	Monolithic Microwave Integrated Circuit
NEMS	Nanoelectromechanical Systems
PCG	Poly Crystalline Graphene
RADAR	Radio Detection And Ranging
RF	Radio Frequency
RFICs	Radio-frequency Integrated Circuit
RGO	Reduced Graphene Oxide
SCG	Single Crystalline Graphene
PCG	Poly Crystalline Graphene
S-parameters	Scattering parameters

Chapter 1
INTRODUCTION

1.1 Need of new material

In the past several decades, silicon integrated circuit technology has made significant progress. The innovations that have led to the miniaturization of the metal-oxide-semiconductor field-effect transistor (MOSFET) into smaller dimensions have driven this technology growth [1]. This realization has encouraged the research for alternative technologies that includes both new device principles and new materials. The motive of using the new device principles is to improve the integrated circuits (ICs) functionality by including the application areas like nanoelectromechanical systems (NEMS), actuators, and sensors, etc. The purpose of searching a new material and replacing the already available materials is to improve the total performance of the device [2]. Based on the material of suspended beam, microelectromechanical (MEMS) switches can be classified into the metal-based switches and carbon material-based switches [3][4][5]. All the beam materials have their pros and cons.

Already existing mechanical switches can be used for high power handling but are heavy and slow. Semiconductor switches exhibit high speed; however, they have poor RF performance and consumes high power. Si-FET (Field-effect transistor) can handle high power at low frequencies (LF) but at high frequencies (HF) the performance deteriorates. In FET, scaling down the device dimensions adversely effects the performance of the device. It decreases the distance between the different parts of the device and the applied voltage. The scaling down concept increases the leakage current, specifically the sub-threshold leakage current [6]. Since MEMS switches require physical contact for current flow from one port to another port. No current can flow between two ports if the switch is off. It greatly reduces off-state power consumption and improves the on-off ratio. Thus, MEMS switches are the solution to the subthreshold leakage problem. MEMS switches can be used at RF as it provides low pull-in voltage, nearly zero power consumption, low insertion loss, and high isolation [7].

The switching speed of MEMS switch is low as compared to semiconductor switches. As compared to MEMS switches, NEMS switches are smaller in size, lighter

in weight, and have smaller footprints for use in circuits. NEMS switches attain low actuation voltage, improved ON/OFF ratio, reduced leakage current, high switching speed as compared to already existing switches [8]. NEMS technology is relatively not effected by extreme radiations [9] or temperature conditions [10][11] and NEMS devices can be used in defence applications. Additionally, the logic gates build from NEMS switches require very fewer components as compared to the logic gates build from Complementary Metal-oxide-semiconductor (CMOS) components [9][10]. M/NEMS switches can also be used in circuits as phase shifters, matching networks, and tuneable filters [12][13].

In nanoelectronics applications, carbon-based materials are of great interest and are widely used because of their outstanding properties [14][15]. Graphene is a carbon-based two-dimensional material which has attracted the attention of researchers worldwide for use in nanoelectronics. The interesting electrical [16], mechanical [17], and thermal [18] properties have motivated the interest of researchers in applications like nanoelectronics, electrochemical, photonics, and electromechanical, etc. In RF applications, graphene has been widely used to make graphene transistor as an amplifier because of properties like high mobility [19][20]. In the application areas that needs a high-speed NEMS switch with low pull-in voltage, graphene can be a good option as beam material but at the expense of large losses [21]. Also, the very high Young's modulus makes graphene beam stiff and leads to structural deformation (buckling) of graphene beam [22].

Graphene derivatives graphene oxide (GO), reduced graphene oxide (RGO) have moderate Young's modulus value that makes the beam less stiff and more flexible. Graphene derivatives can be used as a suspended beam, alone or along with graphene or any other metal (as a composite beam). The main goal of the thesis is to design and simulate a graphene derivative-based NEMS switch with low actuation voltage, high switching speed, and good RF performance.

1.2 RF MEMS switches

MEMS have empowered the use of electronic devices at radio frequency (RF) through RF MEMS switches. A MEMS system with electronic components comprising of moving sub-millimetres sized parts to provide RF functionality is known as RF

MEMS switch [23]. The performance of MEMS switches has made them superior to already existing switches. MEMS switches can operate at RF from DC to a few hundred GHz frequency range and can provide good RF performance [24]. The semiconductor industry's success depends upon efficiently scaling down the device dimensions along with reliable performance. NEMS is the extended version of MEMS where M/NEMS devices are the combination of electrical and mechanical components. RF M/NEMS switches are used for signal routing, impedance matching, and signal switching [7].

1.3 RF MEMS switch mechanism

The actuation mechanism of the switch comprises of mechanical and electrical actuation. The movement of the suspended beam or cantilever defines the mechanical actuation. The mechanical actuation takes place when a voltage is applied at the actuating electrode called electrical actuation. Four different actuation mechanisms can be responsible for the mechanical movement of the switch. The detailed explanation of different actuation mechanisms is given below.

- The RF MEMS switch based on the piezoelectric actuation mechanism, a piezoelectric material like AlN/PZT is used on the top of the suspended beam. When the voltage is applied at piezoelectric material, the material gets elongated and strain is produced across the length of the piezoelectric material. In this way, the beam is deflected [25][26][27]. Using this mechanism, high force is generated and that reduces the pull-in voltage.
- In electromagnetic actuation mechanism, a coil is used on the top of the suspended beam. The applied DC voltage creates electromagnetic forces and actuates the suspended beam. But the coil or the permanent magnet used for actuation leads to self-latching phenomena [28][29][30].
- In the electro-thermal actuation mechanism, the deformation of the beam is decided by the thermal expansion coefficient. A resistor is used on the top of the suspended beam and the applied current to the resistor causes the thermal wave to propagate and deflect the beam [31][32].
- Out of these four actuation mechanisms, the electrostatic actuation mechanism is always preferred because of the benefits like low power consumption, small electrode area, high speed, and high capacitance ratio, etc [33]. But it requires a

high actuation voltage [34]. In electrostatic actuation, the voltage can be reduced up to 5V by using the materials with low spring constant, perforated structure, and meander structures.

1.4 Basic operating principle

In M/NEMS switches, an electrostatic actuation mechanism is used to deflect the suspended beam on the actuation electrode. In this way, the switch actuates between on and off states. The electrostatic forces are inversely proportional to the square of the gap between the suspended beam and the actuation electrode. If the air gap of the switch is increased, the effect of forces decreases and more voltage is required to snap down the beam. As the switch dimensions are scaled-down, the effect of forces becomes more prominent [35][36].

Two kinds of forces act between the double clamped beam and the actuation electrode. One is the electrostatic force that tries to pull down the suspended beam when voltage is applied to the bottom actuation electrode. The other is restoring force that occurs in the suspended beam that tries to hold the beam in its initial position. There is a competition between the electrostatic force and the elastic restoring force. When the applied voltage is increased, the electrostatic force starts to pull the beam towards the actuation electrode. At a certain voltage, the electrostatic force overcomes the elastic restoring force and the suspended beam comes in contact with the actuation electrode.

When the switch is closed, restoring force of suspended beam tries to pull the switch in open state. But the adhesive forces between the suspended beam and actuating electrode counteract this and the switch remains closed. The stiffer beam material and larger air gap lead to volatile operation [37][38]. Nonetheless this case requires high actuation voltage and it may lead to electrothermal failure. On the other hand, less stiff material and smaller gaps lead to non-volatile operation and require less actuation voltage.

1.5 RF MEMS switch structures

MEMS switches can be classified on the basis of four different actuation methods, movement of the beam (can be vertical or lateral), type of contact (ohmic or capacitive) and configuration in which the switch can be inserted in the line (series or shunt). Based on the boundary conditions, there are two categories of the MEMS switches, contact

type and capacitive type. The contact type consists of a cantilever, in which one end is fixed, the other end is free moving and the capacitive type consists of a suspended beam/bridge, in which both the ends are fixed. Contact type switches are mainly preferred as series switches and capacitive switches are preferred as shunt switches [39]. In MEMS switches, the intermolecular forces like van der Waals forces are neglected but they should be considered in NEMS switches.

1.5.1 Series contact type

A series contact type switch consists of a thin metal cantilever in series with the transmission line. The electrostatic force is generated due to the applied voltage, pulls the cantilever downward and cantilever touches the bottom electrode. This particular voltage at which the cantilever touches the bottom electrode is known as actuation voltage/pull-in voltage. Hence the signal passes from one end to another end of the cantilever. In this way, the switch is closed and the input and output ports of transmission lines are shorted through the cantilever [40]. Figure 1 (a), (b) shows the OFF and ON state of the MEMS cantilever switch.

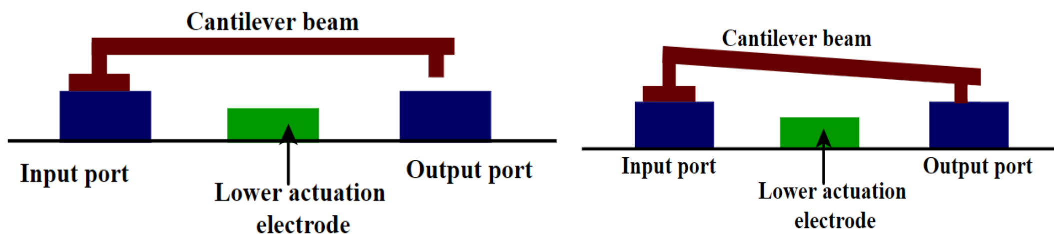

Figure 1: MEMS series contact switch (a) OFF state (b) ON state

1.5.2 Shunt capacitive type

This switch configuration comprises of a bridge/suspended beam structure that is fixed at both ends. This bridge structure is also known as double clamped beam/fixed-fixed beam structure. This bridge is suspended at a certain height over the transmission line of CPW (coplanar waveguide). The metal transmission line is covered by a thin layer of dielectric. The suspended beam is located perpendicularly over the transmission line, hence known as a shunt switch. The biasing voltage is applied at the bottom actuating electrode and suspended beam is kept at zero voltage. When the applied voltage is insufficient to pull down the suspended beam, it remains in upstate as shown in figure 2 (a). In this state, the signal in the transmission line passes from

input to output without any interruption. But when the applied voltage is increased and becomes equal to the actuation voltage, the suspended beam is snapped down and touches the signal line. The switch comes in downstate and the signal from the transmission line is grounded through the suspended beam as shown in figure 2 (b). In OFF state, capacitor structure is formed as the beam touches the dielectric and downstate capacitance exists [41].

In series contact type switch, metal stiction problem is encountered and it consumes more power than shunt capacitive switch.

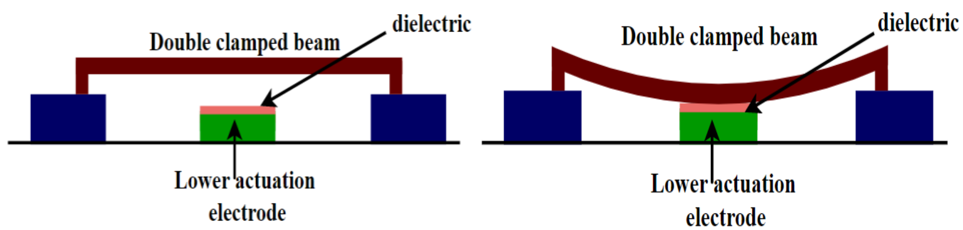

Figure 2: MEMS shunt capacitive switch (a) ON state (b) OFF state

1.6 Electromagnetic modelling of MEMS switch

For RF to millimeter-wave circuit designing, series type and shunt type switch are used. The ideal series switch acts as an open circuit in upstate when inserted in the transmission line and short circuit in the downstate. The ideal series switches have zero insertion loss, and infinite isolation, and series switch configuration can be broadly used upto 40 GHz. On the other hand, shunt switch is placed perpendicularly with the transmission line and the ground. The position of the beam i.e. whether it remains in the actual position or it connects the transmission line and ground line is decided by applied voltage. Also, the transmission of signal from one point to another point is further decided by the position of the beam. The ideal shunt switch exhibits zero insertion loss and infinite isolation. The shunt capacitive switches are most suitable for higher frequencies 5-100 GHz. Figure 3 (a) shows the side view, (b) top view when the switch is inserted in the transmission line, and (c) CLR model of the shunt switch configuration.

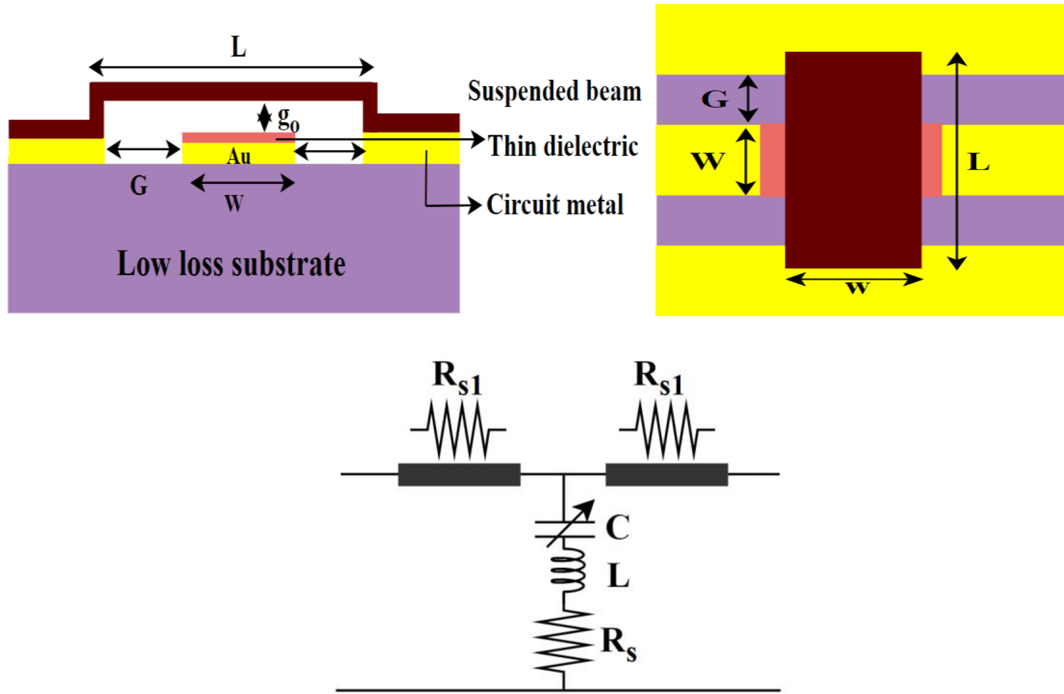

Figure 3 : MEMS switch (a) Side view (b) Top view (c) CLR model of the switch configuration

1.6.1 MEMS shunt capacitive switch description

As shown in figure 3 (a), the suspended beam is placed at some height (g_o) above the dielectric layer over the transmission line. The dielectric material of some thickness (t_d) and dielectric constant (ε_r) is deposited on the central actuation electrode. The width of the central conductor is W µm. The suspended beam of length L µm, width W µm, and thickness t µm is fixed at both ends at ground planes of the transmission line.

For RF signal transmission, either a CPW or micro-strip line is considered. In the CPW line, the signal line and the ground lines both are on the same plane. The ends of the suspended beam are connected to the ground planes while DC voltage is applied between the suspended beam and the central conductor. Because of electrostatic forces, the suspended beam collapses on the central conductor and makes a capacitor structure acting as a short circuit. As the applied voltage is removed, the beam retains its initial position due to the restoring force of the beam material.

The shunt capacitive switch can be modelled by the two short sections of the transmission line and the lumped CLR model of the suspended beam/bridge. The shunt impedance of the switch can be given by equation 1:

$$Z_s = R_s + j\omega L + \frac{1}{j\omega c} \tag{1}$$

In the equation 1, depending upon the position of the beam, C defines the capacitance either in upstate or in downstate. The LC series resonant frequency of the switch can be approximated by equation 2**:**

$$f_0 = \frac{1}{2\pi}\frac{1}{\sqrt{LC}} \quad (2)$$

At resonant frequency (f_0), it behaves like a resistive circuit, below f_0 , it behaves like a capacitor and above f_0, it behaves like inductor. In the upstate position, the inductance does not affect the switch performance, it only plays a significant role when the switch is in downstate.

1.7 MEMS switch design parameters

1.7.1 Pull-in voltage

In electrostatic actuation, the applied voltage at which the suspended beam/cantilever touches the bottom actuation voltage is known as pull-in voltage/actuation voltage [42][43]. It can be expressed by equation 3:

$$V_{pi} = \sqrt{\frac{8k}{27\varepsilon_0 A} {g_o}^3} \quad (3)$$

Where k is the spring constant of the suspended beam, g_o is the air gap, ε_o is the permittivity, A is the actuation area. The spring constant k can be expressed by equation 4 [44].

$$k = 17.63\ Ew\left(\frac{t}{L}\right)^3 \quad (4)$$

Where E is Young's modulus/elastic modulus, w is the suspended beam width, t is thickness and L is length of the suspended beam. The pull-in voltage depends upon the spring stiffness, area of the actuation electrode, and air gap between the beam and actuation electrode.

1.7.2 von Mises stress

The approach that is used to evaluate if a given material will yield or fracture is known as von Mises stress [45]. The maximum distortion energy theory was initially proposed by Hubert in 1904 and further developed by von Mises in 1913. The theory of maximum distortion energy states that when von Mises stress reaches the yield strength of the material, the elastic failure occurs. The yielding of the material occurs

when distortion energy reaches a critical value. The von Mises stress is given by equation 5 [46]:

$$\sigma_{vm}=\sqrt{0.5(\sigma_x-\sigma_y)^2+(\sigma_y-\sigma_z)^2+(\sigma_z-\sigma_x)^2} \quad (5)$$

Here $\sigma_x, \sigma_y,$ and σ_z are the stress in x, y, and z cartesian coordinate system, respectively. The von Mises is not a stress, it is a measure of energy density. This concept is used by the designer to check whether the design will withstand load conditions or not. It is used to find out the distortion energy density at a particular point.

1.7.3 MEMS capacitance

The MEMS shunt switch capacitance is measured at the position of the beam. If the beam is in unactuated state then it is known as upstate capacitance but if the beam is actuated and touches the actuating electrode, it is known as downstate capacitance. The upstate and downstate capacitances are expressed by equation 6, 7 [21]:

$$C_{up}=\frac{\varepsilon_o w W}{g_o+\frac{t_d}{\varepsilon_r}} \quad (6)$$

$$C_d=\frac{\varepsilon_r\varepsilon_o}{t_d} wW \quad (7)$$

S-parameters like isolation and insertion loss are defined by the ratio of upstate capacitance to the downstate capacitance. The low insertion loss and high isolation can be achieved if the C_{Ratio} is high. Capacitance ratio is the ratio of the downstate capacitance to the upstate capacitance and is given by equation 8:

$$C_{Ratio}=\frac{C_d}{C_{up}}=\frac{\frac{\varepsilon_r\varepsilon_o}{t_d}wW}{\frac{\varepsilon_o w W}{g_o+\frac{t_d}{\varepsilon_r}}} \quad (8)$$

1.7.4 Series resistance

For modelling the series resistance, the input or output line should be of 50 Ω or known impedance. MEMS switch is comprised of two resistive components, R_{s1} and R_s. R_{s1} is the resistance due to the transmission line loss while R_s is the resistance due to the MEMS bridge structure. Also, R_{s1} can be calculated by the line loss, $\alpha=\frac{R_{s1/l}}{2Z_o}$ Np/m. The MEMS bridge resistance R_s cannot be calculated easily as in both the states current distribution is different. In the OFF state, R_s can be approximated from the S-parameters. If the thickness of the suspended beam is smaller than two skin depths

($\delta = \frac{1}{\sqrt{f\pi\mu\sigma}}$), R_s remains constant with frequency. For thick suspended beams, R_s changes with $\sqrt{f}$. When the switch is actuated, the current flows through the bridge to the ground terminal. The resistance of the bridge and resistance of the transmission line gives total resistance of the switch. The bridge resistance can be given by equation 9 [47]:

$$R_b = \frac{\sigma_{b\,(L/2)}}{2A} \tag{9}$$

1.7.5 Inductance

For modelling the inductance, the input or output line should be of 50 Ω or known impedance. The inductance of the suspended beam is evaluated by the portion of the suspended beam over the transmission line and it does not depend on the portion of the suspended beam over the actuation conductor. If the width of the suspended beam is increased, the bridge inductance decreases. If the spring constant of the suspended beam is changed by varying its shape, the bridge with the very low spring constant will have a high inductance value.

1.7.6 S-parameters

S-parameters are used to characterize high-frequency circuits. S-parameters define the change in the signal from input to the output port when the switch is inserted in the RF line. It describes the input-output relationship between the ports of the electrical system at HF. S-parameter analysis is necessary to optimize the behavior of NEMS switches in terms of isolation, insertion loss at HF. Insertion loss is the loss of signal power that occurs when a switch is inserted in a transmission line. Insertion loss (S_{21}) is evaluated when the switch is upstate and it should be less than 0 dB. In the upstate position, S_{11} i.e. the upstate reflection coefficient can be calculated as given by equation 10 [33]:

$$|S_{11}|^2 \cong \frac{\omega^2 {C_u}^2 {Z_o}^2}{4} \tag{10}$$

The high value of reflection coefficient leads to high insertion loss. So, low upstate capacitance is desirable. Isolation states the ability of the switch to prevent the signal from appearing at a port in the circuit where it is not desired. The large value of isolation depicts minute coupling between output and input port. Isolation is evaluated when the

switch is downstate. A high value of isolation is desirable and it (S_{21}) should be greater than 30 dB. In downstate, S_{21} can be calculated as given by equation 11 [33]:

$$|S_{21}|^2 = \frac{4}{\omega^2 {C_d}^2 {Z_o}^2} \tag{11}$$

On multiplying equations 10 and 11, equation 12 is obtained:

$$|S_{21}|^2 = \frac{1}{|S_{11}|^2} \left(\frac{C_u}{C_d}\right)^2 \tag{12}$$

1.7.7 Eigenfrequency Analysis

Eigenfrequency, also known as fundamental characteristic frequency/natural frequency, is a frequency at which a device vibrates. When a device vibrates at a certain eigenfrequency, structural deformation takes place in a particular mode. The eigenfrequencies can be calculated by solving the Lagrangian of the system followed by the canonical equation. The harmonic motion of the mass-spring system for single degree of freedom can be modelled by a second-order differential equation 13:

$$m_{eff} \frac{d^2x}{dt^2} + \Upsilon_{eff} \frac{dx}{dt} + k_{eff}\, x = F_e \tag{13}$$

Where, m_{eff} is the effective mass of suspended beam, Υ_{eff} is an effective damping coefficient, k_{eff} is effective spring stiffness and F_e is electrostatic force.

Eigenfrequency analysis provides information about the shape of eigenmode [48]. Each eigenmode has a different eigenfrequency value. The desired motion is represented by the primary eigenmode. The natural frequency of the suspended beam depends upon the effective spring constant and effective mass [49] given in equation 14. The next high mode f_1 of eigenfrequency can be determined by equation 15.

$$f_0 = \frac{1}{2\pi}\sqrt{\frac{k_{eff}}{m_{eff}}} \tag{14}$$

$$f_1 = \frac{1}{2\pi}\left[\frac{15.418}{L^2}\right]\sqrt{\frac{EI_x}{\rho}} \tag{15}$$

Here, k_{eff} = Effective spring constant
m_{eff} = Effective mass
E = Young's modulus
ρ = Mass density
I_x = Inertia
L = Length of beam

k_{eff} depends upon the Elastic modulus of the suspended beam and device dimensions. The high eigenmodes depend upon the inertia of the beam and device dimensions.

1.8 Methods to reduce pull-in voltage

1.8.1 Use of low spring constant structures

Introducing small diameter holes in the MEMS switch improves the switching speed. Holes reduces the residual stress and the spring constant of the suspended beam, which in turn reduces the actuation voltage. By making holes in the beam, the mass of the suspended beam gets reduces and the beam resonates at a much higher frequency. The electrostatic forces are not affected by the hole density and the placement of the holes. During actuation, the air below the perforated structure gets easily squeezed out and helps in further reducing the actuation voltage. It makes the switching operation faster [50]. In the fabrication process, the holes act as tunnels for etching the sacrificial layer. Figure 4 shows the top view of the circularly perforated beam.

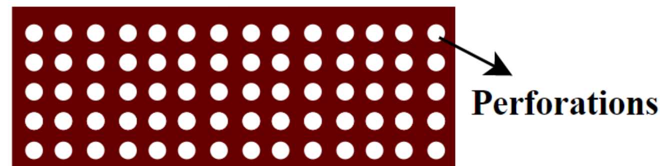

Figure 4: Perforated structure

The development of a low spring constant system (meander structure) has been done to achieve low pull-in voltage [51][52]. The pull-in voltage can be reduced by increasing the number of meander structure. For the low spring constant membranes, different structures can be used as shown in figure 5.

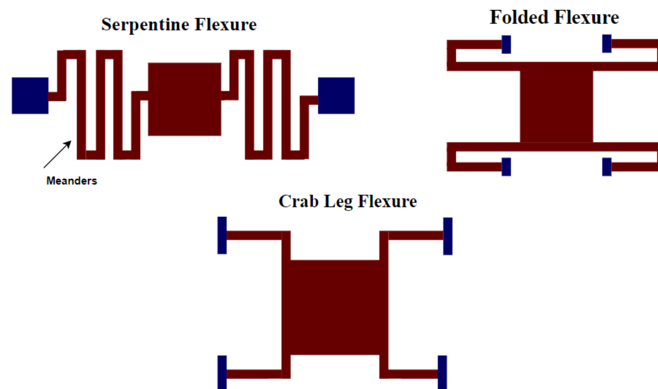

Figure 5: Various meander structures

1.8.2 Change the device dimensions

The change in device dimensions (length, width, thickness of beam) affects the actuation voltage of the NEMS switch. From equation 3, it is evident that the pull-in voltage is directly proportional to the gap between the suspended beam and the actuation voltage. If the gap is increased, the pull-in voltage also increases. The pull-in voltage is also dependent on the spring constant. The change in the beam length and beam thickness changes the spring constant of the beam, which in turn changes the pull-in voltage.

1.8.3 Other materials with low elastic modulus

The spring constant of the beam depends upon elastic modulus of the beam material. Very high elastic modulus of any beam makes the beam stiffer and less flexible. Also, very high Young's modulus value increases the pull-in voltage. The beam flexibility of the suspended beam can be improved by replacing the existing beam material with another beam material having a low spring constant.

1.9 NEMS switch

In RF communication systems, the demand for high-performance devices has grown drastically [53]. NEMS devices are light in weight, small in size, consume very low power, and are highly linear. In the era of miniaturization, NEMS switches can be preferred over the already existing conventional switches due to some outstanding properties like extremely small size, sharp switching, low leakage current, and large capacitance ratio [8]. For applications like logic gates and data storage, NEMS switches can be used [54]. Already existing metal switches suffer from the problem of stiction, self-actuation, and electromigration [55]. The basic working operation of both MEMS and NEMS switch is the same but as the feature size reduces, the intermolecular forces come into effect. Graphene is a monolayer of carbon atoms having remarkable electrical and mechanical properties. Graphene NEMS switches overcome the stiction problem with better reliability [56]. Graphene-based NEMS switches offer lower pull-in voltage and fast switching speed [21]. But Graphene NEMS switches suffer from problems like structural deformation and low life cycle [57]. Very high elastic modulus of the graphene beam makes the beam stiffer and due to repetitive on-off switching of NEMS switch, structural deformation takes place.

1.9.1 Graphene Oxide

GO is an oxidized form of graphene having different radicals connected with carbon atoms by covalent bonds. The structure and properties of GO depend upon the synthesis method and degree of oxidation. Depending on the degree of oxidation, GO can be a semiconductor or an insulator [58]. The physical and mechanical properties of GO can be changed by varying the degree of oxidation [59]. Rippling in GO can alter the mechanical characteristics of the material [60]. In GO, on increasing the oxidation rate Poisson's ratio decreases linearly. For fully oxidized GO, the value of Poisson's ratio is negative [61]. Young's modulus value of GO is 27–31 GPa which is much lower than Young's modulus value of graphene 1 TPa [62][22]. This lower value of Young's modulus makes the beam less stiff and more flexible. The low stiffness of GO is associated with an unexpected low bending modulus and makes it super flexible [63]. GO can be used in application like sensors [64][65], capacitors [66], transparent conductors [67], solar cells [68], drug delivery [69], membranes [70], cellular migration [71], and water purification [72][73] etc. Different methods can be used to produce high-quality GO [74][75] but most of these methods use strong oxidants that result in the production of the GO with certain defects. The conducting property of GO gets highly reduced while optical and mechanical properties suffer from less impact.

1.9.2 Reduced Graphene Oxide

RGO is a graphene derivative that is formed by thermal or chemical reduction of GO. The purpose of the reduction method is to remove the oxygen groups and restore the conductivity. RGO has similar mechanical and electrical properties as pristine graphene. As it has graphene-like properties, RGO is highly desirable to be used in applications like sensors, optoelectronics devices, and storage devices [76]. RGO can be prepared easily in the desired quantity from GO using different methods [77][78]. The different methods of reducing lead to the formation of different quality of RGO with highly reformed properties.

Using the laser annealing method, the measured value of Young's modulus of RGO is 207 GPa and Poisson's ratio is 0.197 [79][80]. RGO possesses less value of Young's modulus than graphene. Thus, RGO possesses high charge carrier mobility and significant conductivity.

Graphene derivatives GO and RGO can be used along with graphene or any metal as a composite beam.

1.10 Thesis outline

In this thesis, graphene derivatives have been used as a suspended beam material for the first time. The advantages of using a composite beam of graphene derivative along with graphene or any other metal have been presented in this work. The finite element modelling (FEM) of the graphene derivative-based NEMS switch is successfully analyzed.

Chapter 1 (This chapter) explains the need for new materials and detailed introduction of RF M/NEMS switches, different types of switch configurations, various actuation mechanisms, and new graphene materials. Also, different design parameters are explained comprehensively. The various methods to reduce pull-in voltage have been discussed. Brief introduction of two new graphene materials with their properties is provided.

Chapter 2 discusses the relevant previous research in the field of RF MEMS switches starting from the development of first MEMS switch and the different methods that have been adopted to improve the switch performance. Based on different methods like low spring structure, materials with high dielectric constant, switch designed for specific bands etc., a plethora of MEMS switches have been proposed and implemented successfully. Also, based on the available literature, the research gaps are identified and on the basis of the research gaps, the research objectives are formulated.

Chapter 3 describes the simulations performed using standard and perforated GO beam with graphene. Also, by considering standard and perforated GO beam with gold electrode, analysis of NEMS switches have been done. In both the cases, different dimensions of the switch are considered. The simulation of GO NEMS switches have been performed to evaluate the actuation voltage, total capacitance, and to ensure the mechanical reliability.

Chapter 4 deals with the electromechanical modelling of the GO NEMS switch. In this chapter, performance analysis of GO NEMS switch at RF has been explained. The analysis of the switch has been done for monolayer and multilayer GO beam structures.

The different eigenfrequency modes, switching time, switch resistance, inductance and capacitance have also been evaluated.

Chapter 5 describes the design and analysis of graphene NEMS switch using various suspended beam structures. Five different bridge structures are designed and analysed to find out the structure with least actuation voltage.

Chapter 6 the structure with least pull-in voltage has been evaluated in previous chapter. Assuming the same structure but of different material (GO), optimization of different design parameters has been performed in this chapter. It has been observed that changing the design parameters changes the performance of the NEMS switch in terms of actuation voltage and mechanical reliability.

Chapter 7 explains the benefits of using a composite beam over a single material beam for RF NEMS switch. In this chapter, different methods are used to reduce the actuation voltage without compromising on the restoring force. A single material beam and two different composite beams have been designed and analysed. A comparative analysis in terms of actuation voltage, switching speed and restoring force of single material beam and composite beam has been done.

Chapter 8 presents the design and modelling of graphene NEMS switch using cantilever structure. The successful implementation of different digital logic gates has been carried out using graphene cantilever NEMS switch with high switching speed.

Chapter 9 describes the conclusion drawn from the present research work. Moreover, this chapter also depicts the future research agenda for practitioners, engineers and potential researchers.

Chapter 2
LITERATURE SURVEY

The growing demand for high-performance RF communication systems has attracted the attention of several researchers from electronics industries and educational institutes towards RF MEMS switches. Till now, a plethora of MEMS switches have been designed by considering different design parameters, different materials for substrate/dielectric/suspended beam, and different actuation mechanisms to achieve better performance of RF MEMS switch. The relevant previous research performed on M/NEMS switches is reviewed in this chapter. The literature review of RF M/NEMS switch is organised on the basis of different actuation mechanism (section 2.1), low spring constant structures (section 2.2), high-k dielectric based structures (section 2.3), fabrication processes of switches (section 2.4), switches for specific bands (section 2.5), and development of NEMS switches (section 2.6). The identified research gaps and formulated research objectives are summarised in section 2.7 and 2.8 respectively.

2.1 Different actuation mechanism-based RF MEMS switch

K. E. Petersen developed the first MEMS switch in 1979. He believed that a bulk micromachined cantilever can be used on the silicon substrate to achieve a switching mechanism at an actuation voltage of 70 V. After that, research on the development of the RF MEMS switches gained pace [81]. Subsequently, RF MEMS switches were studied extensively for communications applications. The small size of the switch offers benefits like high resonance frequency, low mass, and low power consumption [82]. The first shunt capacitive switch was fabricated by Raytheon in the late ’90s. Goldsmith and his team developed a shunt capacitive switch that was previously known as the Texas Instrument switch [83]. A 0.3–0.5 μm thick Al membrane was used as a bridge and it was positioned at the height of 3–5 μm over the CPW transmission line. For the sacrificial layer, polyimide was used and an electrode of tungsten-alloy was used beneath the bridge. The plasma etching method was used to release the suspended beam of Al. The developed shunt capacitive switch can be used as filters and switching networks for X-band and K-band phase shifters applications. A pull-in voltage of 50 V with 6 μs on switching time and 4 μs off switching time was observed. At 20 GHz, the insertion loss of 0.14 dB was observed [84]. The MEMS switch developed by Raytheon

gave a direction towards the micromachined switches to other researchers. Later on, different types of RF MEMS switches were studied and fabricated by various research centers.

H.S. Newman discussed the RF MEMS switches and their applications. The basic principle of operation and insertion of RF MEMS switch, fabrication process, circuit applications, and reliability issues have been explained thoroughly. It concludes that low actuation voltage RF MEMS switch should be preferred as high pull-in voltage has an adverse effect on the reliability of the MEMS switch. Also, the lifetime of the switch decreased by an order of magnitude for every 5 to 7 V increase in the actuation voltage [85]. Gold smith et al. reported the exponential relationship between the applied voltage and switch lifetime. The results demonstrated that the lifetime of the MEMS switch improves on the order of a decade for every 5 to 7 V decrease in applied voltage. For MEMS switch to have a lifetime of more than a billion cycles, it should operate at a voltage less than 40 V [86].

Chang et al. developed an ohmic switch using GaAs substrate [87]. The fabrication of ohmic switch having 0.5 μm/0.1 μm Al/Cr cantilever was done. The bottom electrode and transmission line of 4000 Å thick gold electrode and dielectric material of 3000 Å thick SiO_2 layer were used for fabrication. Amorphous silicon of 1μm thickness was used as the sacrificial layer. A capacitive connection is formed between the center of the transmission line and the ground by the switch. The fabricated switch shows a high pull-in voltage (26–30 V) and a switching speed of 10 ms. When the RF performance of the switch was analyzed at 10 GHz, an insertion loss of −0.2 dB, and isolation of -17 dB was measured. In 2001, a low pull-in voltage RF MEMS switch was proposed by Schauwecker et al. that has high power capability and can be used for high broadband applications. The electromagnetic simulation and fabrication of simulated switch were presented in the study. The pull-in voltage of 16 V, isolation of 22 dB and insertion loss of < 0.85 dB at 30 GHz were observed [88].

Nishijima et al. proposed a novel structure of metal contact RF MEMS switches with low pull-in voltage. A 5 μm thick gold cantilever with contact dimples was used along with a pull-down electrode. A pull-in voltage of 30 V, isolation of 29 dB, and insertion loss of 0.2 dB at 2 GHz were achieved. At the tip of the cantilever, deflection is induced by stress [89]. Daneshmand et al. reported thermally actuated RF MEMS switch for

multiport band selection network. For thermal actuation, thermal actuators were used and connected to the metal plates of the transmission line. The thermally actuated RF MEMS switch exhibits repeatable RF results up to 6000 cycles, isolation of 20 dB and insertion loss of 0.3 dB [90].

Park et al. presented the design, fabrication, and measurement of RF MEMS shunt capacitive switch for 24 GHz RADAR (Radio detection and ranging) applications. The fabricated switches presented high reliability and long lifetime and were free from micro-welding and stiction problems. The comb-drive actuators were used to precisely regulate the capacitance. The copper beam-based MEMS switch actuated at 25 V, showed insertion loss of 0.29 dB and isolation of around 30 dB [91].

Nawaz et al. reported the effect of surface roughness on the electromechanical performance of RF MEMS switch. FEM-based simulation methodology was used to estimate the surface roughness effects on the parameters like upstate capacitance, downstate capacitance, pull-in voltage, pull-in gap, and switching time of RF MEMS switch. The result depicts that surface roughness shows predictable shifts in electromechanical characteristics. For the air gap of 0.4 µm and surface roughness of 50 nm, the pull-in voltage got changed by 28.5%. Also, the upstate capacitance increases and switching time decreases (by 24.2%) by increasing the surface roughness. The estimation of surface roughness using FEM based methodology is a good alternative for complex models [92].

In double clamped beam structures, the actuation mechanism plays a significant role to reduce the pull-in voltage. The electrostatic actuation mechanism is mostly preferred because of the low power consumption, low switching time, and small electrode size, etc. [7]. This actuation mechanism requires very high pull-in voltage but does not consume any current which results in very low power dissipation (10-100 nJ). Other actuation mechanisms consume more current, dissipates high power, and probably result in stiction. The comparison of the actuation voltage obtained from different actuation mechanisms is given below in table 1. It is clear from the table that electrostatic actuation mechanism requires more actuation voltage than any other method.

Table 1: Pull-in voltage for different actuation mechanisms

Actuation mechanism	Actuation voltage (V)	Reference
Electrostatic	9-70	[82][93],[39]
Piezoelectric	2-12	[94], [95]
Electromagnetic	2	[96]
Electro-thermal	2.5-3.5	[97]

Polcawich R.G. et.al reported RF MEMS series switch using a piezoelectric actuation mechanism. The purpose of this switching design is to achieve a lower actuation voltage. He compared the results with a switch actuated using an electrostatic actuation mechanism. The proposed switch exhibits excellent RF performance and retains a large restoring force [94]. On the other hand, Lee et.al developed a cantilever-based RF MEMS shunt ohmic switch. The piezoelectric actuation mechanism was used and a low actuation voltage around 5 V was achieved [98]. A tuned cross switch with four membranes was demonstrated by Muldavin. The proposed switch structure aims to achieve good RF performance. The switch was well suited for low loss high isolation communication applications operated at 28 GHz [99].

2.2 Low spring constant structures-based RF MEMS switch

Pacheco et al. developed a low spring constant-based MEMS shunt capacitive switch using the Nickel as a suspended membrane. For the support of the suspended membrane, meander structures were used. The motive of low spring constant-based structure is to decrease the actuation voltage as pull-in voltage mainly relies on the shape and thickness of the fixed-fixed beam/cantilever structures. For the gap of 4-5 μm, a pull-in voltage of 6-20 V, isolation of -25 dB, and insertion loss of -0.1 dB was achieved at 1-40 GHz [100]. Afterward, several other methods were suggested by researchers to lower the actuation voltage.

In 2003, Peroulis et al. reported MEMS switches having an air gap of 4–5 μm and low pull-in voltage of 6–12 V. A serpentine folded meander configuration was fabricated and as the number of meanders was increased from 1 to 5, the pull-in voltage got reduced by 80%. The structure with 5 meanders attains a low actuation voltage of 3 V [101]. This success lead the researchers to design some different meander structures

to lower the pull-in voltage [102] but this approach prone to issues like sensitivity to mechanical force etc. [33].

The University of Michigan developed a low-height shunt switch with inline transmission line configuration using titanium/gold (0.8–1.0 μm) as a double clamped beam. The small air gap of 1.5–2.2 μm between the suspended beam and electrode resulted in the lower actuation voltage of 12–24 V. Only the air gap was reduced and the spring constant of the membrane was not changed. This switch structure exhibits advantages of fast speed, and a low response to the mechanical vibrations but with poor RF performance [33]. For the development of low voltage RF MEMS switch, Balaraman et al. proposed a design with various hinge (spring) structures using a high resistivity silicon substrate. The suspended beam of copper with four different hinge geometries was used [103]. The pull-in voltage and spring constant of hinge structures using different meanders cantilever are given in table 2. The cantilever with two suspension bridges is having the minimum spring constant values which in turn reduces the pull-in voltage.

Table 2: Different hinge structures

Hinge Structures	Pull-in voltage (V)	Spring constant (N/m)
Solid cantilever	17.8	16.7
2 meander cantilever	11.5	7.4
2 Suspension bridges (each suspension contains 1 meander)	5.7	1.75
4 Suspension bridges (each suspension contains 1 meander)	16.7	14.8

In 2003, Guo et al. reported a MEMS switch with low actuation voltage in which Al-silicon alloy was used as a suspended beam. Based on the suspended beam material and dimensions of elastic modulus, the optimization of the switch structure was realized by calculating the pull-in voltage. The results show that alloy exhibits a lesser pull-in voltage of 5 V than Au based suspended beam. But the alloy-based suspended beam exhibits higher transmission losses than the gold membrane [104].

Figure 6 shows another low voltage MEMS switch, developed by Lee et al. In this switch, electrostatic actuation is used for the movement of the freely moving contact structure. Since in the proposed design, the actuation voltage has not been used for

elastic deformation, the actuation voltage is reduced to a sufficient amount and 4.5 V is required for the actuation [105]. The internal stress gradient of the suspended beam material leads to the bending of the beam. To mitigate this issue, Kim et al. proposed a low voltage DC contact type RF MEMS switch. Thick and stiff Si membrane was used with seesaw mode operation. The gap between the electrode and the beam is small and uniform [106].

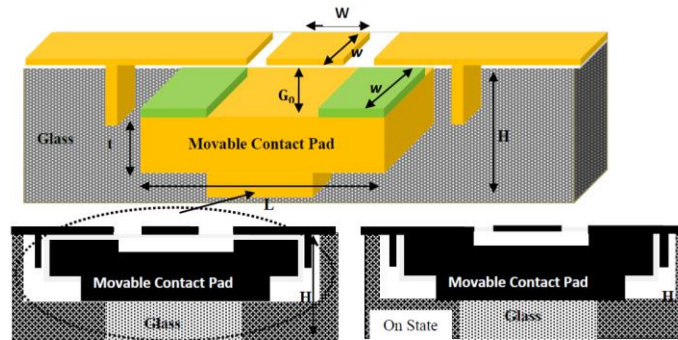

Figure 6: Schematic view of RF MEMS switch with movable contact pad [Lee et al.]

Another design of RF MEMS switch with low voltage and high switching speed was reported by Kundu et al. The concept of moving transmission line over CPW was used to lower the actuation voltage. In this study, two moving plates are used, one plate is used as a membrane, and the other one as a CPW line. The CPW line acts as the bottom electrode to initiate the actuation. In this way, the actuation voltage and switching time reduced around 20 % [107].

Park et al. developed another low voltage MEMS shunt capacitive switch with a high capacitance ratio and good RF performance. The standard configuration double clamped beam structure was used to design the shunt capacitive switch by taking the dielectric layer of Strontium-Titanate-Oxide ($SrTiO_3$). For isolation, $SrTiO_3$ has a very high relative dielectric constant of 30–120. The pull-in voltage of 8-15 V and isolation of -40 dB was achieved. Also, high dielectric constant value results in a high capacitance ratio of 600 with 50 pF downstate capacitance and 70-80 fF upstate capacitance. The surface roughness of the dielectric layer reduces the capacitance ratio from 3000 (theoretical value) to 600 [108].

Other than the hinge structure, some researchers have developed low voltage MEMS switches without hinge or meander structure type beam. An anchorless bridge was developed by Shen et al. in which the bridge was hinged to the substrate by metal post.

The actuation voltage of < 10 V has been obtained for the developed switch structure [109].

A flexible bridge based ohmic switch was developed by Segueni et al. In the designed ohmic switch configuration, two pairs of electrodes were used and the electrodes were positioned on both edges of the supporting pillars. The voltage can be applied at any electrode for the switch operation. A very low pull-in voltage of 3.5 V was achieved. The switch exhibits good RF performance [110].

Sravani et al. reported an RF MEMS shunt capacitive switch with different shapes of meanders as shown in figure 7. The electromechanical analysis of free moving gold suspended beam and Si_3N_4 and HfO_2 as dielectric materials were performed in FEM based tool. The pull-in voltage of 2.3 V and 2 V was obtained for 0.8 µm and 0.6 µm thick beam. For 0.8 µm thick beam, capacitance ratio of 8.69 and 14.93 was obtained for Si_3N_4 and HfO_2 respectively. The non-uniform single meander structure exhibits insertion loss of −0.2 dB and isolation loss of −14 dB at 20 GHz. The obtained switching time of uniform three meander structure is 0.12 ms and that of the non-uniform one meander structure is 0.7 ms [111].

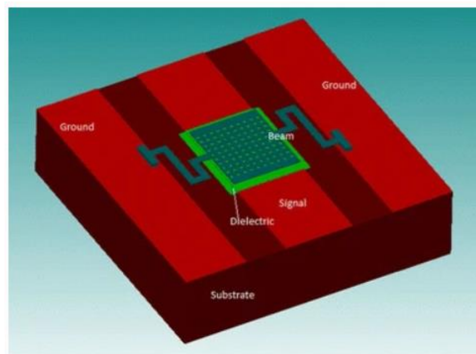

Figure 7: Meander structure proposed [Sravani et al.]

A step structure RF MEMS switch for K-band applications has been proposed by Sravani et al. The non-uniform meander structure for both optimized and non-optimized structures was implemented and analyzed to understand the performance characteristics of MEMS switch. In the K-band frequency range, the optimized non-uniform meander switch actuates at very low pull-in-voltage of 3.82 V, exhibits insertion loss less than -1 dB and high isolation of − 54.17 dB at the center frequency of 22 GHz [112].

To reduce the spring constant of the suspended beam, perforated beams can be used as a bridge in the MEMS switch. Rao et al. proposed a MEMS switch by taking different

beam materials of different thicknesses. Ashby's approach was used to select the best material for the MEMS switch. Silicon nitride was used as dielectric material and for beam material, the stiffness of gold, titanium, and platinum was analyzed. To reduce the pull-in voltage, meanders and perforations were introduced in the suspended beam. The pull-in voltage of 1.9 V was achieved. For X-band applications, the developed switch offers insertion loss of -0.147 dB and isolation of -52.04 dB at 8 GHz [113].

Chan et al. reported a low-voltage metal-to-metal contact shunt RF MEMS switch. The perforated suspended beam of gold actuated at 15 V and had switching speed of less than 25 µs. The metal sticking issue was removed by using separation posts that resulted in lifetimes of 1.6 x 10^6 cycles for hot switching and 7 x 10^9 cycles for cold switching. The results state that the lifetime of the switch improves on the order of a decade for every 5 to 7 V decrease in applied voltage [114].

Kageyama et al. proposed a new fabrication method to enhance the reliability and power handling capability of RF MEMS switch. The fabricated an Au–Au/CNT composite contact exhibited a low insertion loss of < 0.7 dB at 40 GHz and life cycle 2.7 times longer than that of an Au–Au contact switch [115].

Another MEMS shunt switch was proposed by Ansari et al. that has a unique spring design. Al metal was used as a suspended beam and 100 nm thick SiO_2 was used as the dielectric. To reduce the air gap, a step structure/helical spring was included in the switch design. This step structure/helical spring reduces the spring constant that further reduces the actuation voltage to 2.2 V. Analysis of the perforated beam along with helical spring contact pads was performed. For 1-40 GHz, isolation of − 71 dB and insertion loss greater than − 0.85 dB was achieved. When the beam was in upstate, the capacitance of 93.3 fF, and when the beam was in downstate, the capacitance of 2.64 pF had obtained. The overall ratio of the capacitances obtained was 28 for the simulated switch structure [116].

Another low voltage RF MEMS switch was presented by Attaran et al. as shown in figure 8. The switch consists of a 700 µm long and 30 µm wide helix spring structure connected to a perforated actuator. The perforated gold actuator of length 190 µm, width 220 µm, and thickness 70 nm was fabricated over alumina substrate. For a 1.5 µm gap, very low pull-in voltage, isolation of 27 dB, an insertion loss of 0.1 dB, and switching time less than 0.22 ms was obtained [117].

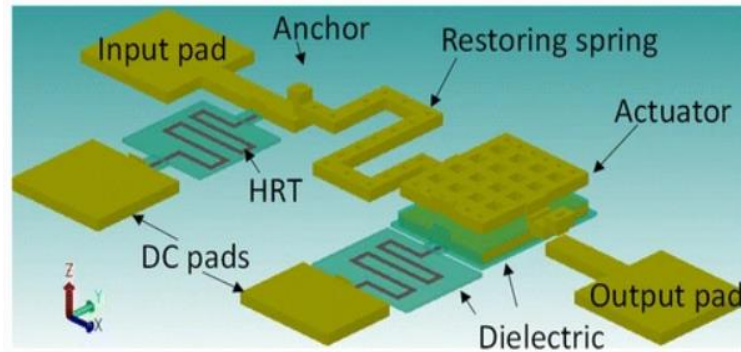

Figure 8: 3D view of helix spring structure MEMS switch

Angira et al. demonstrated a RF MEMS switch with non-uniform bridge structure. The design comprised of four flexures with two wider beams that were further joined to central capacitive area. For the designed switch structure, pull-in voltage of 10.5 V, pull-in time of 76.59 µs, and the release time of 32.76 µs were achieved. In the S-parameters analysis, insertion loss greater than 0.44 dB for X-band while 0.71 dB for Ku band was obtained. Similarly, the isolation of 15 dB was obtained for the frequency range of 10.3 to 40 GHz [118].

2.3 High-κ dielectric based RF MEMS switch

High-κ dielectric material is used to improve the RF performance of the MEMS switches at high frequency and also high-κ dielectric material increases the downstate capacitance. The most commonly used dielectric material is silicon nitride. Park et al. developed a MEMS capacitive switch with a very high capacitance ratio. A double clamped beam using strontium-titanate-oxide ($SrTiO_3$) as dielectric material was presented. The actuation voltage of 8-15 V, capacitance ratio of 600, isolation of -40 dB, and insertion loss of -0.1 dB at 10 GHz was obtained [108].

Zhang et al. developed RF MEMS shunt capacitive switch with HfO_2 for isolation. The results show that a thin layer of dielectric material provides better isolation for the frequency range of less than 20 GHz. The insertion loss of -0.8 dB and isolation of -30 dB was achieved at 50 GHz. But due to some fabrication imperfections, the material exhibits leakage current and reduced the quality of dielectric material [119].

The mixture of Alumina and Zinc oxide can be another choice to use as a dielectric material for MEMS switch. Herman et al. used the atomic layer deposition method for the deposition of dielectric material. The calculated value of Al_20_3/ZnO alloys films

was 7. The MEMS switch exhibits low insertion loss of 0.35 dB and high isolation of 55 dB at 14 GHz respectively [120].

A new method of using a multi-layered dielectric material layer of PZT/HfO_2 in the MEMS switch was developed by Tsaur et al. PZT/HfO_2 has a very high dielectric constant value of 79-82. The leakage density of multi-layered dielectric material is low. RF MEMS switch with multi-layered structure shows high isolation (−30 to −65 dB) and low insertion loss (−0.5 dB) for different frequency bands [121].

Another choice as a dielectric material for the metal-insulator-metal (MIM) switch is Barium Strontium Titanate (BST), proposed by Yoon et al. For the thickness of 150 nm, the dielectric constant of BST is 367. An actuation voltage of 7-18 V was achieved. The RF performance of the proposed switch shows improvement compared to using silicon nitride as a dielectric layer [122].

Persano et al. studied the potential of tantalum nitride (TaN) and tantalum pentoxide (Ta_2O_5) to be used as actuation pads and dielectric layers, respectively, for MEMS switch. RF MEMS shunt capacitive switch was developed using III–V technology materials to overcome the technical limitations and to ensure the reliability of the switch. An actuation voltage of 15-20 V, isolation of -40 dB, and insertion loss of -0.8 dB up to 30 GHz were achieved [123]. Bonthu et al. presented the dielectric material selection method for RF MEMS switch. To optimize the performance indices like dielectric charging, RF performance, stability and hold down voltage, Ashby's material selection method was used. The performance indices are evaluated by choosing material indices of the dielectric layer. From the selection chart of the method, it is evident that Al_2O_3 and SiN can be used without any hesitation as these dielectric materials provide good performance at RF [124].

Guha et al. investigated the high capacitance ratio of RF MEMS shunt capacitive switch. In this work, different meander structures have been used and comparative analysis has been performed. The proposed switch having 0.8 μm thick gold beam material was designed for 5-40 GHz frequency range. The simulation study of the switch illustrates that high dielectric constant materials enhances the capacitance ratio. A pull-in voltage of 2.45 V and capacitance ratio of 223 was obtained for HfO_2 while a pull-in voltage of 2.7 V and capacitive ratio of 83.75 was obtained for Si_3N_4. A low

insertion loss of −0.4 dB and high isolation of 80 dB at 20 GHz were achieved. The study reveals that non-uniform design reduces design complexity [125].

Angira et al. presented RF MEMS shunt capacitive switch with high-κ dielectric for telecommunication applications. In the reported work, HfO_2 has been used in place of SiO_2. The central overlap area in the case of HfO_2 reduces to 8 times less and the switch size reduced by 15% as compared to the SiO_2 based switch. High-κ dielectric based MEMS switch shows a pull-in voltage of 12 V, isolation of 52.70 dB, and insertion loss of 0.06 dB at 9 GHz [126].

Design and analysis of RF MEMS switch using GaAs as dielectric material was reported by Thalluri et al. Al beam of 1 µm thickness and 380 µm length was used along with 50 nm thick GaAs dielectric material. The gap between the suspended beam and electrode was kept 1.6 µm. A pull-in voltage of 8.12 V, isolation of -41.5 dB, and insertion loss of 0.6 dB at 27 GHz were achieved. An overall capacitance ratio of 368.9 was obtained for a dielectric constant of 12.9 [127].

2.4 Fabrication processes-based RF MEMS switch

The surface micromachining method is mostly used as compared to bulk micromachining for the fabrication of the RF MEMS switch. The fabrication of the MEMS switch can be done by using an integrated circuit CMOS process. Though it requires a few additional steps to release the bridge structure. Using this process, the integration of switch with other circuit components can be easily done.

Using the CMOS process, Dai et al. has proposed a RF MEMS shunt capacitive switch which comprised of a metallic beam that was suspended at some height over the CPW line. In the post-process, the Silox Vapox III etchant was used for releasing the metallic bridge by removing the oxide layer. The developed MEMS switch actuates at 17 V and at frequencies of 10-40 GHz, the switch exhibit loss of -2.5 dB when the switch was inserted in the transmission line [128].

Lee et al. developed a CMOS RF MEMS capacitive switch using different methods of actuation. Both electrostatic and electro-thermal actuators were used for the actuation mechanism. Standard 0.35 µm 2Poly-4 Metal of CMOS process was used to develop the MEMS switch. For the post-processing, maskless wet and dry etching techniques were used. Silox Vapox III was used as an etchant for wet chemical etching to release

the suspended beam. Metal layers were used as membrane and CPW lines while the polysilicon layer was used for an electro-thermal actuator. The switch exhibits a pull-in voltage of 7 V, isolation of −4.1 dB, and insertion loss of −2.5 dB at 5 GHz [129].

Lai et al. demonstrated another BiCMOS embedded RF MEMS switch. In this work, a novel back-side processed back to front self-aligned MEMS switch was fabricated for 90 to 140 GHz frequency band. In the high-performance BiCMOS process, only one mask step was added that offers low cost wafer-level packaging. For the fabricated switch, a pull-down voltage of 40 V, switching on time of 10 μs, an insertion loss of less than 0.5 dB up to 140 GHz, and isolation of 15 dB for 90 to 140 GHz were achieved [39].

Kaynak et al. developed a BiCMOS embedded RF MEMS capacitive switch. The proposed switch has been successfully characterized using FEM. A FEM based mechanical model of the switch was developed initially by taking the residual stress of the thin film membrane into account. The membrane of the switch was realized using the stress compensated Ti/TiN/AlCu/Ti/TiN M3 stack and SiN was used as a dielectric layer. The switch offers actuation voltage of < 20 V, isolation > 20 dB, and insertion loss < 5 dB at 60-70 GHz. The study of the developed switch demonstrates the feasibility of using the FEM model in circuit simulations for the development of RF MEMS switch integrated single-chip multi-band RFICs [130].

The failure of ohmic contact switches occurs in the form of damage, pitting, or hardening of the contact material. While in capacitive switches, the failure occurs due to stiction between the dielectric and metal beam. Bansal et al. reported a novel torsional RF MEMS capacitive switch as shown in figure 9. The proposed design is based on a small overlap area which is less prone to stiction and enhances reliability. The floating metal concept is adopted to reduce the on-state capacitance and it in turn minimize the leakage current. For X-band applications, the torsional switch exhibits a pull-in voltage of 20 V, capacitance ratio of 1755 along with insertion loss of 0.1 dB and isolation of -43 dB. The switching speed of the MEMS switch gets improved from 56 to 46 μs [131].

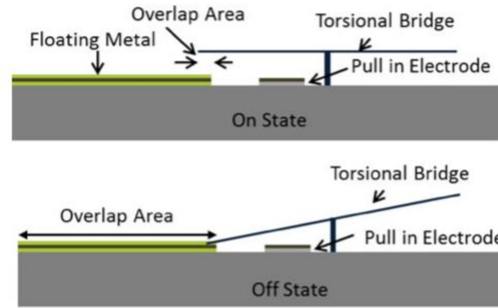

Figure 9: Working of Torsional bridge switch

The investigation of electrostatically actuated RF MEMS switch using gold material as a suspended beam was performed by Persano et al. In this study, pull-in voltage and the capacitance associated with the bridge in both on and off states were evaluated for 300 nm thick silicon nitride as a dielectric. The switch got actuated at 6 V when the displacement of 2.5 µm was achieved by the suspended beam. The study illustrates that Poole-Frenkel effect plays a significant role in the conduction when the beam actuates [132].

In the RF MEMS switch, to release the hanging bridge structure, either dry release method or wet release method is used. The first method i.e. dry release method uses high-temperature processes that curls up the bridge while in the second method, the surface of the released device gets contaminated and it spoils the switch performance [133]. Mehta et al. integrated two processes i.e. a dry and wet method to release a stiction-free suspended beam. Plasma cleaning was used to remove the contamination. Using a mixed dry, wet method of release for the switch having a gold suspended beam, the obtained pull-in voltage was 24 V, isolation of 22 dB, insertion loss of 0.1 dB at 10 GHz [133].

Thalluri et al. have fabricated a perforated serpentine beam using a surface micromachining process. For design and analysis, simulation study has also been performed and the fabricated switch has also been characterized. The results of the simulation study and characterization were obtained and compared. The surface micromachining process with four masks was used for the fabrication. Gold was used as a suspended membrane and 50 nm thick AlN was used as a dielectric material. The perforated membrane provides high isolation of - 58.5 dB and very low insertion loss - 0.4 dB at 31.5 GHz. The fabricated switch of 500 nm thick Au beam having a perforated

serpentine structure with non-uniform meanders actuates at a very low voltage of 4.5 V [134].

2.5 RF MEMS switches developed for specific bands

Compared to the semiconductor switches, the RF MEMS switch delivers high linearity and consumes very less power. But the power handling capability is very poor. Stehle et al. developed a Ku band RF MEMS switch for high power handling. A low loss and less complex RF MEMS switch was designed for a small signal operation that can handle power up to 6 W in hot switching mode. The design actuates at 35 V, exhibit isolation of -21 dB and insertion loss of -0.2 dB at Ku band [135].

Vu et al. presented the design of RF MEMS switch to integrate with tunable filters for W to V-frequency band applications. A gold cantilever of 2 µm thickness and 3 µm air-gap with dimple structures has been used in the tunable resonator. The fabrication imperfections lead to the curling of the cantilever in the upward direction that increases the pull-in voltage to 80 V. In the RF analysis, isolation of 15.10 dB and insertion loss of 1.23 dB at 60 GHz were obtained [136].

The proper choice of the configuration of the switch allows high input RF power by reducing the probability of self actuation. Jhanwar et al. proposed a high-power handling applications-based metal contact switch by considering two design aspects. First is the configuration of the switch and second is the shape and location of the contact spots. The simulated switch actuates at 19 V, shows an isolation of -32.5 dB and insertion loss of -0.1 dB at 10 GHz. Without considering the temperature conditions, the switch can handle power up to 15.6 W [137].

Quaranta et al. designed, fabricated, and characterized a RF MEMS shunt capacitive switch for K-band applications. The size of different parts of bridge was varied to find out the resonant frequency. The switch was fabricated using surface micromachining process while surface profilometry was used to measure the thickness of different layers. The estimated spring constant of the gold bridge was 30-34 N/m. The deposition of floating metal reduces the isolation from -42 dB to -35 dB [138].

Savin et al. presented RF MEMS switches with the different geometrical designs for X-band. The different geometrical designs and their concept are compared in terms of complexity and RF performance parameters. For switch fabrication, sapphire has been

used as a substrate. A perforated copper beam of 1 µm thickness and 0.3 µm thick silicon nitride have been used. For the air gap of 2 µm, a pull-in voltage of 15 V and 7 V were achieved for different structures. At RF, an insertion loss of -0.5 dB and isolation of < -20 dB were obtained for the frequency range of 6 GHz-12 GHz [139].

A multiport RF MEMS switch for satellite payload applications was designed and fabricated by Subramanian et al. The single input multiple output topology was used to design the switch suitable for satellite payload applications that can work on both dual-mode and quad-mode. A pull-in voltage of 4.5 V was obtained for the designed switch. The designed switch configuration exhibits isolation of > -50 dB and -60 dB at 12 GHz for dual-mode and quad-mode respectively. While the insertion loss of -2.5 dB at 10.5 GHz and -4 dB at 15 GHz was achieved for dual-mode and quad-mode respectively [140].

Chu et al. presented a low loss, high isolation, good reliability, and high-power handling RF MEMS switch based on GaAs microwave monolithic integrated circuit (MMIC) technology. For the proposed design, impedance matching of the switch was acquired by a T-matching structure. A gold bridge with a length of 300 µm actuates at a pull-in voltage of 36 V and shows improved isolation from 20 dB to 35 dB and exhibit insertion loss of < 0.3 dB over Ka-band [141].

2.6 Development of NEMS switches

The advantages of carbon materials make graphene and carbon nanotubes promising materials for new generation RF NEMS switches. The era of miniaturization has evolved the NEMS switches using graphene material because of its demand for low power consumption applications. Milaninia et al. fabricated a NEMS switch comprised of two polycrystalline graphene films. The films were deposited using a chemical vapor deposition (CVD) method. One graphene film acts as suspended beam while the other as the bottom electrode. The switch actuated at 5 V and after switching several times, the contact got broken. The reliability of the switch can be improved by scaling the device area within one crystalline domain of graphene film [56].

Kim et al. fabricated and characterized a suspended few-layer graphene-based NEMS switch. The beam of length 20 µm, width 2 µm, and the gap of 0.15 µm got actuated at 1.85 V. Based on Rebeiz's model, the estimated switching time was 40 ns

[142]. Shi et al. demonstrated an electrostatically actuated NEMS switch using multilayer graphene as a suspended beam. Multilayer graphene NEMS switch acquires an on-off ratio of 10^4 with a life cycle of 500 cycles [57].

Graphene has attracted the attention of researchers vigorously in the development of NEMS switches. The performance analysis of a graphene-based RF NEMS capacitive switch was reported by Pankaj et al. in 2013. The analysis of monolayer and multilayer graphene NEMS switch was done and 20 nm thick Hafnium dioxide was used for dielectric material. A pull-in voltage of less than 2 V and switching time of 240-430 ns were obtained. For monolayer graphene at 1-60 GHz, an insertion loss of 0.01–0.3 dB and isolation of >10 dB was obtained. For multilayer graphene, in the same frequency range, an isolation of >20 dB and insertion loss of 0.01–0.2 dB was obtained. The monolayer graphene undergoes quite high losses compared to multilayer graphene. From the results, it can be demonstrated that graphene can be used for applications that demand high switching speed NEMS switch with low actuation voltage. But it suffers from large electromagnetic losses as compared to metal-based switches [21].

Mafinejad et al. reported the properties of graphene for RF M/NEMS applications. The mechanical behavior of metallic switches and graphene was compared. The simulation study demonstrates that graphene-based NEMS switch actuates at a faster speed than metallic switches with less pull-in voltage. Graphene NEMS switches are expected to exhibit high reliability and avoid stiction problems [143].

Li et al. reported the growth of monolayer, bi-layer, and tri-layer single-crystalline graphene (SCG) using the CVD method. Atomic force microscope and Raman spectroscopy methods were used to characterize and verify the mechanical properties and crystalline nature of SCG. NEMS switches based on monolayer and bilayer SCG were fabricated. A pull-in voltage of 1 V and a switching speed of 100 ns were obtained. This fabricated NEMS switches exhibit a lifetime of 5000 cycles [144].

Another RF nano switch using single-crystalline graphene as bridge material was reported by Li et al. Low-pressure chemical vapor deposition (LPCVD) method was used for the growth of SCG. SCG based switch exhibit a higher lifetime (5000 cycles) than polycrystalline graphene (PCG) switches. The switch exhibits a very low pull-in voltage of 1 V and good isolation of -30 dB at 40 GHz. The flat structure of SCG resolves the problem of the metal fence [145].

The structural and electrical properties of multilayer graphene were thoroughly discussed by Moldovan et al. A double clamped multilayer graphene was fabricated and the RF performance of the fabricated switch was analyzed. For multilayer graphene, actuation voltage of 10 V and switching time of 1.56 µs were evaluated by measurements. A capacitance ratio of 10.7 was obtained. At 6 GHz, an insertion loss of -1.6 dB and limited isolation of -1.75 dB were obtained in the study. The RF performance of the graphene NEMS switch can be enhanced by improving the fabrication process [146].

Zulkelfi et al. reported the optimization of design parameters of graphene NEMS switch to achieve low pull-in voltage. The beam length was varied from 0.5-2 µm and the air gap from 0.05 -2.5 µm. For 1 nm thick and 0.2 µm wide graphene beam, the minimum pull-in voltage obtained was 2 V. The design and analysis of NEMS switch demonstrate that device optimization procedure is important to achieve better performances of the device before proceeding to the fabrication process [147].

Zulkefli et al. reported the switching and mechanical reliability of both the standard and perforated graphene beam structures. In electromechanical switching, analysis of actuation voltage, mechanical reliability, and von Mises stress were performed using FEM based tool. In both the beam structures i.e. standard and perforated beam, the actuation voltage of 2 V and 1.5 V were achieved. The study shows that a long and thin beam requires less actuation voltage and undergoes less von Mises stress. Using a perforated beam, both pull-in voltage and von Mises stress get reduced [148].

Anjum et al. reported the design and simulation of contact type RF NEMS switch with low actuation voltage and enhanced RF performance. The design and analysis of the NEMS switch have been performed in ANSYS software by taking graphene and MoS_2 as suspended beam material. The simulated NEMS switches exhibit low actuation voltage of less than 1 V. Both multilayer graphene and MoS_2 based RF NEMS switches exhibit isolation of -62 dB at 7 GHz and insertion loss of -0.03 dB at 14 GHz. It is evident from the results that low voltage RF NEMS switch can be realized using 2D materials [149].

Table 3 summarizes the performance of already existing RF M/NEMS switches. Based on results, it can be concluded that GO can be used as a suspended beam as GO-based RF NEMS switch provides very good isolation and low insertion loss.

Table 3:Performance of switches having different dimensions and different materials

References	Beam Material/dielectric	Pull-in voltage (V)	S-parameters
Yao et al. 1995	Gold/SiO_2	28	Isolation= -50 dB Insertion loss= 0.1 dB @4 GHz
Goldsmith et al. 1996	Al	50	Insertion loss = 0.14 dB
Goldsmith et al. 1998	Al/Si_3N_4	30-50	Isolation= -35 dB Insertion loss= -0.7 dB @ 10-40 GHz
Muldavin et al. 1999	Au/Si_3N_4	15-20	Isolation= 50 dB Insertion loss= < 0.6 dB @ 22-38 GHz
Chang et al. 2000	Al-Cr	26-30	Isolation=-17 dB Insertion loss=-0.2 dB @10 GHz
Pacheco et al. 2000	Ni/Si_3N_4	6-20	Isolation=-25 dB Insertion loss=-0.1 dB @1-40 GHz
Park et al. 2001	Au/STO	8-15	Isolation= -40 dB Insertion loss=-0.1 dB @10 GHz
Yoon et al. 2001	---/BST	7-18	--------------------------
Schauwecker et al. 2002	Au/--	16	Isolation=-22 dB Insertion loss=-0.85 dB @ 30 GHz
Peroulis et al. 2003	Ni	6-12	Insertion loss=-0.1 dB @ 40 GHz
Rebiez 2003	Ti-Au	12-24	--------------------------------------
Guo et al. 2003	Al-Si alloy	5	Insertion loss < 10 dB @ 1-15 GHz
Nishijima et al. 2004	Au	30	Isolation = -29 dB Insertion loss = -0.2 dB @ 2 GHz
Tsaur et al. 2005	PZT/HfO_2	<20	Isolation = −30 to −65 dB at 50 MHz-57GHz Insertion loss = < −0.5 dB at 50 MHz–20 GHz
Zhang et al. 2006	HfO_2	--------	Isolation = -30 dB Insertion loss = -0.8 dB @ 50 GHz
Herman et al. 2007	Al_20_3/ZnO	--------	Isolation= 55 dB @ 14 GHz Insertion loss = 0.35 dB @ 14 GHz
Segueni et al. 2007	Au	3.5	Isolation= -30 dB Insertion loss= -0.45 dB @ 10 GHz
Lee et al. 2008	Au	7	Isolation= -4.1 dB Insertion loss= -0.25 dB @ 5 GHz
Park et al. 2009	Copper/SiO_2	25	Isolation= 30.1 dB Insertion loss= 0.29 dB @ 5 GHz
Kaynak et al. 2010	Metal/SiN	<20	Isolation > 20 dB Insertion loss < 5 dB @ 60-70 GHz
Lai et al. 2011	Metal	40	Isolation=15 dB @90-140 GHz Insertion loss= 0.5 dB up to 140 GHz
Persano et al. 2011	Ta_2O_5	15-20	Isolation = -40 dB Insertion loss = -0.8 dB @ 30 GHz
Vu et al. 2012	Gold	80	Isolation = 15.1 dB Insertion loss = 1.23 dB @ 60 GHz
Sharma at al. 2013	Graphene/ HfO_2	< 2	Monolayer, Isolation= >10 dB, Insertion loss= 0.01–0.3 dB @ 1-60 GHz

			Multilayer, Isolation= >20 dB, Insertion loss= 0.01–0.2 dB @ 1-60 GHz
Jhanwar et al. 2014	Gold	19	Isolation= -32.5 dB Insertion loss= -0.1 dB @ 10 GHz
Moldovan et al. 2015	Graphene	10	Isolation= -1.6 dB Insertion loss= -1.75 dB @ 6 GHz
Singh et al. 2015	Gold/HfO_2	22.5	Isolation= 75 dB Insertion loss= 0.13 dB @ 28 GHz
Guha et al. 2016	Gold/Si_3N_4 and HfO_2	2.45, 2.7	Isolation = 80 dB Insertion loss= −0.4 dB @ 20 GHz
Anjum et al. 2018	Graphene	<1	Isolation= -62 dB @ 7 GHz Insertion loss= -0.03dB @ 14GHz
Mehta et al. 2018	Gold/SiO_2	24	Isolation= -22 dB Insertion loss= -0.1 dB @ 10 GHz
Ansari et al. 2019	Al/SiO_2	2.2	Isolation= 71 dB Insertion loss= 0.85 dB @1-40 GHz
Thalluri et al. 2020	Gold/AlN	4.5	Isolation= -58.8 dB Insertion loss= -0.4 dB @ 31.5 GHz

2.7 Research Gaps

Based on the conclusions drawn from the systematic literature review, following research gaps have been identified:

- The mechanical switches can be used for high power handling but are heavy and slow. On the other hand, semiconductor switches exhibit high speed, poor RF performance and consumes high power. Si-FET can handle high power at LF but at HF the performance decreases. MEMS switches can provide the advantage of both the switches but requires high actuation voltage and exhibits low switching speed. So, a switch structure that exhibits low pull-in voltage, light in weight, better RF performance, and high switching speed is desirable.
- In the FET devices, leakage current is high because the device dimensions are scaled down which results in poor device performance. To minimise the leakage current, a switch that requires physical contact for current flow from one port to another port is indispensable.
- The implementation of logic gates using CMOS components is intricate as it requires large number of components. To overcome this complexity associated with formulation of logic gates, it is necessary to build digital gates with fewer components.
- Graphene based NEMS switches requires low pull-in voltage, but at the expense of large losses. Also, the very high elastic modulus makes graphene beam stiff

and owing to the buckling issue. This problem can be addressed by taking another graphene derivative with low elastic modulus value that makes beam more flexible and less stiff.

2.8 Problem Formulation

Based on the RF MEMS switch structures, fabrication methods, different materials used as a suspended beam, different switch structures have different pull-in voltages and different RF performances. The design of an RF M/NEMS switch that meets all the desired requirements is still challenging. Based on the available literature and research gaps mentioned above, the following objectives are formulated.

1. Realization of NEMS shunt switches using Graphene/Graphene derivative as beam material.
2. Stress and pull-in response analysis of designed switch using Finite Element Modelling.
3. S-parameter analysis of RF NEMS switch to find out capacitance value for both up and downstate of beam.
4. Evaluation of RF NEMS switch performance by optimizing the parameters.

Chapter 3

FEM MODELLING OF GO BASED NEMS SWITCH

In this chapter, 3D design and analysis of a novel configuration of the NEMS shunt capacitive switch is discussed. Broadly, this chapter is divided into two parts. In the first section (section 3.1), GO-Graphene has been considered for double clamped structure. The design parameters like pull-in, pull-out voltages, and von Mises stress have been analyzed using COMSOL Multiphysics. FEM modelling of standard/intact beam and perforated beam has been performed. While in the second section (section 3.3), GO with gold has been considered a suspended beam. In this section pull-in voltage, and eigenfrequency analysis are presented for the intact and circularly perforated beam.

3.1 Device Geometry Description of double clamped GO-Graphene

In this study, GO has been used as dielectric material along with a suspended graphene beam for the first time. For the operation of the NEMS switch, two graphene electrodes were used. One graphene electrode (actuator) was situated under the GO beam (5 nm thick) and another graphene electrode (3 nm thick) was placed just above the GO beam. In FEM simulations, GO (dielectric) was used as beam material and two graphene electrodes were used, one as an actuating electrode, and another as a ground electrode.

To exclude the effect of intermolecular forces the air gap cannot be decreased to very low values (< 30 nm) [150]. The suspended beam is mounted over a lossless transmission CPW line of 50 Ω. The beam length cannot be increased much as it alters the width and slot spacing of CPW. Also, the if the beam thickness is less than twice of skin depth than the switch resistance remains constant with the frequency [33]. So, for the proper operation of switch, the beam thickness is considered twice of skin depth. These boundary conditions restrict the values of beam length, thickness and air gap.

The simulations were performed for both standard and perforated beam structures. The simplified diagram of the double clamped GO NEMS switch is illustrated in figure 10. The top view of the perforated GO beam is illustrated in figure 11.

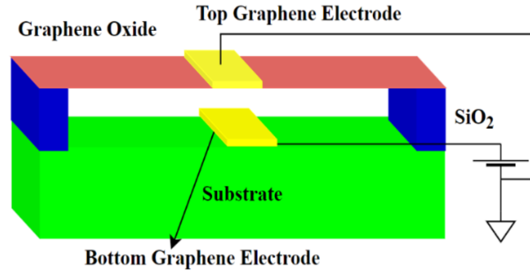

Figure 10: Simplified figure of GO NEMS switch

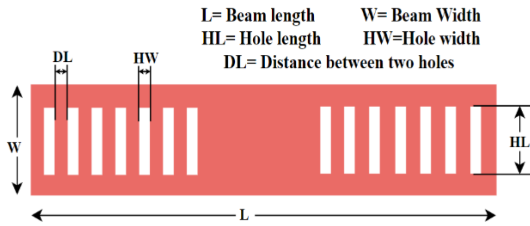

Figure 11: Top view of perforated GO beam

The suspended beam dimensions of GO NEMS switch and perforated GO NEMS switch are given in table 4.

Table 4: Dimensions of standard and perforated GO beam

Parameters	Values
Beam length	1 µm
Beam width	0.3 µm
Beam thickness	2.8 nm
Gap between beam and bottom electrode	30 nm
Actuation electrode area	200*300 nm
Distance between two perforations (DL)	80 nm
Perforation length (HL)	30 nm
Perforation width (HW)	200 nm

3.1.1 Pull-in analysis

In the proposed switch configuration, for operation, the electrostatic actuation mechanism has been used for pull-in analysis. The electrostatic actuation mechanism was achieved by applying a voltage at the bottom graphene electrode and ground potential at the top graphene electrode. The voltage value at which sudden deflection in the beam is observed is known as pull-out voltage/lift-off voltage [151].

The pull-in voltage depends upon the spring stiffness, area of the actuation electrode, and the gap between the suspended beam and bottom electrode. The purpose of the perforated GO beam is to further reduce the pull-in voltage.

3.1.2 FEM simulations of GO-based NEMS switch

The huge geometries governed by the laws of physics for space and time-dependent problems become very complex to be solved with analytical methods. As an alternative, based on different types of discretization, the approximation of the equations of the analytical methods can be done [152]. The complex equations of analytical methods can be solved using numerical methods. The solution obtained by numerical model equations is an approximation of the real solution. Such approximations are computed by FEM [153].

In this study, FEM based tool COMSOL Multiphysics has been used to perform NEMS switch simulations. The modelling of FEA is accomplished in three steps: Pre-processing, Solver, and Post-processing [154]. In the pre-processing step, modelling of the structure is done. Pre-processing involves some sub-steps like the creation of geometry, assigning the material, selecting the physics, setting up the physics, and applying boundary conditions. Subsequently, the meshing of the device takes place in which the structure is divided into several finite elements. Then set of algebraic equations is solved. These equations provide nodal solutions related to physics. All the solutions of mathematical equations and finite element formulation occur in the software. In COMSOL Multiphysics, two methods named segregated step method and fully coupled methods are used to obtain the model solutions. After generating the solutions, post-processing allows the user to evaluate and plot the results. Figure 12 shows basic steps to perform FEA in COMSOL.

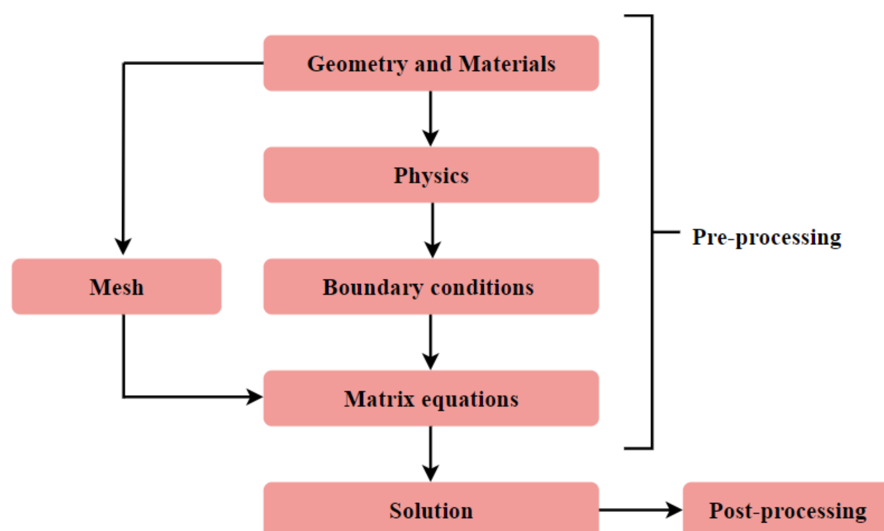

Figure 12: Basic steps of finite element method

In brief, it can be said that FEM is a numerical method for solving complex engineering and mathematical problems. The large problem is subdivided into smaller parts that are known as finite elements. The results of the solved problems are analyzed hence it is termed as FEA. The two physics namely, Solid mechanics (under Structural Mechanics module) and Electrostatics (under AC/DC module) were used for the entire analysis of RF NEMS switch.

The Structural Mechanics module consists of the physics interfaces that are used for analyzing deformations, stresses, and strains of solid structures. In this different analysis like Stationary, Eigenfrequency, Transient, Frequency response, and Linear Buckling are available. The Solid Mechanics interface is intended for general structural analysis of 3D, 2D, or axisymmetric bodies. Based on the solution of Navier's equations, Solid Mechanics interface computes displacements, stresses, and strains.

The AC/DC interfaces are used to compute the electric and magnetic fields in static and low-frequency systems. AC/DC interface can be used to model the electrical circuits, electric current conduction, and orbits of charged particles, etc. The Electrostatics interface computes the electric field, the electric displacement field, and potential distributions in dielectrics under conditions where the electric charge distribution is explicitly prescribed. For the electric field, this physics solves the Gauss's law by taking scalar electric potential as the dependent variable. Also, this physics can be used together with other physics like eigenfrequency, frequency-domain, small-signal analysis, and time-domain modelling.

To predict certain design parameters, analytical models are very helpful to get approximations in the dynamic and static behavior of M/NEMS devices. It enables the end user to perform Multiphysics simulations. Electromechanics is the governing principle of RF-M/NEMS switches. The design and simulation of the proposed switch have been performed in FEM based tool COMSOL Multiphysics in the air medium.

3D modelling of double clamped NEMS shunt switch using GO as beam material was performed in COMSOL Multiphysics version 5.4. For the first time, GO has been used as beam material in NEMS switches. To evaluate the pull-in, pull-out, and von Mises analysis, electromechanics module was used. For all FEM simulations, GO Young's modulus was set to 27 GPa and Poisson's ratio value was set to -0.567 [62]. Free tetrahedral triangular mesh was used to reduce meshing complexity. In air medium

at 1 atm pressure, the suspended GO beam was positioned on the top at a distance of 30 nm from the bottom graphene electrode. For the top electrode, graphene beam was positioned just above the GO beam and was kept at 0V. While the electric potential was applied to the bottom graphene actuating electrode. All remaining boundaries were electrically insulated. For comparative analysis, FEM simulations for graphene-based NEMS switch were also performed by taking the same device dimensions.

3.2 Results and Discussions

The simulations of NEMS switches have been performed by taking GO as beam material using FEM based tool. To compare the results with GO NEMS switch, simulation of graphene NEMS switch was also performed.

Figure 13 illustrates the results of von Mises stress analysis for intact/standard and perforated graphene NEMS switches. The obtained maximum von Mises stress values for the case of graphene and perforated graphene NEMS switches are 4.8 GPa and 3.86 GPa respectively. The von Mises stress occurs maximum at the beam edges and minimum at the beam center. The von Mises stress is very high (GPa) in graphene NEMS switch. So, the beam is replaced by GO beam along with graphene electrode.

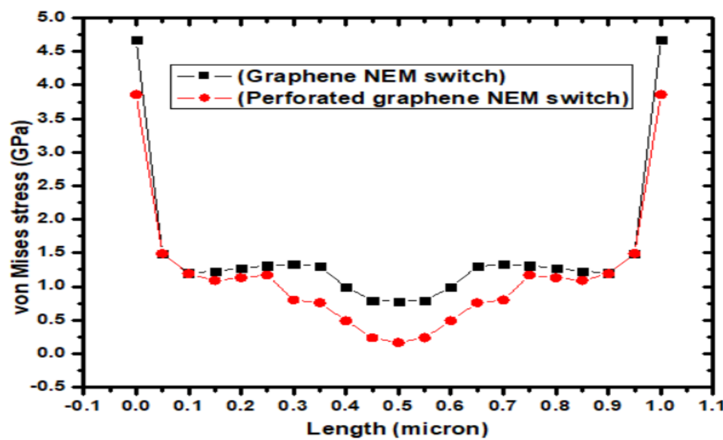

Figure 13: The von Mises stress of graphene NEMS switch with and without perforations

3.2.1 Standard and perforated beam structure

Under the effect of electrostatic actuation, if the suspended beam crosses the one-third distance of the gap between the top and bottom electrodes, the pull-in phenomenon starts to occur [32]. At actuation voltage, the beam snaps down completely and touches the bottom electrode. As the applied voltage is reduced, the effect of electrostatic forces decreases. This, in turn, causes the GO beam to deflect towards the initial position.

For the device dimensions mentioned in table 4, pull-in voltage of 5.4 V, pull-out voltage of 3.15 V, and maximum von Mises stress of 500 MPa were achieved. Figure 14 shows the total displacement when the beam was in contact with the actuating electrode due to the actuation mechanism.

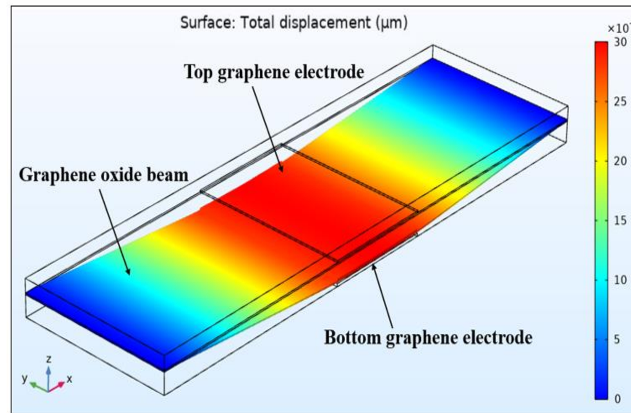

Figure 14: Schematic diagram of standard beam structure in downstate

To observe the effect of introducing perforations into the beam, FEM simulations of perforated GO beam were performed as shown in figure 15. For the device dimensions mentioned in table 4, pull-in voltage of 3.35 V, pull-out voltage of 2 V and maximum von Mises stress of 419 MPa was obtained. The pull-in voltage was reduced to 3.35 V from 5.4 V (without perforations) by introducing perforations into the beam.

The results show that making perforations into the suspended GO beam of NEMS switch reduces both, pull-in voltage and von Mises stress. Due to perforations, air below the suspended beam gets easily squeezed out when the beam is pulled down by the actuating electrode. Hence reduces pull-in voltage. As shown in the results, the pull-out voltage is lesser than the pull-in voltage [151].

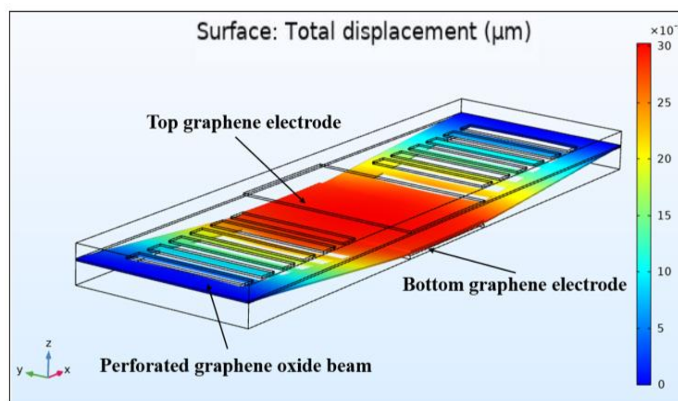

Figure 15: Schematic diagram of perforated beam in downstate

The change in von Mises stress along the beam length for both the GO NEMS switch structures is shown in figure 16. In standard beam structure, von Mises stress is maximum (500 MPa) at the beam edges and the beam center edges. But for perforated beam structure, von Mises stress is maximum (419 MPa) only at the beam edges, and at the center, it is having a lesser value (228 MPa). The von Mises stress exhibits intense effect at beam edges and the beam center due to edge termination effect. At the center, this value is almost half of the value of maximum von Mises stress in the case of the standard beam structure. Perforated beam structure reduces the von Mises stress acting on the suspended beam. In both cases, von Mises stress follows a specific trend. At beam edges and the beam center, von Mises stress is high but in between the edge and the center of the beam, von Mises stress value is low.

In GO and graphene NEMS switch, maximum von Mises stress occurs at the corner of beams. Interestingly, it has been observed that for GO NEMS switch, von Mises stress again increases at the beam center. This rise in von Mises stress is due to the presence of the upper graphene electrode. The interface at which graphene is situated above the GO beam suffers higher stress, as the beam at the center is thicker than the corner beam.

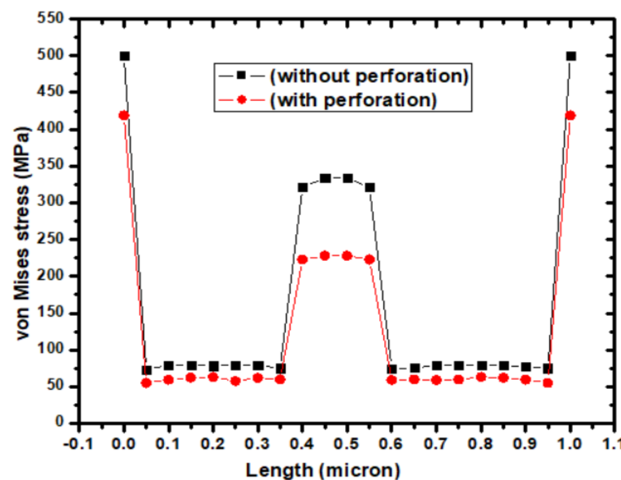

Figure 16: The von Mises stress of GO NEMS switch with and without perforations

In graphene NEMS switch, the maximum von Mises stress is 4.8 GPa while for GO NEMS switch von Mises stress is 500 MPa. The von Mises stress in GO NEMS switch is almost ten times lower than the stress in graphene NEMS switch.

Figure 17 shows the contour plot of von Mises stress in both standard and perforated beam structures. In standard beam structure, the maximum stress occurs at beam corners and the beam center edges while in the case of perforated structure, the maximum stress occurs at the beam corners and the perforation’s edges. The edges of the beam suffer maximum stress in both cases because electric field strength is very intense at the beam edge. Since GO is positively charged, it makes strong adhesion with negatively charged metals. Graphene is a zero bandgap material and it is the most conductive material [155]. Thus, the adhesion between graphene and GO supports the bonding of the upper graphene electrode and suspended GO beam. Also, the use of graphene along with GO increases the downstate capacitance [156].

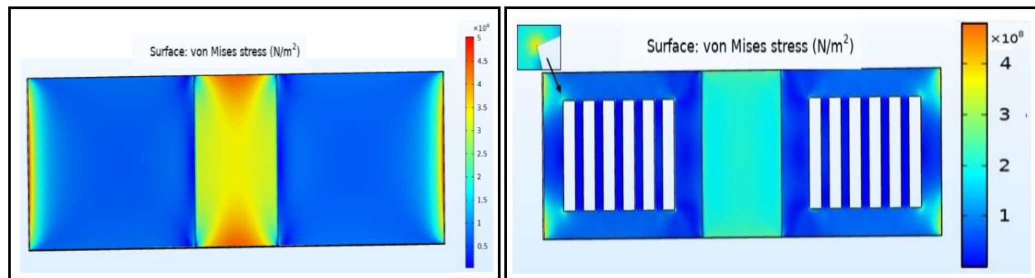

Figure 17: Contour plot of von Mises stress for standard and perforated GO beam structure

Figure 18, illustrates the electric field distribution in the actuated state of GO NEMS switch structure. The directions of the electric field are represented by the arrows. The bottom actuation electrode is represented by red color as the voltage is applied at the bottom electrode while the grounded top electrode is blue. The electric field lines move from the actuating electrode towards the ground electrode. The applied electric field is composed of a uniform field between the parallel plates and the fringing field exists at the edges of the plates [157]. The fringing field capacitance has a negligible effect on the pull-in voltage for the beam having a width greater than the air gap [158].

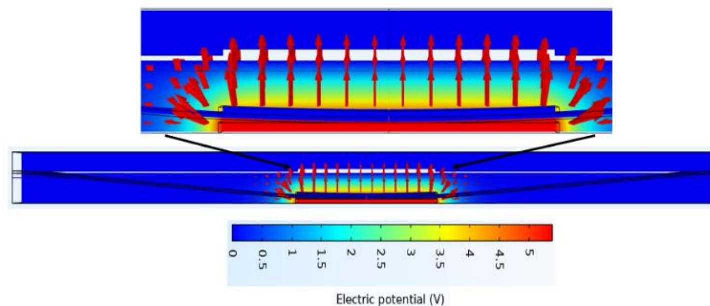

Figure 18: Electric field distribution GO beam structure

In the comparison of both graphene and GO NEMS switches, it is concluded that GO-based NEMS switch has less von Mises stress. So, the choice of GO as beam material over graphene is good. Since the results illustrate that perforated beam structure requires less actuation voltage and has less von Mises stress effect (at center), the perforated GO beam NEMS switch is better and more reliable than the standard GO beam NEMS switch.

From on state to off state of NEMS switch, variation in capacitance has been encountered as a graphene electrode was used just above GO. Depending upon the applied voltage, the distance between GO beam and bottom graphene electrode changes. At actuation voltage, when the beam touches the actuation electrode, it forms a capacitor structure. In NEMS switch, downstate capacitance is the sum of parallel plate capacitance (C_p) and fringing field capacitances (C_f) as shown in figure 19.

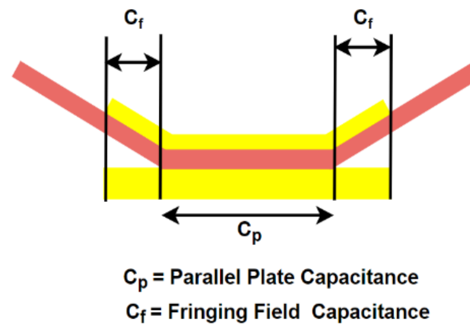

Figure 19: Total capacitance in downstate

As shown in figure 19, the slanting position of the GO beam with the bottom electrode gives fringing capacitance (C_f). The simulated results for fringing field capacitance are evaluated by integrating the capacitance values from the parallel plate capacitor edge to the bottom electrode edge. The value of C_f obtained on both sides ($2C_f$) is 359.2 aF. The simulated value of downstate capacitance ($C_d=C_p+2C_f$) is 0.9403 pF.

In figure 20, results of variation in capacitance value by varying applied voltage are presented for both standard and perforated GO NEMS switch. The voltage variation is done from 0.9 V to 5.4 V for standard GO NEMS switch. It results in a variation in the gap from 23 nm to 0 nm. For perforated structure, voltage variation is done from 0.9 V to 3.35 V that varies the gap from 20 nm to 0 nm. As the applied voltage is increased, due to the effect of electrostatic force, the beam gets pulled down towards the bottom electrode, and the gap between the beam and electrode decreases. When the applied

voltage is varied, the gap among the suspended beam and electrode changes, in response to that, different values of capacitance are obtained. When the applied voltage equals to the actuation voltage, the beam snaps down by the electrode and forms a capacitor structure. In standard and perforated GO NEMS switches, total capacitance obtained is 0.9403 pF when GO is completely in contact with the bottom electrode. As the device dimensions are the same for both the cases including GO, the total capacitance is the same at actuation voltages 5.4 V for standard and 3.35 V for perforated GO NEMS switches.

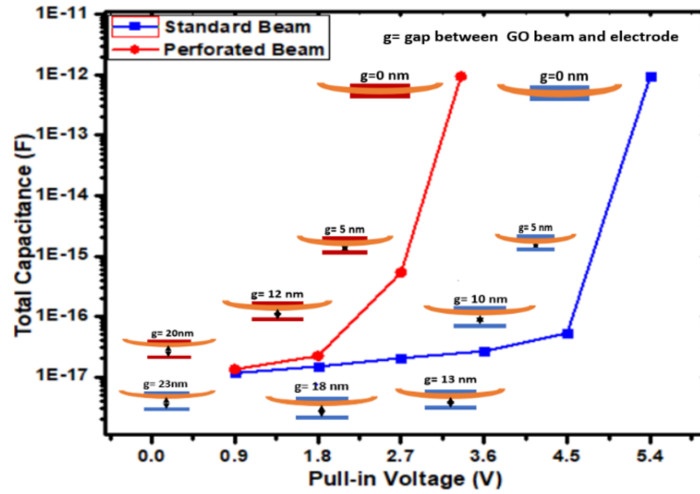

Figure 20: Variation in Capacitance plot for standard and perforated GO NEMS Switch

The simulated structure is feasible to investigate practically as researchers have successfully validated NEMS structures having the air gap < 30 nm [37][39]. Apart from that, packaging of the NEMS devices is very crucial for reliable operation. The process of packaging affects the size and associated cost of the fabricated device. Thin-film capping and chip capping are popular package methods for NEMS structures [40][41].

3.3 Device Geometry Description of double clamped GO-Gold

In this section, pull-in voltage and eigenfrequency analysis of a NEMS switch using gold/GO as beam material is presented. The switching operation of NEMS switch is achieved by the electrostatic actuation mechanism. For actuation, one gold electrode is used as bottom actuation electrode and another gold electrode is placed just above GO.

The pull-in voltage and eigenfrequency analysis for both intact and circularly perforated structures have performed.

FEA of GO-gold NEMS shunt switch has been performed in COMSOL Multiphysics. GO along with gold has been used as a double clamped suspended beam structure. The electromechanics module solves the coupled equations for electric field and structural deformation. For reducing the meshing size and computational time, free tetrahedral triangular mesh is used. In the air medium, the GO beam is positioned at the top and the gold electrode is positioned at the bottom. Electric potential is applied to the bottom gold electrode and the top gold electrode is kept at 0 V. The remaining boundaries are electrically insulated.

The schematic diagram of the GO-based NEMS switch is shown in figure 21 and the circularly perforated beam structure is shown in figure 22. In this switch structure, two gold electrodes are used, one is used as a bottom electrode at which voltage is applied. Another gold electrode is used just above the suspended GO beam. The top gold electrode is kept at ground potential. The geometrical dimensions of the suspended beam/bridge, electrodes, and circularly perforated beam are given in table 5,6.

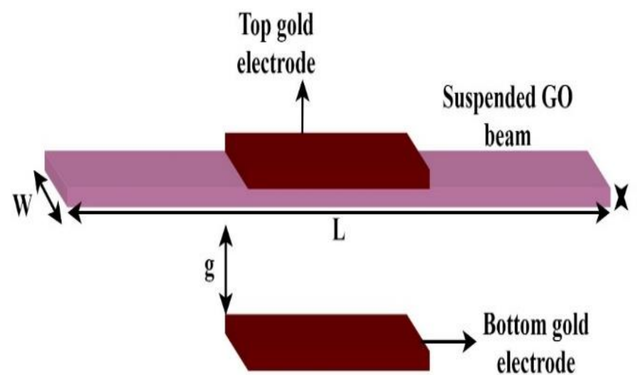

Figure 21:GO/gold NEMS switch

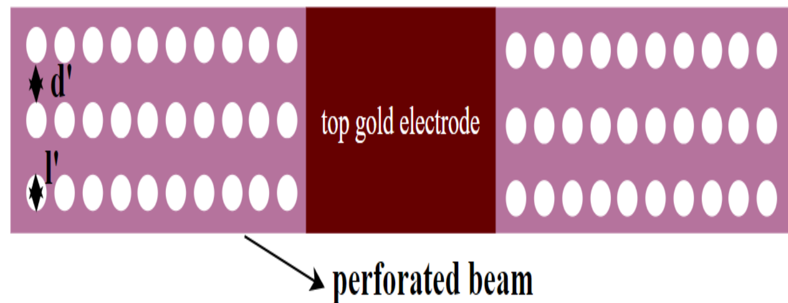

Figure 22: GO/gold double clamped beam

Table 5: GO beam and electrode dimensions

Beam Parameters	Values
Length (L)	2 µm
Width (W)	0.3 µm
Thickness (t)	4.9 nm
Gap (g)	50 nm
Top electrode width	0.3 µm
Top electrode length	0.4 µm
Top electrode thickness	3 nm

Table 6: Circularly perforated beam dimensions

Perforations parameters	Values
Hole diameter (l')	50 nm
Gap between two holes (d')	50 nm

In NEMS switches, low actuation voltage is desired. The actuation voltage can be decreased by either changing spring stiffness of suspended beam, by changing the device dimensions, by using perforations, or by using meander structure. By making perforations in the beam, the mass of the beam reduces and the air below the suspended beam gets easily squeeze out. Thus, it reduces the actuation voltage. In the perforated structure, the change in actuation voltage is highly dependent on the size/shape of perforations [148].

3.4 Results and Discussions

FEA of a shunt capacitive switch has been performed. The pull-in voltage analysis is performed for both intact structure and circularly perforated structure. The pull-in voltage of 5.6 V is obtained for the intact structure of GO-based NEMS switch. Figure 23 (a) shows the total displacement of 50 nm achieved at voltage 5.6 V. The actuation voltage of 4.75 V is obtained for the circularly perforated structure. Figure 23 (b) shows the total displacement of 50 nm at voltage 4.75 V.

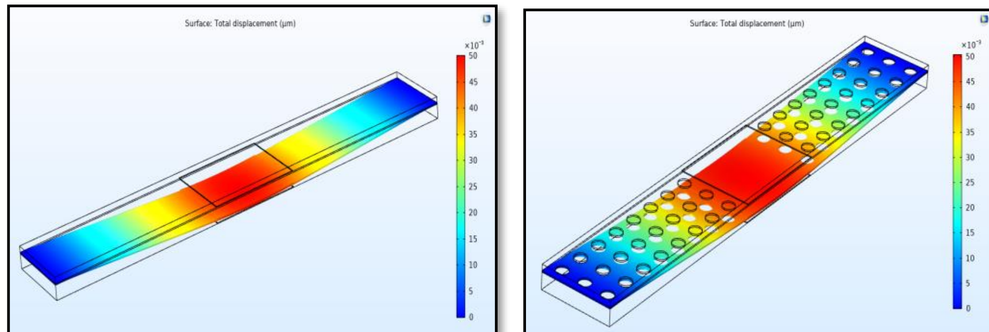

Figure 23: (a) Intact GO beam in downstate (b) Circularly perforated beam in downstate

The actuation voltage depends upon the spring stiffness of suspended beam. The spring stiffness of the suspended beam gets changed by making perforations in the beam. By making perforations, the mass of the beam reduces and the beam becomes less stiff. While other parameters are same for both cases but the spring stiffness for both intact and perforated beam is different. Hence, different voltage values are obtained.

Figure 24 shows the gap vs applied voltage plot for both structures. When the applied voltage is 0 V, the suspended beam remains in upstate. As the applied voltage increases, the gap between the actuating electrode and suspended beam decreases.

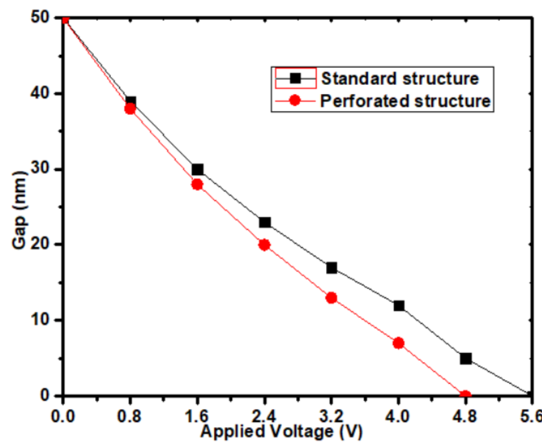

Figure 24: Gap vs applied voltage plot

When the applied voltage is equal to pull-in voltage, the beam touches the actuating electrode and the gap becomes zero. The results show that the pull-in voltage can be reduced from 5.6 V to 4.75 V by making circular perforations in suspended beam.

Eigenfrequency analysis has performed for both intact and circularly perforated GO-based NEMS switch structures. The obtained first six eigenfrequency modes are given in table 7.

Table 7: Obtained eigenfrequencies

Mode	Eigenfrequency Value (Hz) Standard structure	Eigenfrequency Value (Hz) Circular Perforated structure
1	3.80 E6	3.21 E6
2	1.90 E7	1.63 E7
3	2.11 E7	1.80 E7
4	6.51 E7	6.20 E7
5	8.01 E7	7.25 E7
6	1.25 E8	1.23 E8

The basic modes of oscillation of the device are represented by eigenfrequency analysis. In the analysis, different eigenmodes can be obtained. The primary eigenmode represents the desired motion of the device while the higher eigenmodes represent the undesired modes. For both intact and circularly perforated structures, six different eigenfrequency modes are obtained using FEA as shown in figures 25, 26.

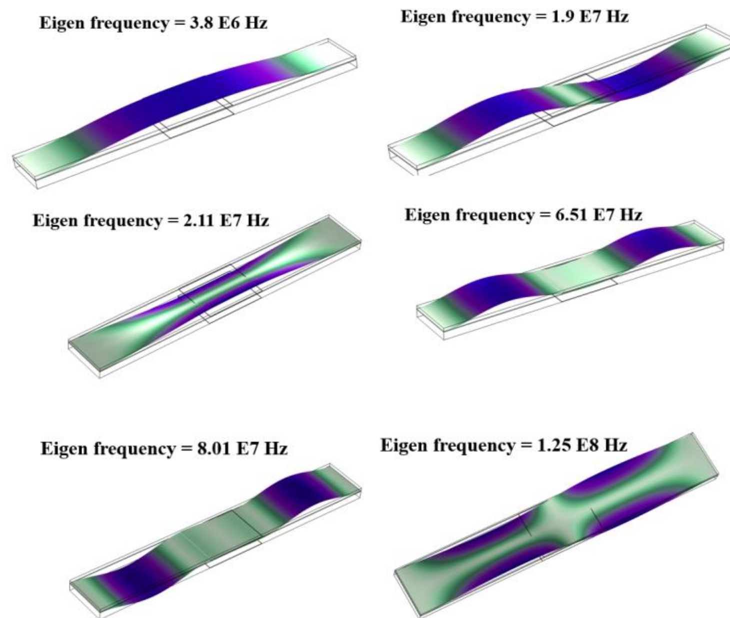

Figure 25: First six eigenmodes of intact structure

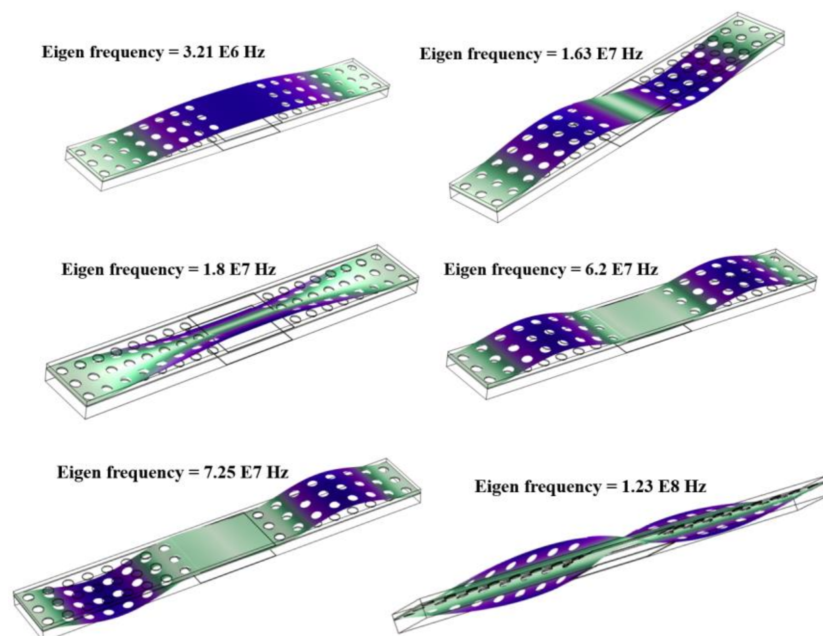

Figure 26: First six eigenmodes of perforated beam

For intact GO NEMS switch structure, the obtained values of eigenfrequencies are 3.8 MHz, 19 MHz, 21.1 MHz, 65.1 MHz, 80.1 MHz, 125 MHz. For circularly perforated structure, the obtained values of eigenfrequencies are 3.21 MHz, 16.3 MHz, 18 MHz, 62 MHz, 72.5 MHz, 123 MHz. The primary eigenmodes in both cases are 3.8 MHz and 3.21 MHz for intact and circularly perforated structure respectively. For the circularly perforated structures, the eigenfrequency values are less as compared to intact structure. By making a circularly perforated structure, the flexural rigidity of the suspended beam is reduced which reduces the inertia of the beam. The reduction in inertia further reduces the eigenfrequency.

3.5 Summary

- In the first section, the pull-in response and mechanical reliability of GO-based NEMS switch were investigated for the first time by taking GO along with graphene beam. Based on 3D modelling of both standard and perforated GO NEMS switches, the perforated beam structure is preferred over standard beam structure as it requires low pull-in voltage.
- The simulated von Mises stress values for GO NEMS switch and graphene NEMS switch are 500 MPa and 4.8 GPa respectively. This lesser value of von Mises stress in GO NEMS switch makes it a good choice as beam material.
- The variation in capacitance was successfully demonstrated when the suspended beam actuated towards the bottom graphene electrode. The maximum value of capacitance obtained was 0.9403 pF when the GO beam was in contact with the bottom electrode.
- In the second section, pull-in stability and eigenfrequency analysis of gold/GO based NEMS switch have performed. The FEM of gold/GO-based intact and circularly perforated structures are done using COMSOL Multiphysics.
- The circularly perforated structure gets actuated at a voltage less than the intact structure. By making perforations, the air below the suspended beam is easily squeezed out through the perforations, hence reduces the actuation voltage.
- Eigenfrequency analysis for both the structures is performed to find out the primary eigen mode. It is observed that by making perforations, the pull-in voltage and eigen frequencies are reduced. The pull-in voltage can be further reduced by changing the perforation size/shape.

Chapter 4

RF ANALYSIS OF G/GO BASED NEMS SWITCH

Since, the design and analysis of GO NEMS switch has successfully carried out in the previous chapter, in this chapter, analysis of the RF performance of GO NEMS switch has been performed. Both monolayer and multilayer GO suspended beam were designed (section 4.3) and analyzed using FEM and the RF performance analysis was performed using HFSS (section 4.4).

4.1 RF NEMS switch

RF performance analysis of GO-based double clamped shunt capacitive switch has been reported. The NEMS switch structure consists of GO along with graphene as a suspended beam that has been reported earlier. The performance analysis at a high frequency of GO NEMS switch has been achieved using Ansys high-frequency structure simulator (HFSS). The analysis of both monolayer and multilayer GO NEMS switch structures has been performed. FEM based tool COMSOL Multiphysics has been used to evaluate the pull-in voltage and to analyze the first three mode shapes in eigenfrequency analysis.

4.2 Design parameters

The 3D schematic diagram of the proposed GO-based RF NEMS shunt capacitive switch is given in figure 27. The RF NEMS switch structure is implemented on a CPW line and it comprises a dielectric layer along with a conductive electrode on the top of it. GO along with the graphene electrode is taken as a suspended beam. The suspended beam is situated at the height of 30 nm from the bottom actuating electrode.

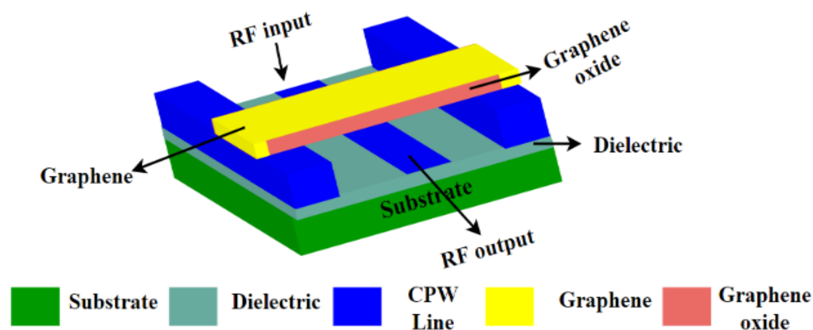

Figure 27: GO-based RF NEMS switch

The switch structure having graphene/GO suspended beam has been considered similar to that used in previous chapter. But, the length of the top electrode is changed in this chapter. In previous chapter, a small length of the top graphene electrode was considered. But to analyze the S-parameters, the top electrode should touch the ground lines of the CPW line. As the length of the top electrode is increased, it again changes the pull-in voltage. For accurate measurements, the length of the top electrode has changed, so that in the off state, the signal should get grounded properly. The geometric parameters of the proposed switch are given in table 8.

Table 8: Dimensions of proposed switch

Parameters	Symbol	Values
Beam length	L	1.1 µm
Beam width	W	0.3 µm
Beam thickness (Monolayer)	t_d	0.7 nm
Beam thickness (Multilayer)	t_d	2.8 nm
Air gap	g_o	30 nm
Electrode width	W	0.5 µm

In the analysis of RF performance of a NEMS switch, the insertion loss and isolation can be measured. The discontinuity between characteristic impedance of the RF line and switch results in insertion loss. The characteristic impedance (Z_o) of CPW line depends upon the width of central conductor (w), conductor spacing (S), permittivity of substrate (ε_r), and height of the substrate (H). For lossless transmission, the impedance of CPW line must be 50 Ω [21]. Figure 28 shows the top view of the RF NEMS switch suspended over the CPW line.

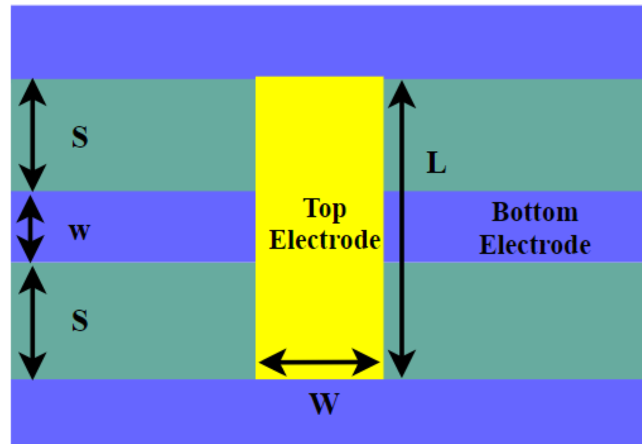

Figure 28: Top view of GO-based RF NEMS switch

4.3 FEA of GO-based NEMS switch

The analysis is carried out for both monolayer and multilayer GO beam. The pull-in voltage of 7.5 V and 9.8 V are obtained for the monolayer and multilayer GO NEMS switch respectively. Figure 29, 30 shows the total displacement of 30 nm is achieved at the pull-in voltage. As the beam thickness is increased, the pull-in voltage also gets increased. Monolayer GO-based NEMS switch requires less pull-in voltage than the multilayer GO.

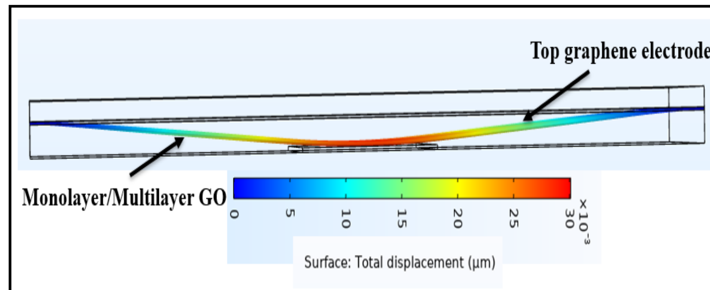

Figure 29: Side view of total displacement for 30 nm gap

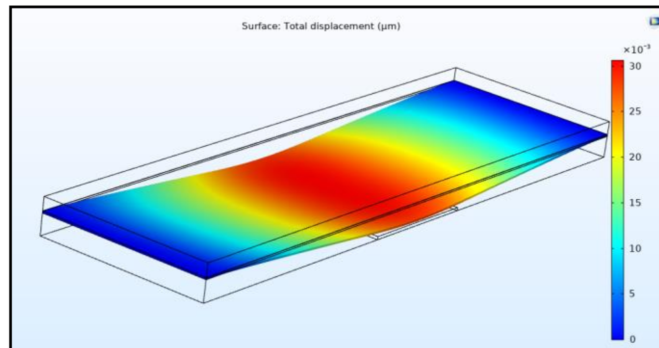

Figure 30: Pull-in analysis for 30 nm gap

The dimensions of the switch given in table 8, (S/w/S=0.3/0.5/0.3) results in Z_o of 50 Ω. If proper impedance matching between the RF line and NEMS switch is done, fewer losses occur during the signal transmission. The dimensions of the switch in this case are considered to minimize the losses and obtain accurate results.

4.4 Eigenfrequency Analysis and Actuation speed

The fundamental frequency of a device is known as eigenfrequency. The basic modes of vibration of RF NEMS switch are extracted by eigenfrequency analysis. COMSOL Multiphysics FEM simulation has been performed to extract the first three modes of eigenfrequency given in table 9. The monolayer resonates at less frequency than multilayer.

Table 9: Eigenfrequency analysis

Mode	Eigenfrequency (Hz)	
	Monolayer	**Multilayer**
Mode 1	2.31 E7	3.40 E7
Mode 2	6.30 E7	9.39 E7
Mode 3	6.39 E7	1.13 E8

For GO capacitive shunt switch, the three eigenfrequency modes are shown in figure 31.

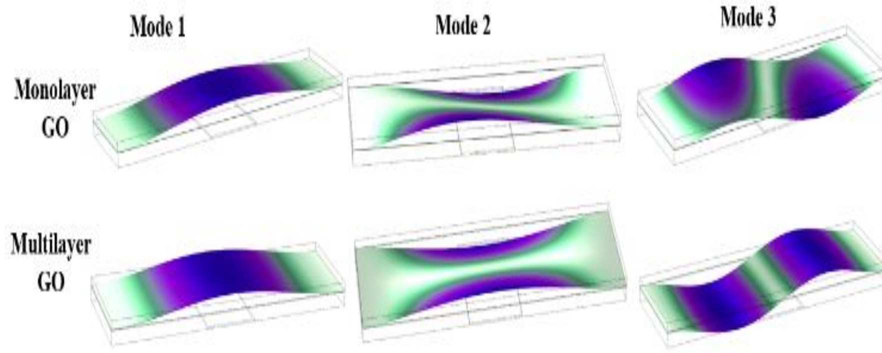

Figure 31: First three eigenfrequency modes mono/multilayer GO NEMS switch

The switching time of 19.4 ns and 13.2 ns are obtained for monolayer and multilayer GO NEMS switch respectively. Both monolayer and multilayer switch structures result in high switching time.

The downstate capacitance is simulated when the switch is in off state and the beam completely touches the bottom electrode. The obtained downstate capacitance ($\frac{\varepsilon_o \varepsilon_r}{t_d}$) for the monolayer GO beam is 7.5 pF and the multilayer GO beam is 1.89 pF. As the dielectric thickness is decreased, the downstate capacitance increases.

4.5 S-parameters

S-parameter analysis of GO NEMS switch structure has been achieved at frequency range 1-60 GHz to study the RF performance of the designed switch. For upstate, insertion loss, and for downstate, isolation has been calculated for both monolayer and multilayer GO NEMS switch. The obtained s-parameters results for both upstate and downstate are shown in figure 32. For monolayer, the insertion loss of 0.03 to 0.06 dB, and isolation of > 70 dB has been obtained for the frequency range of 1-60 GHz. For multilayer, the obtained insertion loss of 0.03 dB to 0.05 dB, and isolation of > 60 dB has been obtained for the frequency range of 1-60 GHz.

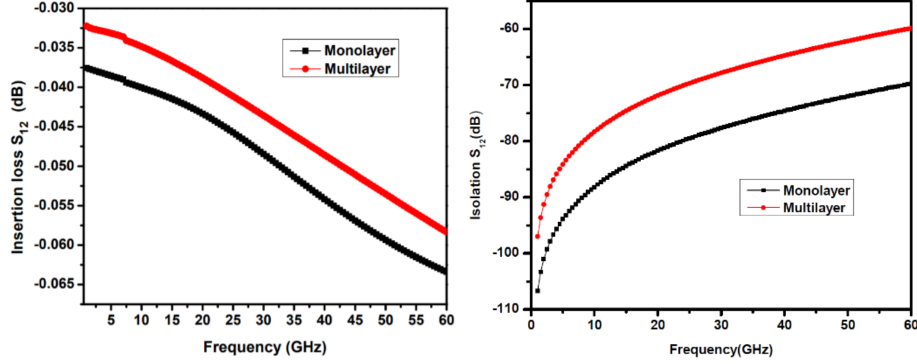

Figure 32: Obtained (a) Insertion loss (b) Isolation of GO NEMS switch

The isolation of NEMS switch depends upon the downstate capacitance. To achieve high isolation, the downstate capacitance should be high. In the above case, monolayer switch exhibits high downstate capacitance. Thus, the isolation of monolayer switch is higher than multilayer switch.

The insertion loss depends upon the upstate capacitance. For the switch to exhibit low insertion loss, the upstate capacitance should be small. The multilayer switch has less upstate capacitance than monolayer switch. Thus, the multilayer switch exhibits less insertion loss. The monolayer switch provides high isolation than multilayer while the small variation in insertion loss has been observed. Also, the calculated values of resistance for top graphene electrode are 3.05 Ω. The inductance of the suspended beam is determined by the resonant frequency. Both monolayer and multilayer NEMS switches resonate at different frequencies. Thus, the obtained inductance values are 6.33 μH and 11.6 μH for monolayer and multilayer respectively.

The obtained s-parameters of monolayer and multilayer beam are mentioned in table 10. Based on results, it is evident that GO can be used as a suspended beam as GO RF NEMS switch provides very good isolation and low insertion loss.

Table 10: RF performance of simulated switch

Beam type	Bridge/Dielectric	Isolation	Insertion loss
Monolayer	Graphene-GO/GO	>70 dB	0.03 -0.06 dB @1-60 GHz
Multilayer	Graphene-GO/GO	>60 dB	0.03-0.05 dB @1-60 GHz

4.6 Summary

- In the chapter, RF performance analysis for GO NEMS shunt switch has been evaluated for the first time. The S-parameter of monolayer and multilayer GO-based switches are analyzed for the frequency range of 1-60 GHz.

- The simulated monolayer GO NEMS switch acquires low pull-in voltage and exhibits high downstate capacitance. Both the simulated switch structures provide high switching speed and good RF performance.
- The different eigenmodes of the suspended graphene-GO beam are obtained by performing the FEM of the proposed switch. GO-based NEMS switch can be preferred in the application that requires good RF performance, less pull-in voltage and high switching speed.

Chapter 5

NEMS SWITCH WITH DIFFERENT BRIDGE STRUCTURES

In the previous chapters, analysis of only intact and perforated beam has been done. This chapter deals with design and analysis of graphene NEMS switch having different bridge structures. The analysis of different bridge structure has been carried out to find a bridge structure that actuated at minimum pull-in voltage. The analysis of actuation voltage (section 5.2) and total capacitance (section 5.2) for various structures has been performed. The results show that different bridges have different spring stiffness and get actuated at different actuation voltages.

5.1 Different bridge structures

NEMS switch consists of a metal bridge structure suspended at some height over the transmission line. The central conductor at which bias voltage is applied is known as the actuation electrode and is covered with a dielectric material. The on-off switching of the NEMS switch is achieved by electrostatic actuation. The signal passes through the central electrode of the transmission line. The potential difference is applied between the actuation electrode and the graphene beam. This structure in which the suspended beam is placed perpendicularly to the signal line (covered with the dielectric) is known as a shunt capacitive switch. In this work, graphene has been chosen as suspended beam material. The Young's modulus of graphene is taken as 860 GPa and the Poisson's ratio is set as 0.17 [159].

Figure 33 shows the side view of the graphene NEMS switch. For the actuation electrode, gold metal is taken and for dielectric material, 25 nm thick HfO_2 (ε_r=25) is taken [21]. The device dimensions for this switch structure are mentioned in table 11.

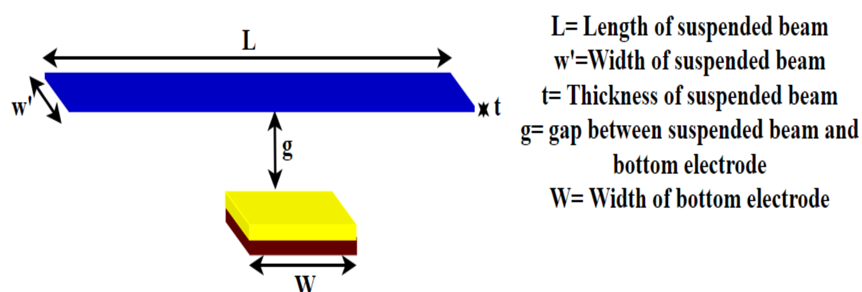

Figure 33: NEMS switch with intact beam structure

Table 11: NEMS switch device dimensions

Design parameters	Values
Beam Width (w_b)	5 µm
Thickness (t_b)	9 nm
Length (L)	10 µm
Gap (g)	250 nm
Electrode area	2 µm *5 µm

As shown in figure 34, the study of five different structures referred to as structures a, b, c, d, e respectively is done. The different bridge structures get actuated at a different voltage.

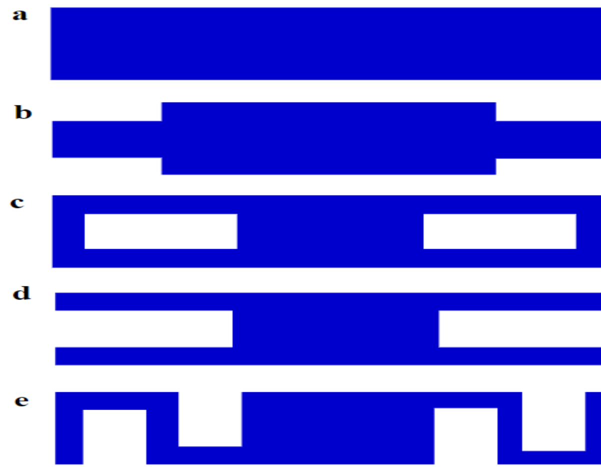

Figure 34: Different graphene bridge structures

FEM of five different bridge structures has been performed. All the simulations are performed in the air medium. The bias voltage is applied at the bottom actuation electrode while the suspended graphene beam is kept at ground potential.

5.2 Results and discussion

The structural design and analysis of the NEMS switch have been performed in COMSOL Multiphysics. Five different bridge structures are designed and simulated. Since bridge structure is considered, both the ends of the bridge are fixed. Graphene beam of 10 µm length, 5 µm width, and 9 nm thick is considered as a suspended beam. The beam is suspended at a height of 250 nm from the dielectric material. The actuation voltage is applied at the bottom electrode. All the bridges structures get actuated at different actuation voltage. The total displacement of 250 nm of different graphene bridge structures is shown in figure 35 (a-e).

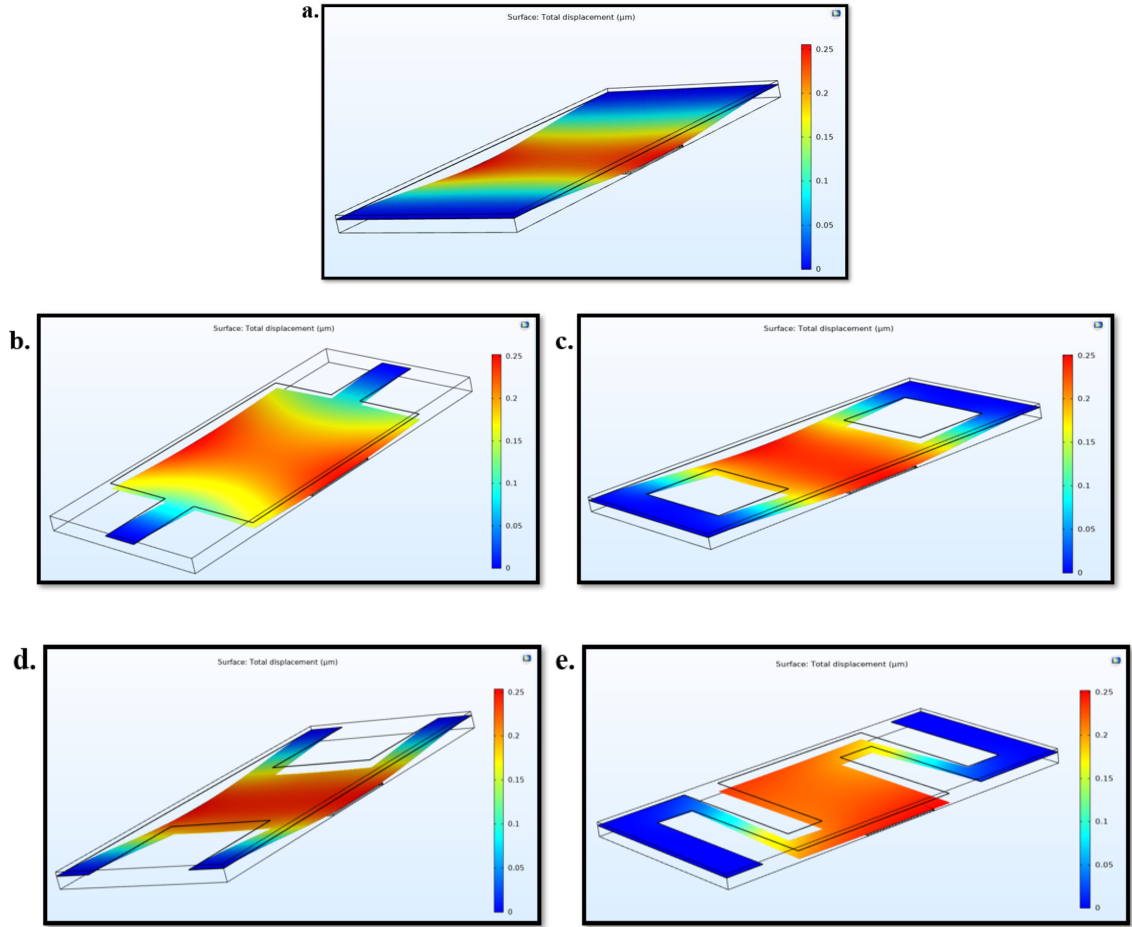

Figure 35: Total displacement of different structures (a) structure-1 (b) structure-2 (c) structure-3 (d) structure-4 (e) structure-5

The results show that different voltages are required to snap down the bridge in different structures. As the bridge structures are different in all five cases, the spring constant of the bridge also changes, which in turn changes the actuation voltage. Table 12 summarises the pull-in voltage obtained for different bridge structures.

Table 12: Pull-in voltage for different bridge structures

Bridge Structure	Pull-in Voltage
1	4.43 V
2	2.8 V
3	3.65 V
4	3.38 V
5	1.41 V

When NEMS switch is actuated between on-off states, two types of capacitance exists, one is upstate capacitance ($C_{up}= \frac{\varepsilon_o w_b W}{g+\frac{t_d}{\varepsilon_r}}$) other is downstate capacitance ($C_d=\frac{\varepsilon_o w_b W}{g}$). The downstate capacitance is further divided into two parts: one is parallel

plate capacitance (C_p) while the other is tilted plate capacitance (C_t). For accurate results, all three capacitances should be calculated. In the downstate, the beam forms contact with the dielectric layer as shown in figure 36. The total capacitance can be written as equation 16:

$$C_{Total} = C_{up} + C_d \quad (16)$$

Here, $C_d = C_p + 2C_t$

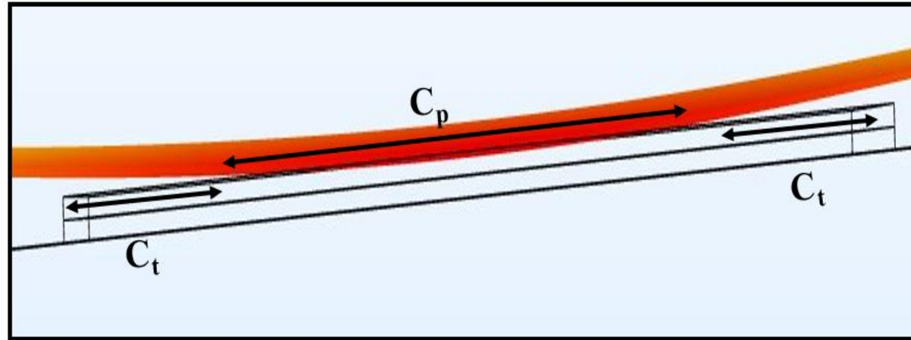

Figure 36: Downstate capacitances

For the simulated NEMS switch, the obtained upstate, parallel plate, and tilted plate capacitances are 0.3 fF, 0.66 pF, and 0.85 fF respectively. The area of the graphene beam that is in contact with the dielectric material is the same for all the cases. Hence the same value of capacitance is obtained in all the cases.

5.3 Summary

- Graphene-based NEMS switch with different bridge structures has been designed and simulated in COMSOL Multiphysics. For different bridge structures, different actuation voltages are obtained. The intact structure requires the maximum actuation voltage (4.43 V) while the structure-5 requires a minimum actuation voltage (1.41 V).
- The actuation voltage depends upon the bridge stiffness. The different bridge structures have different spring stiffness. The perforations reduce the mass of the suspended beam and make beam less stiff which in turn changes the actuation voltage. Also, the total capacitance of 0.66 pF has been obtained for the simulated switch structure.

Chapter 6

OPTIMIZATION OF DESIGN PARAMETERS OF GO NEMS SWITCH

In the previous chapter, the results illustrate that hinge structure requires the least actuation voltage. This chapter focuses on the design and simulation of a hinge structure-based GO NEMS shunt switch. The optimization of different device parameters such as beam length, beam thickness, and air gap has been performed to achieve low pull-in voltage (section 6.3). Also, von Mises stress analysis (section 6.4), eigenfrequency analysis (section 6.5) of the given switch structure has been performed. The RF performance (section 6.6) of the simulated switch with the least pull-in voltage has been carried out using Ansys high-frequency structure simulator.

6.1 Geometrical description of NEMS switch

This section describes the design and modelling of hinge structure-based GO NEMS switch. The designed NEMS switch resides in an air-box in which the bottom actuation electrode is located at the lower side of the air-box while the hinge structure-based GO beam is suspended at some height. On top of the GO beam, a gold electrode is situated. The ends of the suspended GO hinge structure are fixed. The actuating voltage is applied at the bottom electrode while the top electrode is grounded.

The FEM of GO-based NEMS switch is simulated in the air medium. The length of the suspended beam is varied from 1 μm to 1.6 μm, the thickness of the beam is varied from 2.8 nm to 4.9 nm, and the air gap is changed from 30 to 60 nm. The effect of intermolecular forces is neglected in simulations as the effects of the forces cannot be encountered for the air gap >30 nm [150]. The schematic diagram and top view of the hinge structure-based GO beam are shown in figure 37 and the dimensions are given in table 13.

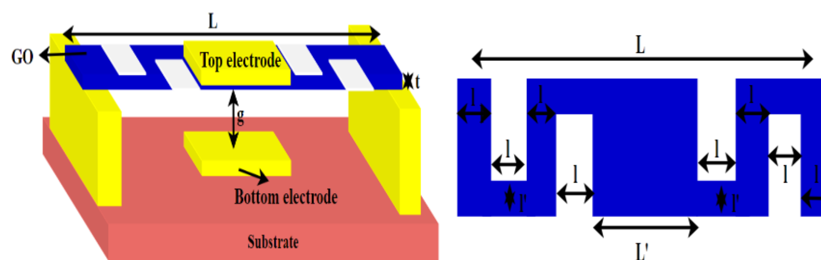

Figure 37: GO-based NEMS shunt switch (a). Schematic diagram (b). Top view

Table 13: Suspended GO beam dimensions

Parameters	Values
Total length (L)	1 µm
L’	200 nm
L	100 nm
l’	50 nm
Beam length (L)	1-1.6 µm
Beam thickness (t)	2.8-4.9 nm
Air gap (g)	30-60 nm
Beam width	0.2 µm

6.2 Effect of different parameters

The change in device dimensions affects the switch performance, especially in terms of the pull-in voltage. The applied voltage at which the beam touches the bottom electrode is known as pull-in voltage. The pull-in voltage can be varied by varying three key parameters explained below:

6.2.1 Suspended beam length: In NEMS switch, the performance of the NEMS switch is profoundly affected by varying the beam length. From equations 10 and 11, it is clear that the change in beam length affects the beam stiffness. Increase in the beam length makes the beam less stiff, and therefore it can easily be deflected. This in turn reduces the actuation voltage. If the length of the suspended beam is decreased, the beam becomes stiffer, less flexible, and large pull-in voltage is required to deflect the beam. However, the length of the double clamped beam cannot be scaled down severely as it has high internal strain as compared to a cantilever beam [160].

6.2.2 Suspended beam thickness: The stiffness of the suspended beam can also be reduced by reducing the beam thickness. As the beam thickness is reduced, spring constant gets reduced which further causes the reduction in the pull-in voltage. The reduction in thickness of the beam also affects the switching speed. The effective mass of the beam gets reduced by decreasing the beam thickness, which further changes the switching speed.

6.2.3 Air gap: The change in pull-in voltage is highly affected by changing the air gap between the suspended beam and bottom actuation electrode. When the air gap is reduced, the pull-in voltage gets reduced, and when the gap is increased, the pull-in voltage gets increased. But the air gap cannot be decreased beyond

some critical dimensions. If the air gap is taken below 30 nm, the effect of intermolecular forces needs to be considered.

6.3 Results and Discussion

The FEM for GO based NEMS shunt switch is performed using COMSOL Multiphysics. As shown in figure 38, the NEMS switch switches between two states: off state and on state. The operation of the double clamped beam switch has already been discussed in section 1.4.

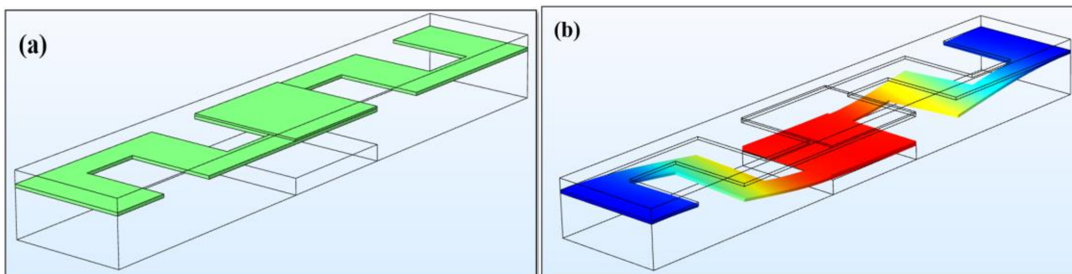

Figure 38: Simulated GO-based NEMS shunt capacitive switch during (a) On state (b) Off state

For the parameters given in table 16, the different value of pull-in voltage is achieved by varying the beam length from 1 µm to 1.6 µm. The voltage is applied at the bottom actuation electrode and the top electrode remains at ground potential. The applied voltage generates electrostatic force, and the beam gets deflected towards the actuating electrode. For the beam length of 1µm, an actuation voltage of 4.2 V is achieved. As the beam length is increased, the pull-in voltage reduces from 4.2 V to 2.1 V. The increase in length makes the beam more flexible, less stiff, and it can be easily deflected. Thus, the reduction in the pull-in voltage is observed as the beam length is increased. Figure 39 (a) demonstrates the behavior of actuation voltage on changing the beam length.

On changing the beam thickness from 2.8 nm to 4.9 nm, the variation in pull-in voltage from 2.7 V to 4.2 V has been observed. When the beam thickness is increased, the pull-in voltage increases. The thinner beam can be easily deflected. Figure 39 (b) shows the effect of variation of beam thickness on pull-in voltage.

Increasing the air gap among the suspended GO beam and bottom electrode also increases the actuation voltage. Figure 39 (c) shows the variation in pull-in voltage from 1.5 V to 6.2 V, by varying the air gap from 30 nm to 60 nm. The results show that a long and thin beam becomes less stiff, more flexible hence requires less pull-in voltage.

While the increase in the air gap requires more electrostatic forces to deflect the beam, therefore, increases the pull-in voltage.

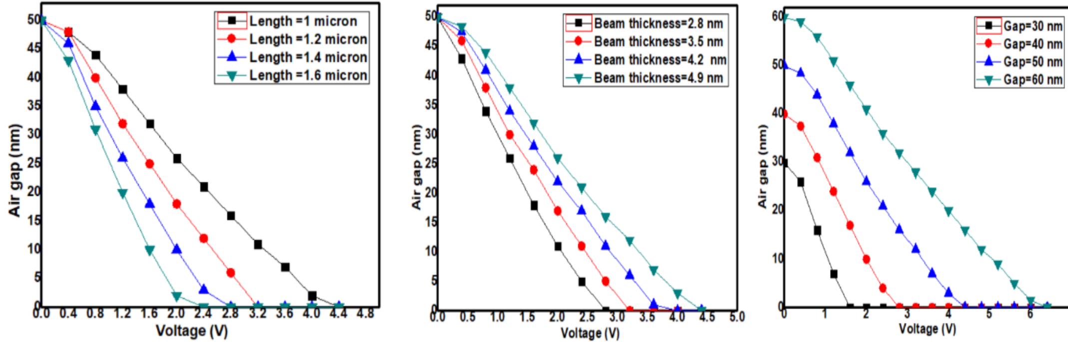

Figure 39: Variation in pull-in voltage by varying (a) GO length (b) GO thickness (c) Air gap

On increasing the beam length from 1 µm to 1.6 µm, the pull-in voltage gets reduced to approximately 50%. While increasing the beam thickness from 2.8 nm to 4.9 nm and the air gap from 30 nm to 60 nm, the pull-in voltage gets increased by 313 % and 320 %, respectively. The simulated and analyzed outcomes have been outlined in table 14 and the results have plotted again in figure 40.

Table 14: Dimensions of GO-based switch by varying different design parameters

Switch configuration	Varying parameter	Length (µm)	Thickness (nm)	Air gap (nm)	Pull-in voltage (V)
A		1			4.2
B		1.2	4.9	50	3.2
C	Length	1.4			2.6
D		1.6			2.1
E				30	1.5
F	Air gap	1	4.9	40	2.7
G				50	4.2
H				60	6.2
I			2.8		2.7
J	Thickness	1	3.5	50	3.2
K			4.2		3.7
L			4.9		4.2

Figure 40 shows that there is a negative correlation between pull-in voltage and beam length while the other two parameters: the thickness of the GO beam and the air gap is in positive correlation with pull-in voltage. If the beam length increases, the pull-in voltage decreases. But if the thickness of the GO and air gap is increased, the pull-in

voltage also increases. The minimum pull-in voltage of 1.5 V has achieved for the beam length of 1 μm, beam thickness of 4.9 nm, and air gap of 30 nm. The results show that thin, long, and small air gap beam can be preferred as it requires low pull-in voltage.

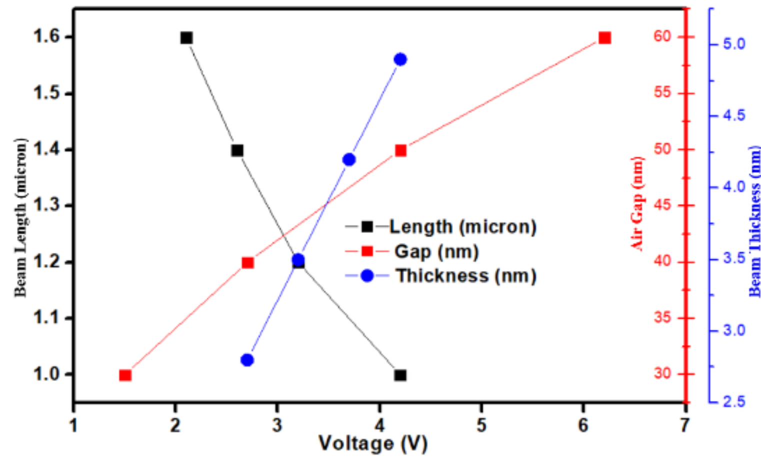

Figure 40: Pull-in voltage trends against different design parameters of the NEMS switch

6.4 von Mises stress analysis

By optimizing the switch dimensions, the mechanical stability of the GO-based NEMS switch can be improved. The FEM modelling of the switch is carried out to observe the effect of change in length, thickness, and air gap on von Mises stress. Figure 41 shows the contour plot analysis from the top view of the NEMS switch (L=1 μm, t= 4.9 nm, g= 30 nm). The analysis for the length variation from 1-1.6 μm, thickness variation from 2.8-4.9 nm, and air gap variation from 30-60 nm has been performed in COMSOL Multiphysics. The simulated results of GO-based NEMS shunt switch are given in table 15.

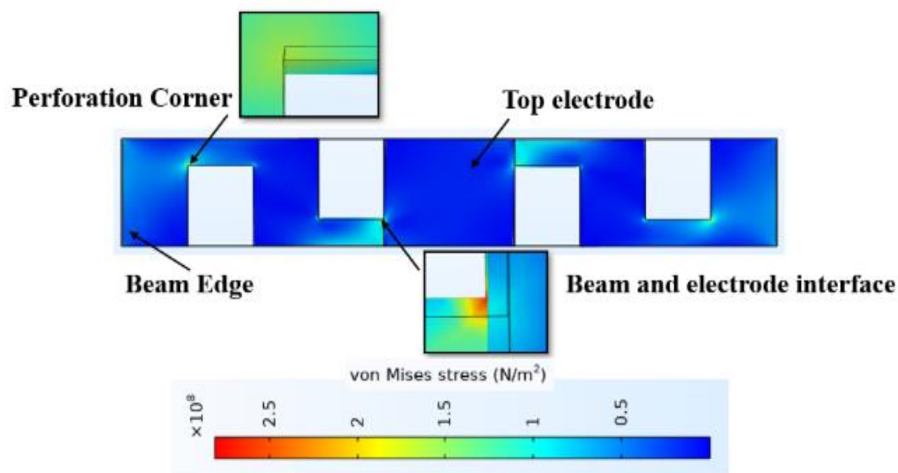

Figure 41: Von Mises contour plot

Table 15: von Mises stress analysis results for different design parameters

Design parameters		Beam edge	Perforation corner	Beam and electrode interface	Top electrode
		von Mises Stress (MPa)			
Beam Length	**1µm**	85.8	465	567	47.9
	1.2 µm	67.8	329	415	31.2
	1.4 µm	48.7	232	362	21.1
	1.6 µm	35.3	156	264	11.3
Beam Thickness	**2.8 nm**	49.5	360	551	19
	3.5 nm	55.5	438	585	25.1
	4.2 nm	73	495	608	42.4
	4.9 nm	89.9	501	708	53.5
Air Gap	**30 nm**	42.5	275	369	27.3
	40 nm	74.7	366	459	33.8
	50 nm	85.8	463	647	53.4
	60 nm	123	607	875	74.2

On varying the beam length, the suspended GO beam with a length of 1 µm can withstand maximum von Mises stress (567 MPa) while the GO beam with a length of 1.6 µm can withstand minimum von Mises stress (264 MPa) at the beam-electrode interface. A variation in the von Mises stress has been observed with the variation in the beam design parameters.

The results illustrate that von Mises stress decreases by increasing the suspended GO length, reducing the GO thickness and air gap. The perforation corner and beam-electrode interface point suffer maximum stress because of the edge termination effect. In the edge termination effect, the electric field is high and concentrated at the sharp edges. Based on the obtained results, it can be concluded that thinner and longer beams can be preferred because of the minimum probability of device failure.

The cross-sectional view of the electric field distribution for the beam L=1 µm, t = 4.9 nm, and g = 30 nm in the off state is shown in figure 42. The pull-in voltage of 1.5 V is obtained for the given switch structure. At the bottom electrode, the voltage is applied. So, the electric field is highly dense at the bottom electrode (red shade) while the top electrode is grounded, the electric field is less dense (blue shade). The electric field lines are directing towards the top electrode from the bottom electrode.

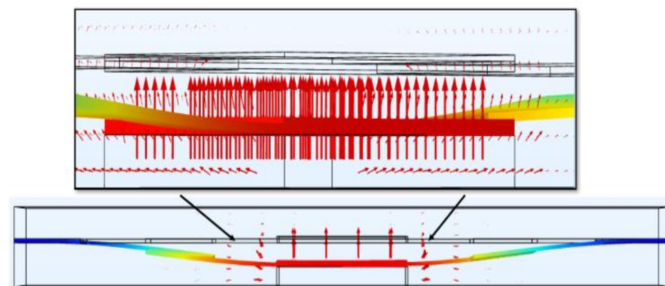

Figure 42: Side view of electric field distribution

6.5 Eigenfrequency Analysis

For GO capacitive shunt switch, the six eigenfrequency modes are shown in figure 43. The switching speed of the NEMS switch of 0.32 µs (L=1 µm, t = 4.9 nm, and g = 30 nm) is obtained by simulation.

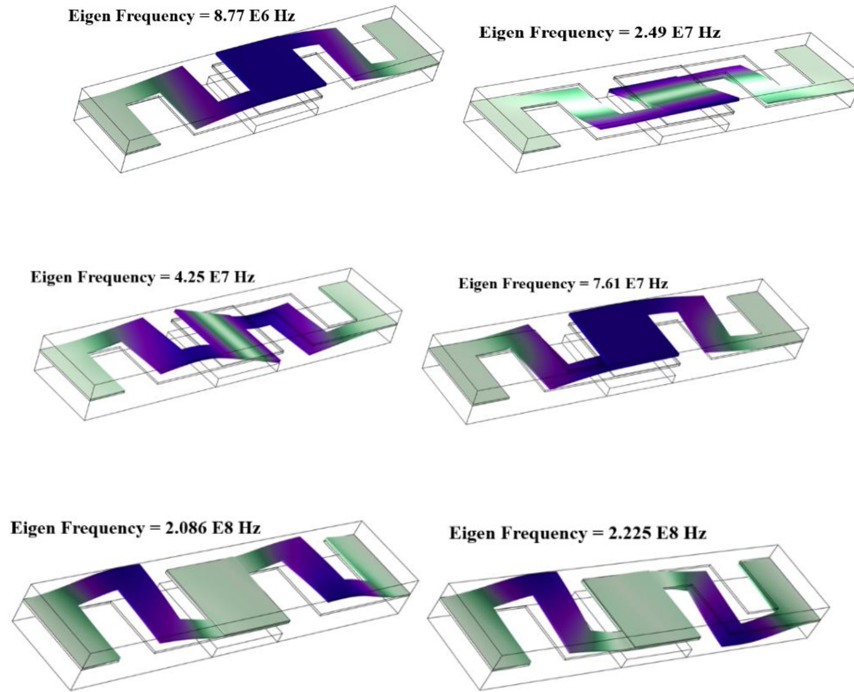

Figure 43: First six eigenfrequency modes GO NEMS switch

6.6 RF Performance analysis

After computing the actuation voltage, analyzing the von Mises stress and eigenfrequencies, RF performance of the NEMS switch is the most crucial parameter to analyze. S-parameter analysis is necessary to optimize the behavior of a NEMS switch in terms of isolation, insertion loss at high frequency.

S-parameter analysis of hinge based NEMS switch structure has been performed by using Ansys high-frequency structure simulation software. The RF performance of the switch is observed for the frequency range 1-60 GHz. For S-parameters analysis, the top electrode should touch the ground lines of the transmission line. The length of the top electrode is taken the same as that of the suspended beam which slightly increases the pull-in voltage. The insertion loss and isolation have been calculated for the upstate and downstate, respectively. Since the minimum actuation voltage is achieved for switch structure 'e' (table 14), RF performance analysis has been performed for this

switch structure. Figure 44 (a) shows the obtained S-parameters for the upstate position. The insertion loss of 0.02-0.03 dB is obtained for the hinge structure-based NEMS switch. Figure 44 (b) shows the obtained S-parameters for the downstate position. The isolation of >70 dB has been achieved for the frequency range of 1-60 GHz. It is clear from the results that the simulated NEMS switch structure exhibits high isolation and low insertion loss.

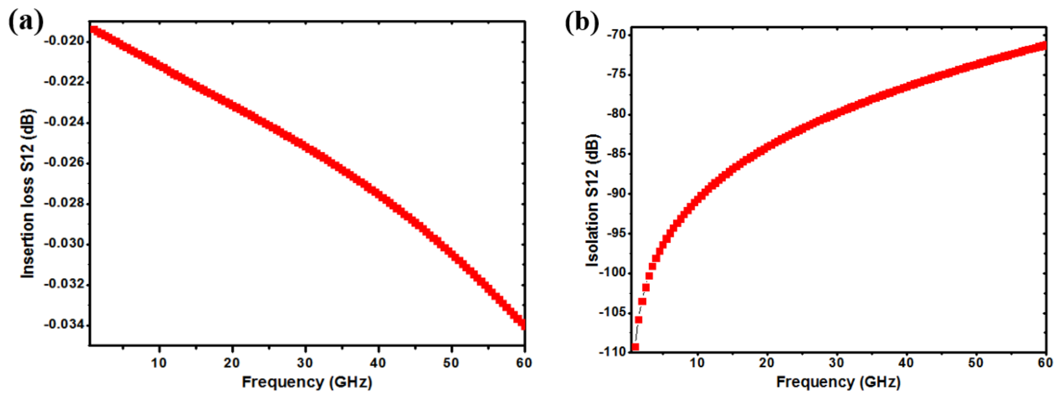

Figure 44: S-parameters analysis of GO NEMS switch (a). Insertion loss (b). Isolation

6.7 Summary

- FEM-based simulation is essential to study the electromechanical behavior and stress analysis of NEMS switch. The detailed analysis of variation in device design parameters such as length and thickness of the beam, and air gap on actuation voltage and von Mises stress is studied in this work.
- The pull-in voltage was reduced to 50% by increasing the beam length from 1 µm to 1.6 µm. Moreover, it also has been identified that the pull-in voltage has increased to 313% and 320% on changing the beam thickness from 2.8 nm to 4.9 nm and air gap from 30 nm to 60 nm, respectively.
- The von Mises can be reduced by increasing the length of GO, decreasing the thickness of GO, and the air gap between the GO and bottom electrode.
- The RF performance analysis of the proposed switch exhibited high isolation of >70 dB and insertion loss as low as 0.02-0.03 dB. It can be concluded that the long and thin GO beam requires less actuation voltage, which can endure less von Mises stress and exhibits good RF performance.

Chapter 7

GRAPHENE DERIVATIVES BASED COMPOSITE BEAM NEMS SWITCHES

This chapter deals with the comparison of performance parameters between the single material beam and composite beam based NEMS switches. For composite beam structures, graphene-RGO and graphene-GO are used to design and analyze the NEMS switches. Subsequently, the FEM of the single material beam (section 7.4) and the composite beam-based (section 7.5,7.6) switches have been performed to analyze the performance parameters like pull-in voltage, switching time, and restoring force.

7.1 Background

The performance of the MEMS switch is degraded by issues like high pull-in voltage, stiction, and poor mechanical stability. There are some methods to overcome high pull-in voltage problems: the first way is by reducing the air gap, the second one is by increasing the actuation area or another one is by reducing the spring constant of the fixed-fixed beam structure [44].

The spring constant of the material can be reduced either by changing the geometric design/using perforations/using meander structure [22][125][161] or by using new material with a low value of elastic modulus or modulus of elasticity [56]. For fixed-fixed beam and cantilever beam, low actuation pull-in voltage can be achieved without much reduction in restoring force.

The top graphene layer acts as an electrode that has been used with dielectric GO double clamped beam and at the bottom, another electrode has to be used to achieve the actuation mechanism. GO can be used along with a conductor like graphene to achieve the switching action of the NEMS switch. RGO is a graphene derivative that is formed by thermal or chemical reduction of GO. The purpose of reduction is to remove the oxygen groups and restore the conductivity. Thus, RGO possesses high charge carrier mobility and significant conductivity [80][162]. The double clamped beam of composite material can be modelled into a single material beam with a low effective elastic modulus. GO can be used along with the graphene beam to make a composite beam of low elastic modulus.

7.2 Selection of Suspended beam Material

The selection of appropriate material as a suspended beam depends upon material properties. Different materials have been used as suspended beam material for RF MEMS switch, but all of them have their pros and cons. Pure Au is highly inert to oxidation but pure Au contacts suffer contact pitting and hardening failure mechanisms [163]. Besides that, metals like tungsten and molybdenum are sensitive to oxidation [164]. In NEMS switches, graphene has drawn the attention because of characteristics like ultra-low thickness, high current conduction, and high elastic modulus [22]. But this very high elastic modulus increases the spring stiffness that further increases the pull-in voltage. A composite of graphene/GO can be considered to reduce the effective elastic modulus which in turn reduces the pull-in voltage. Pull-in voltage is one of the primary performance indices for the designing of RF M/NEMS switch. From equation 3 and 4, it is evident that pull-in voltage depends upon the spring constant, air gap, and electrostatic area. While, the spring constant further depends upon the design parameters, Poisson's ratio, and elastic modulus (E) of the fixed-fixed beam. Thus, the actuation voltage can be optimized by either changing the device dimensions or by choosing a material with a low elastic modulus.

7.3 Analysis of Single material double clamped beam

Ease of manufacturing and high spring stiffness are the two predominant reasons for using the double-clamped beam structure. The switching time can be lowered by taking a beam with high spring stiffness but at the expense of a high pull-in voltage. The double clamped beam offers high stability and is less sensitive to stress. The schematic diagram of RF NEMS switch with the graphene beam and graphene-GO composite bridge is shown in figure 45.

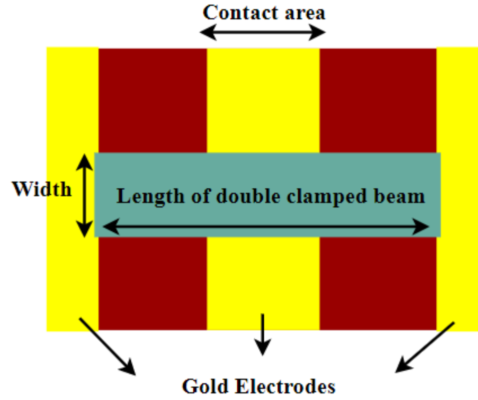

Figure 45: Top view of NEMS switch

7.4 FEA of proposed structure

In this study, the FEA of graphene NEMS switch was performed in COMSOL Multiphysics. Electromechanics and Solid mechanics modules are used for the electromechanical modelling of the designed switch. Graphene with an elastic modulus of 669 GPa and Poisson's ratio of 0.416 was considered for the simulation [165][166]. The actuation voltage of 12.2 V was achieved for the graphene beam of length 2 µm, width 0.3 µm, thickness 5 nm, and air gap of 40 nm as shown in figure 46.

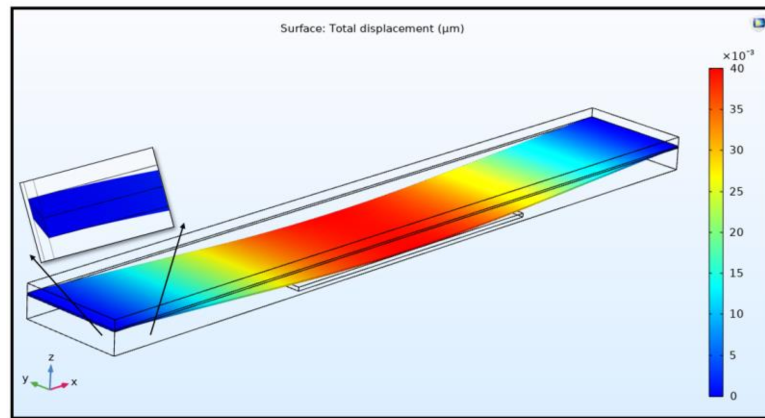

Figure 46: Simulated graphene NEMS switch

The driving force that is responsible for retrieving back the suspended beam into its initial position when the applied voltage is removed is known as restoring force. The restoring force f_R can be expressed by equation 17 [44]:

$$f_R = kg \tag{17}$$

k and g are the spring constant (N/m) and the air gap (µm) respectively.

Two different methods can be adopted to reduce the pull-in voltage. In method 1, the beam length of double clamped graphene beam can be varied and reduction in pull-

in voltage is observed. The simulation of graphene NEMS switch for different lengths has been performed in COMSOL Multiphysics. Table 16 shows the simulated results of pull-in voltages and restoring force for different lengths of suspended graphene beam.

Table 16: Variation in performance parameters of single material graphene beam

Beam length (µm)	Pull-in voltage (V)	Restoring force (nN)	Spring constant (N/m)
2	12.2	101	0.055
2.5	8.5	49.2	0.028
3	6.5	28.8	0.016
3.5	4.9	16.4	0.010
4	4	10.9	0.006

As the beam length of the suspended graphene beam is increased, the pull-in voltage, restoring force, and the spring constant of the beam are changed. The spring constant of the graphene beam was reduced to 0.016 N/m and the restoring force falls by 71 %, when the length of the graphene beam was changed from 2 µm to 3 µm, as shown in figure 47. Further increment in the beam length from 3 to 4 µm drops the spring constant to 0.006 N/m that pulls down the restoring force by 62 %. The spring constant and the restoring force were reduced to 0.006 N/m, 89% respectively as the length of the beam was doubled from 2 µm to 4 µm. The results show that changing the suspended beam geometry is not a good approach for lowering the pull-in voltage with nominal restoring force. From equation 22, it is evident that an increase in the length decreases the spring constant which in turn decreases the restoring force.

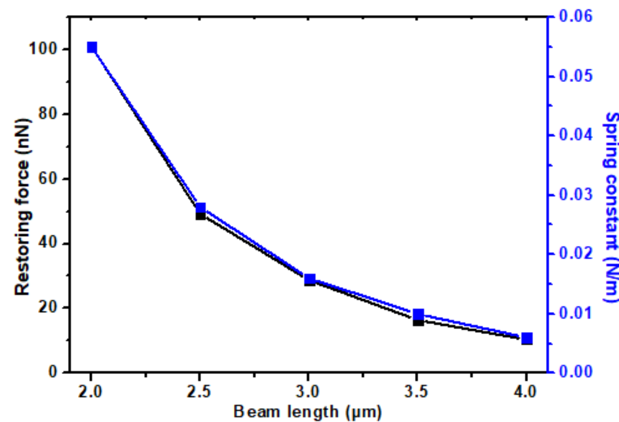

Figure 47: Effect of variation of beam length of Single material Graphene beam on Restoring force and Spring constant for different beam length

In method 2, the actuation voltage can be reduced by lowering the elastic modulus instead of changing the length of the beam. Table 17 shows the simulated results for a material beam of 2 μm length, 0.3 μm width, 5 nm thickness, and 40 nm gap for different spring constant values.

Table 17: Variation in performance parameters by changing the Elastic Modulus

Elastic Modulus (GPa)	Pull-in voltage (V)	Restoring force (nN)	Spring constant (N/m)
669	12.2	101	0.055
569	11.4	88.5	0.047
469	10.4	73.7	0.038
369	9.2	57.7	0.030
269	8	43.6	0.022

The elastic modulus value was changed from 669 GPa to 269 GPa. The simulated results are plotted in figure 48 (a), 48 (b), and 48 (c) show that as the elastic modulus of the material is reduced, the pull-in voltage gets reduced. It also reduces the restoring force.

In figure 48 (a), 48 (b), and 48 (c) two curves are plotted. The curve 1 indicates the results obtained for the change in beam lengths with elastic modulus 669 GPa. The curve 2 shows the results obtained for the change in the elastic modulus with 2 μm beam length.

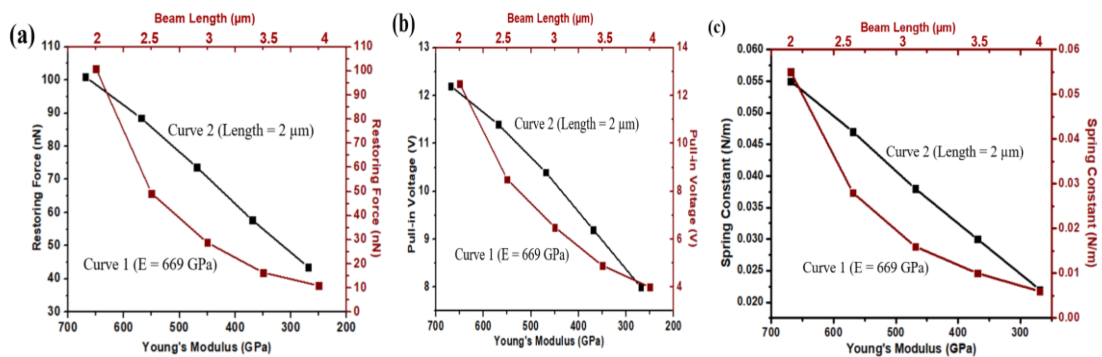

Figure 48: Comparison between the results obtained for (a) restoring force (b) pull-in voltage (c) spring constant using two different methods

The results indicate that the restoring force gets reduced by 56% (2.3 times), pull-in voltage gets reduced to 34% (1.5 times), and the spring constant reduced by 60% when the value of elastic modulus was varied. Figure 48 (a), 48 (b), and 48 (c) show the plot obtained for the change in restoring force, pull-in voltage, and spring constant for both

the cases first when beam length was changed and second when elastic modulus was changed. The results illustrate that by changing the beam length, abrupt change in the restoring force was obtained. The change in the beam length reduces the spring constant and reduction in spring constant rapidly changes the restoring force. On the other hand, the change in the restoring force is linear for the case when variation in elastic modulus value has been done.

The discussion presented here concludes that changing the device dimensions (beam length) cannot be a good approach as a sudden change in the restoring force is observed. The elastic modulus cannot be changed as elastic modulus is a property of the material that remains constant. So, another alternative is to use a beam of new material with less value of elastic modulus or use a composite beam.

7.5 Analysis of Graphene/RGO Composite beam

When two or more than two layers of different material with different elastic modulus and thickness are deposited over one another, a composite layer is formed. The concept of a composite beam is adopted to decrease the actuation voltage without much drop in restoring force. A new beam of single material can be formed as composite beam with an effective elastic modulus value. The design parameters like length, width, and gap of the beam are kept the same as that of single material double clamped beam. The single material graphene beam (5 nm thick) is replaced by graphene/RGO composite beam (2.2 nm/2.8 nm). The graphene/RGO beam of length 2 μm, width 0.3 μm, and air gap of 40 nm was considered for the pull-in analysis. A 2.2 nm thick graphene beam is placed over 2.8 nm thick RGO beam. RGO beam with elastic modulus of 207 GPa and Poisson's ratio of 0.19 was considered for the simulation [79]. Figure 49 shows the schematic diagram of the single material beam and composite double clamped beam.

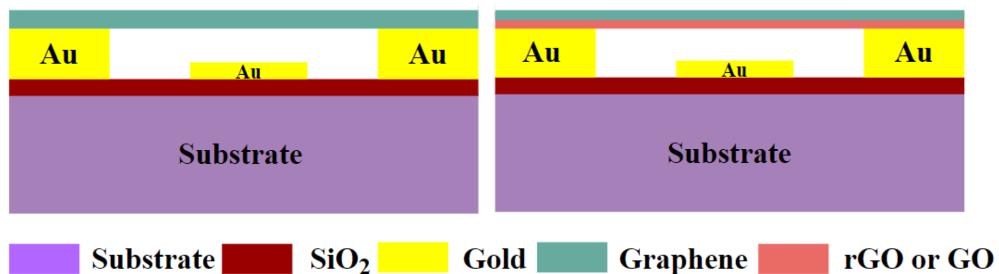

Figure 49: Schematic diagram of (a). single material (b). composite beam NEMS switch

For the designed graphene/RGO NEMS beam of length 2 µm, width 0.3 µm, thickness 5 nm (2.2/2.8 nm), and air gap of 40 nm, the actuation voltage of 9.7 V was obtained as shown in figure 50. The actuation voltage of graphene/GO composite beam structure is (9.7 V), less than the single material graphene beam structure (12.2 V).

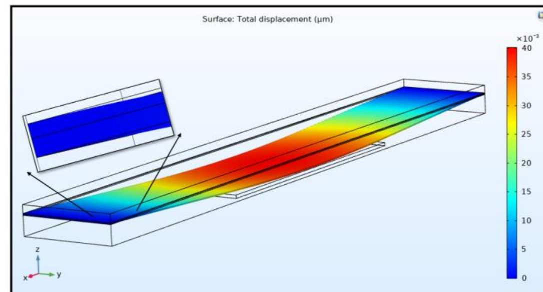

Figure 50: Simulated graphene/RGO NEMS switch

7.6 Analysis of Graphene/GO Composite beam

GO along with graphene is used as composite to observe the effect on performance parameters. The design parameters, in this case, are kept the same as the previous simulation. The only change is that RGO is replaced by GO to form composite beam. The single material graphene beam (5 nm thick) is replaced by graphene/GO composite beam (2.2 nm/2.8 nm). A graphene/GO beam of length 2 µm, width 0.3 µm, and air gap of 40 nm was considered for the pull-in analysis. A 2.2 nm thick graphene beam is placed over 2.8 nm thick GO beam. GO with elastic modulus of 27 GPa and Poisson's ratio of -0.567 was considered for the simulation [62].

For the designed graphene/GO NEMS beam of length 2 µm, width 0.3 µm, thickness 5 nm (2.2/2.8 nm), and air gap of 40 nm, the actuation voltage of 8.3 V was obtained as shown in figure 51. The actuation voltage of graphene/GO composite beam structure is (8.3 V), less than the single material graphene beam structure (12.2 V).

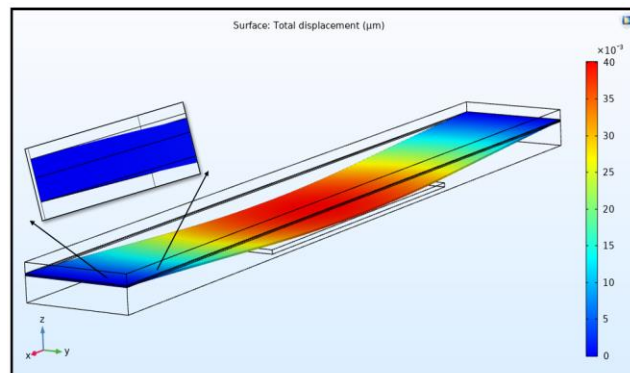

Figure 51: Simulated graphene/GO NEMS switch

The composite beam can be transformed into a beam with an effective elastic modulus and equivalent thickness. The equivalent elastic modulus of the beam can be expressed by equation 18 [44].

$$E_{equi}=\frac{E_1A_1+E_2A_2}{A_1+A_2} \quad (18)$$

E_1, E_2 are elastic modulus values and A_1, A_2 are the values of the cross-sectional area of the two different materials used to form composite beam. The single material beam equivalent to the composite graphene/GO or graphene/RGO beam is shown in figure 52. The calculated value of equivalent elastic modulus is 438 GPa and 348 GPa for graphene/RGO and graphene/GO respectively.

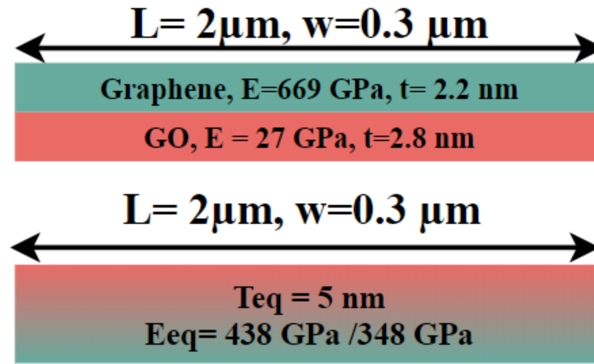

Figure 52: Composite beam represented as its equivalent single material beam

Graphene/GO can be a good choice to form a composite beam as it offers low elastic modulus (equivalent elastic modulus 348 GPa). The composite graphene/GO beam requires a pull-in voltage of 8.3 V but on the other hand, single material graphene beam requires pull-in voltage of 12.2 V. The restoring force for electrostatically actuated single material graphene beam is 101 nN (table 17), graphene/RGO beam is 64.2 nN while it is 47 nN for composite graphene/GO. The composite beam graphene/RGO offers low actuation voltage without much drop in restoring force.

7.7 Modal analysis of single material beam and composite beams

The resonant frequency of the double clamped beam structures is obtained with modal analysis. The obtained eigenfrequency modes of the graphene beam are 24.6 MHz, 67.9 MHz, 100 MHz. For composite beam graphene/RGO, the obtained eigenfrequencies are 17.4 MHz, 48.2 MHz, 75.4 MHz, and for graphene/GO beam the values are 14.4 MHz, 39.7 MHz, 71.7 MHz. This modal analysis was performed for the

beam length of 2 µm, width 0.3 µm, thickness 5 nm (2.2/2.8 nm), and air gap of 40 nm. Figure 53 shows the obtained eigenmodes for single material graphene beam, graphene/RGO, and graphene/GO composite beam. The graphene/GO composite beam resonates at lesser frequency than the other two cases.

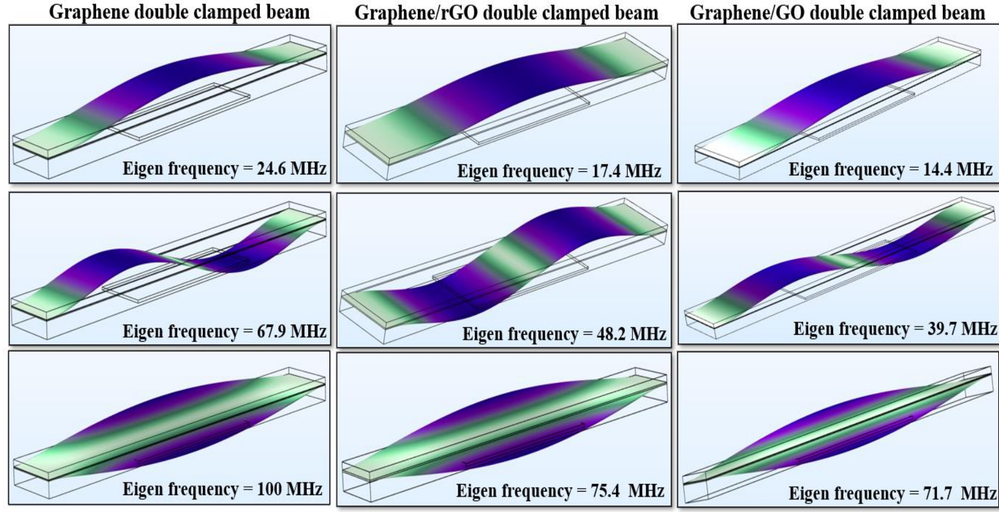

Figure 53: Eigenfrequency analysis of single material beam and composite beams

Switching time is the time required by the switch to come in the off state from on state. Release time is the time taken by the bridge to come to its initial unactuated state after removing the voltage. The switching time (t_s) and release time (t_r) are expressed by equation 19, 20 [167][168]:

$$t_s = 3.67 \frac{V_{pi}}{V_s \omega_o} \tag{19}$$

$$t_r = \frac{1}{4 f_o} \tag{20}$$

Where V_{pi} is the actuation voltage, $V_s = 1.3V_{pi}$, and ω_o is the angular resonant frequency. For the beam length of 2 µm, width 0.3 µm, thickness 5 nm and air gap of 40 nm, the obtained switching time and release time of graphene NEMS switch is 114 ns and 10 ns, respectively. The switching time and release time for composite beams are obtained as shown in table 18. For the same dimensions, the switching time and release time of graphene/RGO NEMS switch are 162 ns and 14 ns, respectively. The switching time and release time of the composite beam graphene/GO are 196 ns and 17 ns, respectively. From the above simulated results, it is evident that single material graphene is the fastest switch as it has the lowest switching time but requires high pull-in voltage for actuation.

Table 18: Single material beam and Composite beam Performance Parameters

Beam material	Beam length (µm)	Pull-in Voltage (V)	Restoring force (nN)	Switching time (nsec)	Release time (nsec)
Graphene	2	12.2	101	114	10
	2.5	8.5	49.2	180	16
	3	6.5	28.8	261	23
	3.5	4.9	16.4	355	31
	4	4	10.9	465	41
Graphene/RGO	2	9.7	64.2	162	14
	2.5	6.7	30.6	254	22
	3	5	17	363	32
	3.5	3.9	10.4	493	43
	4	3.15	6.74	643	56
Graphene/GO	2	8.3	47	196	17
	2.5	5.7	22.2	307	27
	3	4.3	12.6	440	39
	3.5	3.4	7.88	598	52
	4	2.7	4.9	780	69

The variation in the single material graphene beam length from 2 µm to 4 µm leads to the variation in the pull-in voltage and switching time. Figure 54 (a), 54 (b), and 54 (c) show the effect of changing the beam length of the single material graphene beam on pull-in voltage, switching time, release time and restoring force.

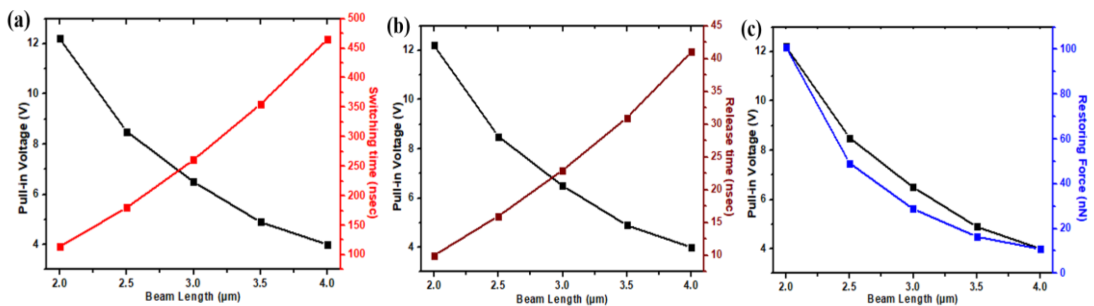

Figure 54: Effect of variation of beam length of single material graphene beam on (a) Switching time and pull-in voltage (b). Release time and pull-in voltage (c). Restoring force and pull-in voltage

The variation in the composite beam length from 2 µm to 4 µm leads to the variation in the pull-in voltage and switching time. Figure 55 (a), 55 (b), and 55 (c) shows the effect of changing the beam length of the graphene/RGO composite beam on pull-in voltage, switching time, release time and restoring force.

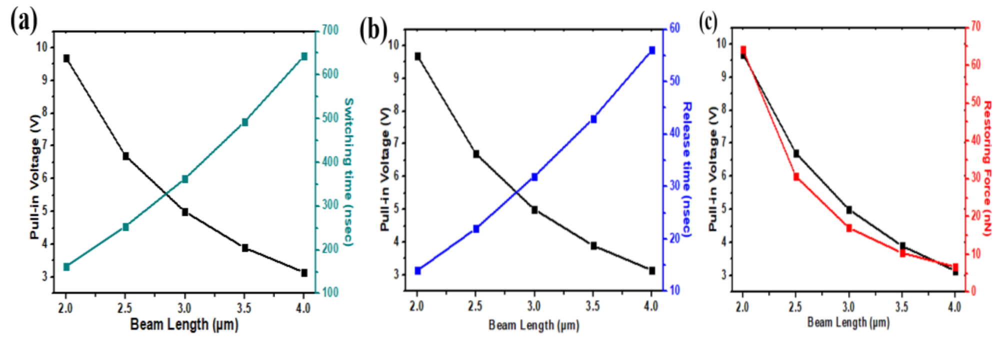

Figure 55: Effect of variation of beam length of graphene/RGO composite beam on (a) Switching time and pull-in voltage (b). Release time and pull-in voltage (c). Restoring force and pull-in voltage

The variation in the graphene/GO composite beam length from 2 µm to 4 µm is simulated. Figure 56 (a), 56 (b), and 56 (c) shows the effect of changing the beam length of the composite graphene/RGO beam on the performance parameters like pull-in voltage, switching time, release time and restoring force.

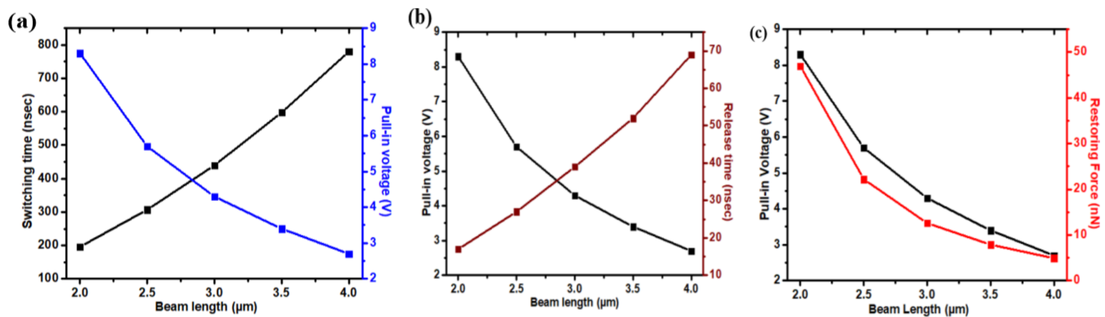

Figure 56: Effect of variation of beam length of graphene/GO composite beam on (a) Switching time and pull-in voltage (b). Release time and pull-in voltage (c). Restoring force and pull-in voltage

The pull-in voltage and restoring force of the composite beam based NEMS switch is decreased by increasing the length of the double clamped beam. While the switching time and release time of the composite double clamped beam gets increased on changing the beam length. Figure 57 (a), 57 (b), 57 (c), 57 (d) shows the variation in the performance parameters by varying the beam length for single material and composite beam. In figure 57 (a) and 57 (b), the variation in pull-in voltage and restoring force is plotted against variation in beam length for graphene, graphene/RGO, and graphene/GO beams. While in figure 57 (c) and 57 (d), the variation in switching time and release time is plotted against variation in beam length for graphene, graphene/RGO, and graphene/GO beams.

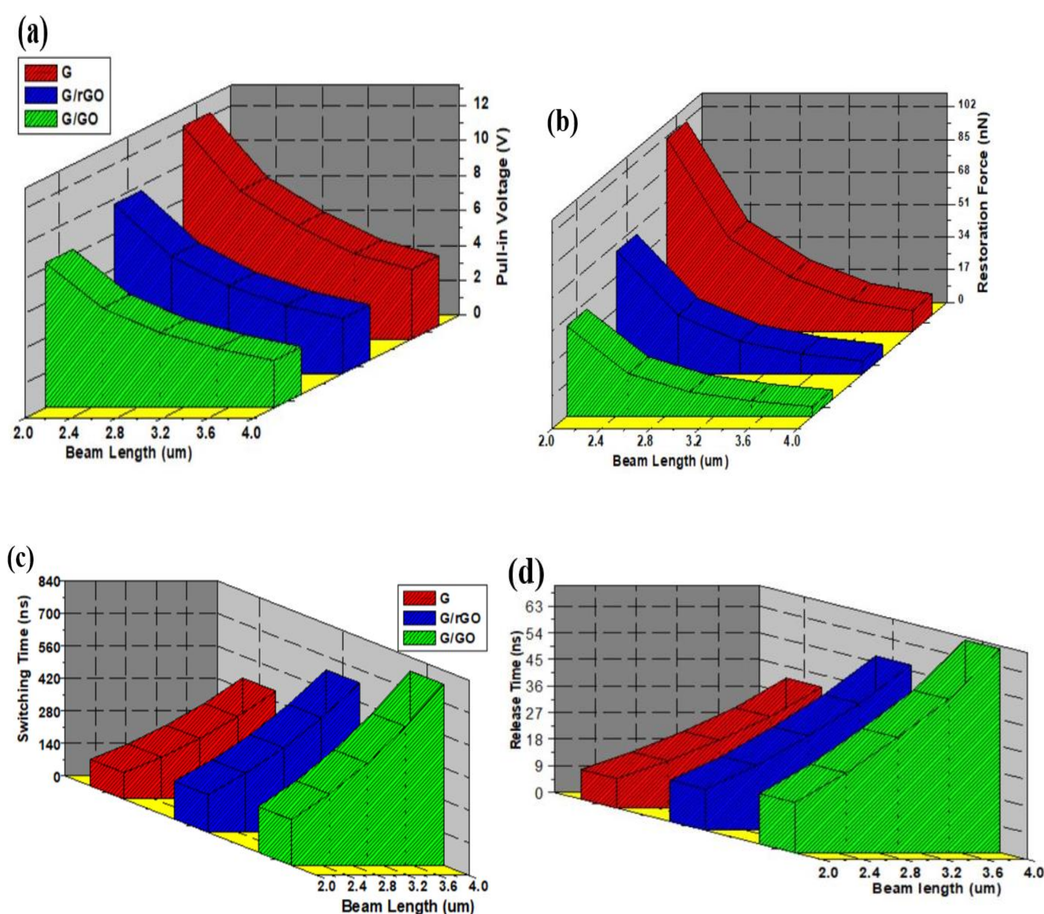

Figure 57: Single material vs Composite material (a) Beam length vs pull-in voltage (b). Beam length vs Restoring force (c). Beam length vs switching time (d). Beam length vs release time

It is clear from the plots that an increase in the beam length reduces the actuation voltage and restoring force while increasing the switching time and release time. Graphene beam exhibits high pull-in voltage, high restoring force with less switching, and release time. while graphene/GO beam requires less pull-in voltage, less restoring force with high switching, and release time. The performance parameters of graphene/RGO beam lies in between the graphene and graphene/GO beam.

For ease of comparison and analysis, the obtained results in this study are summarized in table 19. For 2 μm beam length, the pull-in voltage is reduced by 20% and 31%, and restoring force is reduced by 36% and 53% for graphene/RGO and graphene/GO beams, respectively, as compared to graphene. The switching time is increased by 29%, 41%, and release time gets increased by 28%, 41% for graphene/RGO, and graphene/GO beams, respectively, as compared to graphene beam.

Comparing the results of a single material beam and two composite beams, graphene/GO beam offers very low actuation voltage and high switching time. Comparing the results of 2 µm and 4 µm long composite beam shows that changing the device dimensions reduces the actuation voltage with high loss in restoring force. Thus, it can be concluded that a composite beam based NEMS switch is an ideal choice to achieve low actuation voltage without much fall in restoring force, and graphene beam based NEMS switch can be a good choice when faster switching speed is required. The varying section composite beam approach can be used to lower the pull-in voltage without much drop in restoring force.

Table 19: Comparison of device performance parameters

Beam Type	V_{pi} (V)	F_R (nN)	t_s(ns)	t_r(ns)	% Reduction/Increment			
					V_{pi} (V)	F_R (nN)	t_s(ns)	t_r(ns)
L= 2 µm, W= 0.3 µm, t= 5 nm (2.2/2.8 nm), g= 40 nm								
Graphene	12.2	101	114	10	-	-	-	-
Graphene/RGO	9.7	64.2	162	14	20 (↓)	36 (↓)	29 (↑)	28 (↑)
Graphene/GO	8.3	47	196	17	31 (↓)	53 (↓)	41 (↑)	41 (↑)
L= 4 µm, W= 0.3 µm, t= 5 nm (2.2/2.8 nm), g= 40 nm								
Graphene	4	10.9	465	41	-	-	-	-
Graphene/RGO	3.15	6.74	643	56	21 (↓)	38 (↓)	27 (↑)	26 (↑)
Graphene/GO	2.7	4.9	779	69	32 (↓)	55 (↓)	40 (↑)	40 (↑)

7.8 Summary

In this study, the comparative analysis of graphene, graphene/RGO, and graphene/GO NEMS switches was illustrated using COMSOL Multiphysics.

- The restoring force changes non-linearly on increasing the beam length as compared to the change in elastic modulus. The studies show reduction in actuation and restoring force for graphene/RGO and graphene/GO beam when compared with graphene beam. But this is observed at the expense of an increase in switching time and release time.
- Thus, graphene-based NEMS switch can be used when low switching time is required and graphene/GO NEMS switch can be used when low actuation voltage without much fall in restoring force is desired.

- The performance of the NEMS switch highly rely on pull-in voltage and switching speed and can be further improved by using varying section composite beam structures.

Chapter 8

GRAPHENE CANTILEVER BASED DIGITAL LOGIC GATES

In this chapter, universal logic gates NAND and NOR along with NOT and XOR are successfully implemented using graphene cantilever structures (section 8.3,8.4). 3D modelling of different graphene cantilever structures is demonstrated using COMSOL Multiphysics software. The high electrical conductivity of graphene makes it a better choice as a cantilever beam for this study. The cantilever based simulated logic gates could enable the implementation of different digital circuits.

8.1 Background

The development of microfabrication technology has empowered the production of outstanding micro and nanodevices. NEMS switches are one of the remarkable nanodevices that can replace the already existing switches due to properties like high efficiency, low actuation voltage, high switching speed, etc. [21][8]. The switching action can be achieved by either cantilever or double clamped bridge-based structure [169][170]. A cantilever beam is fixed at one end and another end freely moves when it is under some external stress. For the sensing application like physical, biological, or chemical sensing, microcantilever structures are used. The sensing is achieved by detecting the changes in cantilever bending [171]. The double clamped bridge-based structure is fixed at both ends. The bending of the beam is achieved by applying actuation in the middle of the structure [45]. NEMS switches can be used for switching applications [172], data storage [54], low power digital computing [173], and logic gates [174], etc. The implementation of compact XOR/XNOR gates was reported using only two laterally-actuated double-gate NEMS switches [175]. The logic gate implementation using microplasma was performed with high operating voltage [176]. Also, AlN based switches were implemented as NAND and NOR gate functions with an operating voltage of 2V [177]. Various NEMS switch structures for applications like wireless sensors [178] and addressable memory component [179] have been reported.

Graphene beams have been an intriguing area of research from the last two decades [180]. The thermal stress coefficient of expansion of graphene paper-based cantilever structure was studied [181]. The fabrication of a cantilever-based graphene structure is

difficult than fixed beam structures. But graphene cantilever is a promising candidate for different NEMS devices [16]. Graphene cantilever as nano switch was fabricated and the mechanical properties of graphene cantilever were studied using atomic force microscopy [182]. The interesting mechanical [18], thermal [183], and electrical [57] properties of graphene make it suitable for various applications. Multilayer graphene [184] is always preferred over monolayer graphene due to high conductivity and high stiffness [144].

In this study, the implementation of graphene cantilever-based different logic gates like NOT, NOR, NAND, and XOR using electrostatic actuation mechanism has been done. Different cantilever structures in a different configuration are used to implement various logic gates.

8.2 Device dimensions and operating principle

The device dimensions of the simulated cantilever structure are given in table 20. A 2 µm long, 0.2 µm wide, and 5 nm thick graphene cantilever is modelled in COMSOL Multiphysics. The Young's modulus of 860 GPa and Poisson's ratio of 0.17 is taken for multilayer graphene for all FEM simulation [148]. The air gap between the cantilever and the actuation electrode is taken as 50 nm.

Table 20: Dimensions of graphene cantilever

Parameters	Values
Beam width	0.2 µm
Thickness	5 nm
Length	2 µm
Gap between beam and bottom electrode	50 nm
Actuation electrode area	200*200 nm

The electrostatic actuation mechanism is used for the operation of the cantilever. At the fixed end, the signal line is connected. For the successful implementation of digital logic gates, the signal line carries a positive voltage signal. Because of the high signal line, the cantilever always acquires some positive potential. The operation of cantilever depends upon the polarity of the voltage applied at the bottom actuation electrode. When the applied voltage is +ve (high), due to repulsion between the cantilever positive polarity and actuation electrode positive polarity, the beam remains in upstate as shown in figure 58. But when the applied

voltage is 0V (low), the actuation electrode will attract the cantilever in downward and the cantilever touches the output port as shown in figure 59. Hence signal passes from input to output and high voltage is obtained. If the signal line is at 0V, the output signal will be zero always irrespective of the polarity of the actuation electrode.

The actuation voltage of cantilever beam can be increased or decreased by changing the beam dimensions or by changing the air gap.

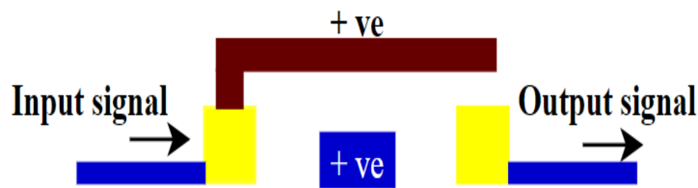

Figure 58: Cantilever operation in Upstate

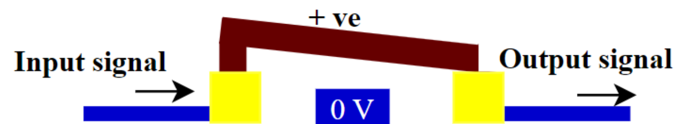

Figure 59: Cantilever operation in Downstate

8.3 Logic gate implementation

8.3.1 NOT gate

For NOT gate implementation, one graphene cantilever and one actuating electrode (V_1) are used. The input signal is applied at the fixed end of cantilever while the output is taken at the free end as shown in figure 60. The truth table of NOT gate is given in table 21.

When 0 V is applied voltage at the actuating electrode and cantilever voltage is equal to pull-in voltage/actuation voltage, the electrostatic actuation mechanism pulls the cantilever in the downward direction, and the beam touches the output port. Hence the input from the cantilever beam is taken at the output port.

When the applied voltage at actuating electrode is equal to pull-in voltage (V_{pi}) and cantilever voltage is equal to pull-in voltage/actuation voltage, the positive polarity of both actuating electrode and cantilever beam will repel each other and the beam remains in up direction. No output is obtained at the output port.

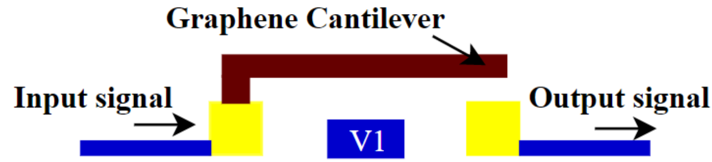

Figure 60: NOT gate structure

Table 21: Truth table of NOT gate

Input	V_1	Output
1	0	1
1	1	0

8.3.2 NOR gate

For NOR gate implementation, two graphene cantilevers and two actuating electrodes (V_1,V_2) are used. Both cantilever structures are connected in series. The input signal is applied at the fixed end of the first cantilever while the output is taken from the free end of the second cantilever as shown in figure 61. The truth table of NOR gate is given in table 22.

When both inputs (00) are at 0 V, the first cantilever is closed first due to electrostatic actuation and high output is generated. The output of the first cantilever is applied as input to the second cantilever and still the second actuating electrode is at 0V then high output is obtained at the second cantilever port.

When one of the inputs is high (01), the cantilever one obtains high output. But the second cantilever obtains 0 output because the second actuating electrode is at high potential. When the input applied at the actuating electrode is, one is high and another low (10). The first cantilever remains in the upward direction and zero output is obtained at the output port of the first cantilever. Since the second actuating electrode is at 0 V, the overall output obtained is 0.

When pull-in voltage is applied at both the inputs (11), the first cantilever remains in the upstate. Since no output is obtained at the output port of the first cantilever, the overall output obtained is 0V.

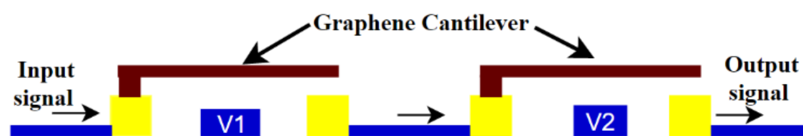

Figure 61: NOR gate structure

Table 22: Truth table of NOR gate

Input	V_1	V_2	Output
1	0	0	1
1	0	1	0
1	1	0	0
1	1	1	0

8.3.3 NAND gate

For NAND gate implementation, two graphene cantilevers and two actuating electrodes (V_1,V_2) are used. Both cantilever structures are connected in parallel. The input signal is applied at the fixed end of both cantilevers while the output is taken from the free end of both cantilevers as shown in figure 62. The truth table of NAND gate is given in table 23.

When both inputs (00) are at 0 V, both cantilevers are closed due to electrostatic actuation and high output is generated. When one of the inputs is high (01, 10), one of the cantilevers remains in downstate and obtains high output. When pull-in voltage is applied at both the inputs (11), both cantilevers remain in upstate and no output is obtained at output port.

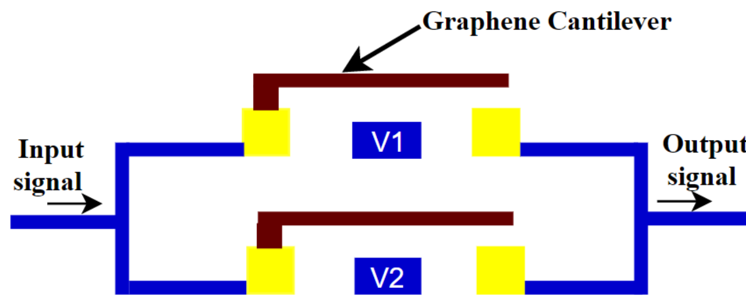

Figure 62: NAND gate structure

Table 23: Truth table of NAND gate

Input	V_1	V_2	Output
1	0	0	1
1	0	1	1
1	1	0	1
1	1	1	0

8.3.4 XOR gate

For XOR gate implementation, one graphene cantilever and two actuating electrodes (V_1,V_2) are used. The input single is applied at the fixed end of cantilever while the output is taken at the free end as shown in figure 63. The truth table of NAND gate is given in table 24.

When both inputs (00) are at 0 V, both actuating electrodes will try to pull the beam and as a result, the cantilever remains in the initial position. Hence no output is obtained. When both inputs are high (11), both actuating electrodes will try to repel the beam and as a result, the cantilever remains in the initial position. Hence no output is obtained. But when one of the inputs is low (01,10), the beam will be deflected towards the actuating electrode at ground potential, and output is obtained.

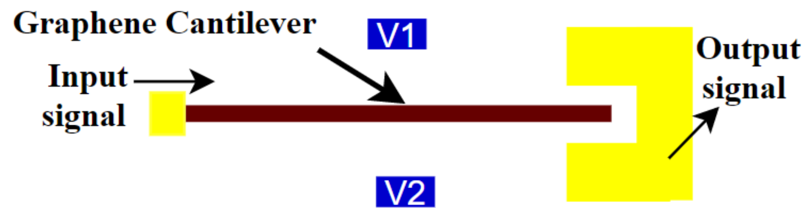

Figure 63: XOR gate structure

Table 24: Truth table of XOR gate

Input	V_1	V_2	Output
1	0	0	0
1	0	1	1
1	1	0	1
1	1	1	0

8.4 Results and discussion

The NEMS switch-based logic gates are designed and simulated in COMSOL Multiphysics version 5.4. The device dimensions of the simulated cantilever are already listed in table 20. Structural mechanics and AC-DC modules are used for simulating the logic gate structures. For all simulations, logic 1 equals the actuation voltage i.e. 1.57 V.

8.4.1 NOT gate implementation

The simulation results obtained for NOT gate implementation are shown in figure 64. 3D model of NOT gate is shown, when the actuation voltage is low and when the actuation voltage is high. In both cases, cantilever is at voltage equals to actuation voltage (1.57 V). For low actuation voltage, the cantilever touches the output port. Hence signal passes from input to output and high output is obtained. For high actuation voltage, the cantilever remains in the upstate and at the output port, no output is obtained.

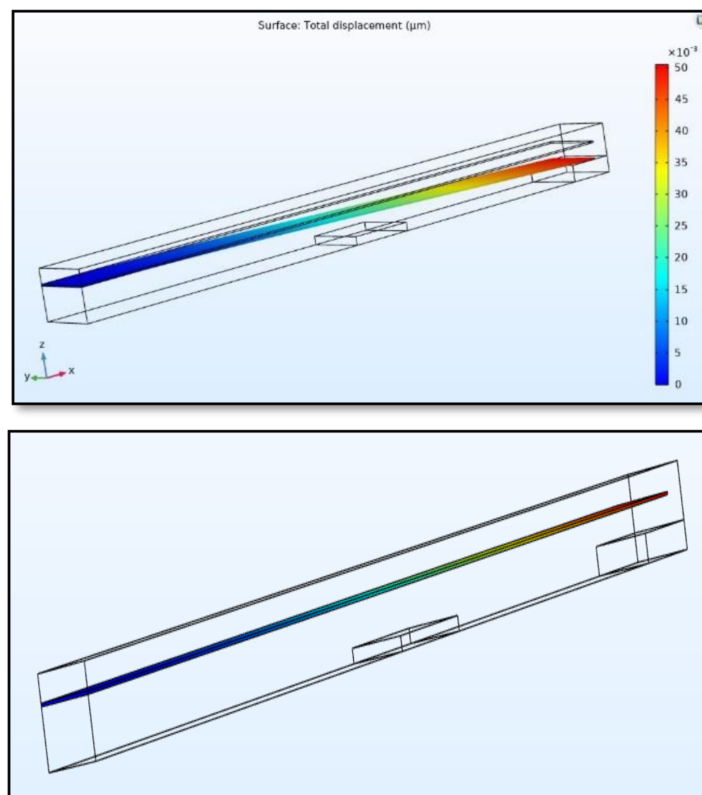

Figure 64: 3D model of NOT gate (a) when $V_1 = 0$ (b) when $V_1 = 1$

8.4.2 NOR gate implementation

The simulation results obtain for NOR gate implementation are shown in figure 65. The 3D model of NOR gate is shown for the four cases (V_1,V_2) (00,01,10,11). In all four cases, the first cantilever is at actuation voltage while the second cantilever attains actuation voltage only when the output of the first cantilever is high. When the actuation voltages are V_1V_2 = 00, high output is obtained because in this case, both cantilevers touch their respective output ports. Hence signal passes from input to output. For the

remaining cases either one cantilever is in upstate or both the cantilevers are in upstate and zero output is obtained.

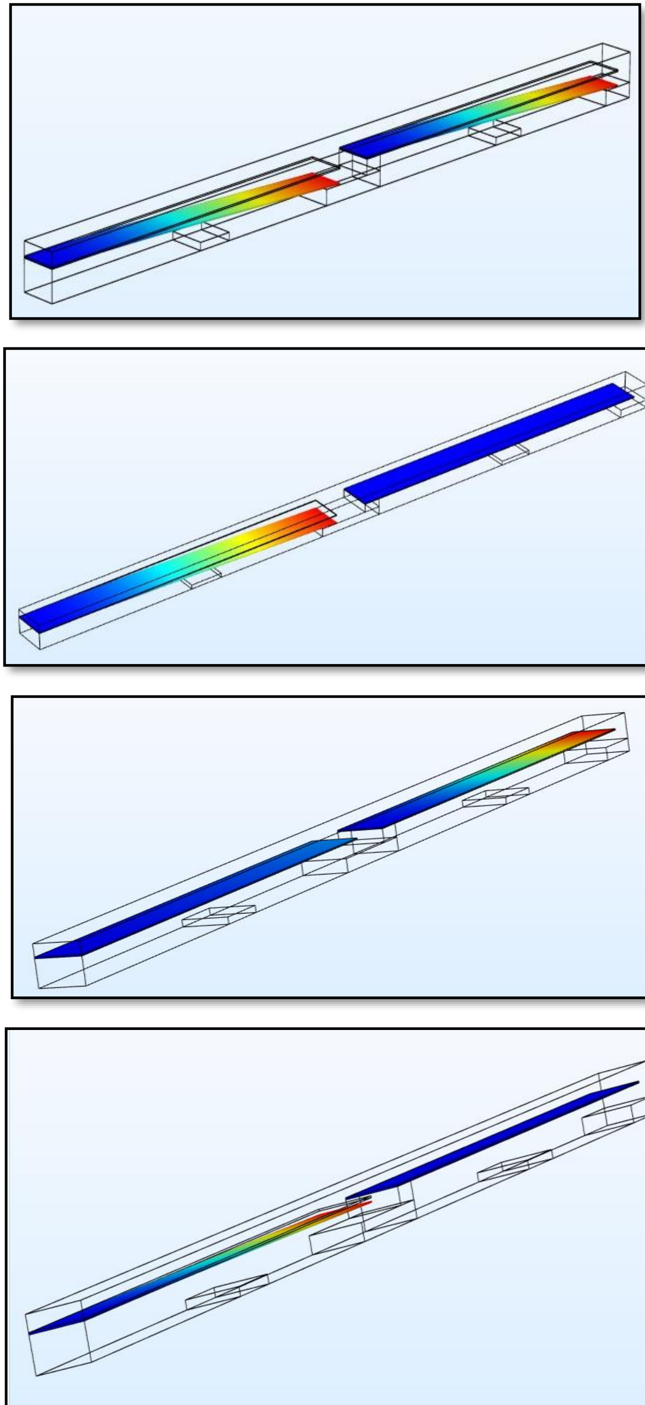

Figure 65: 3D model of NOR gate (a) when V_1V_2= 00 (b) when V_1V_2= 01 (c) when V_1V_2= 10 (d) when V_1V_2= 11

8.4.3 NAND gate implementation

The obtained simulation results for NAND gate implementation are shown in figure 66. The 3D model of NAND gate is shown for the four cases (V_1,V_2) (00,01,10,11). In all four cases, both the cantilevers are at actuation voltage. When both inputs are low or one of the inputs is low, high output is obtained because in this case, cantilever touches the respective output ports. Hence signal passes from input to output. When the actuation voltages are V_1,V_2 =11, the low output is obtained because in this case both cantilevers are in upstate and zero output is obtained.

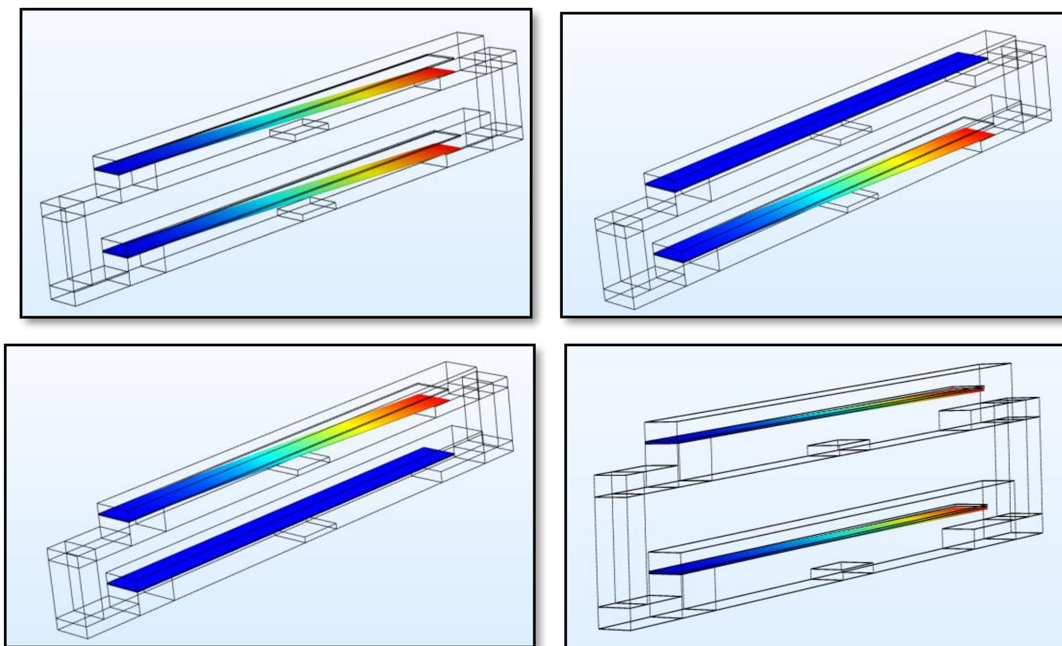

Figure 66: 3D model of NAND gate (a) when V_1V_2= 00 (b) when V_1V_2= 01 (c) when V_1V_2= 10 (d) when V_1V_2= 11

8.4.4 XOR gate implementation

The simulation results obtain for XOR gate implementation are shown in figure 67. The 3D model of XOR gate is shown for the four cases (V_1,V_2) (00,01,10,11). In this case, cantilever is at actuation voltage for all four cases. When the actuation voltages are V_1,V_2= 01 or 10, high output is obtained because in this case, at least one cantilever touches the respective output port. Hence signal passes from input to output. For the remaining cases (00,11), the cantilevers are in upstate and zero output is obtained.

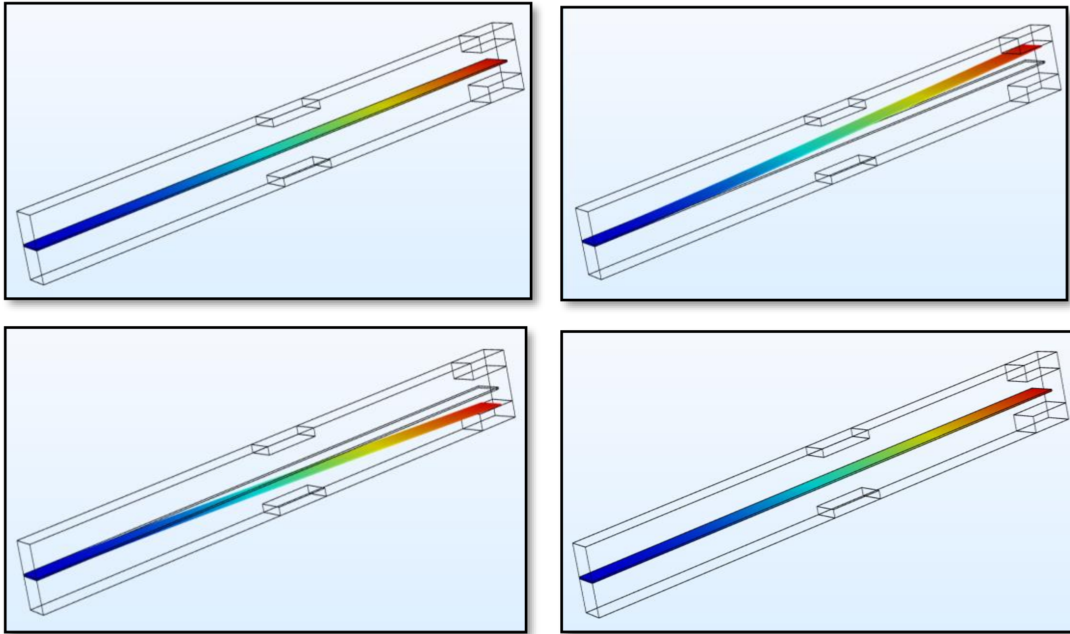

Figure 67: 3D model of XOR gate (a) when V_1V_2= 00 (b) when V_1V_2= 01 (c) when V_1V_2= 10 (d) when V_1V_2= 11

8.5 Switching speed

The switching time of NEMS switch is approximated by equation 19. The switching time of 45 ns has been obtained for graphene cantilever NEMS switch. Since the device dimensions of the cantilever beam is the same in all the cases and the actuation voltage is also the same hence the same switching speed has been obtained.

8.6 Summary

- In this work, the successful demonstration of the graphene cantilever based NEMS switch is done. The designed NEMS switches are implemented as different digital logic gates. The actuation voltage of 1.57 V is obtained for the 5 nm thick graphene cantilever when the cantilever completely touches the output port.
- The proposed NEMS logic gate NAND and NOR are universal gate, using these any other gate can be implemented. The digital circuit like adders and multiplexers can be easily realized by the simulated digital logic gates.
- The practical realization of XOR gate can be done. The actuating electrodes can be placed on the both sides of cantilever and lateral actuation can be carried out to achieve switching mechanism.

Chapter 9

CONCLUSION AND FUTURE SCOPE

This chapter concludes the research work done in this thesis. This chapter also elaborates that how the designed and analysed proposed structures can be used to implement various other structures and their future perspective.

9.1 Conclusion

The proposed work on graphene materials-based RF NEMS shunt switches has been carried out systematically. Different NEMS switch structures and dimensions are designed and analyzed. The original contributions of the proposed work are discussed below:

- The pull-in response and mechanical reliability of GO-based NEMS switch were investigated for both standard and perforated GO beams. The perforated beam structure is preferred over standard beam structure as it requires low pull-in voltage. From the von Mises stress analysis, it is evident that von Mises stress values in GO NEMS switch is less than graphene NEMS switch. This lesser value of von Mises stress in GO NEMS switch makes it a good choice as beam material. The variation in capacitance was successfully demonstrated when the suspended beam actuated towards the bottom graphene electrode. The proposed structure, GO-based NEMS switch could be used for data storage and memory applications.
- The pull-in stability and eigenfrequency analysis of gold/GO-based NEMS switch have been performed for intact and circularly perforated structures. The circularly perforated structure gets actuated at a voltage less than the intact structure. By making perforations, the air below the suspended beam is easily squeezed out through the perforations, hence reducing the actuation voltage. It is observed that by making perforations, the pull-in voltage and eigenfrequencies are reduced. The pull-in voltage can be further reduced by changing the perforation size/shape.
- The performance analysis for GO NEMS shunt switch at RF has been evaluated for the first time. The S-parameter of monolayer and multilayer GO-based switches are analyzed for 1-60 GHz. The results show that monolayer GO

NEMS switch acquires low pull-in voltage, and exhibits high downstate capacitance. Both the simulated switch structures provide high switching speed and good RF performance.

- Also, graphene-based NEMS switch with different bridge structures has been designed and simulated to find out which structure requires the least pull-in voltage. It is clear from the simulated results that hinge structure-based NEMS switch requires the least pull-in voltage as actuation voltage depends upon the bridge stiffness. The different bridge structures have different spring stiffness. The perforations reduce the mass of the suspended beam and make beam less stiff which in turn changes the actuation voltage.
- Further, the detailed analysis of variation in device design parameters such as length and thickness of the suspended beam, air gap was studied. The effect of changing the device design parameters on actuation voltage and von Mises stress was observed. The pull-in voltage was reduced to 50% while increasing the beam length from 1 µm to 1.6 µm. Moreover, it also has been identified that the pull-in voltage has increased to 313% and 320% on changing the beam thickness from 2.8 nm to 4.9 nm and air gap from 30 nm to 60 nm, respectively. The von Mises can be reduced by increasing the length of GO, decreasing the thickness of GO, and the air gap between the GO and bottom electrode.
- The RF performance analysis of the proposed switch exhibited high isolation and low insertion loss. It can be concluded that the long and thin GO beam requires less actuation voltage, it can endure less von Mises stress and exhibits good RF performance.
- Also, graphene derivatives i.e. GO and RGO based NEMS shunt capacitive switches were designed and modelled. The comparative analysis of graphene NEMS and graphene derivatives composite beam based NEMS switches were performed in terms of pull-in voltage and restoring force. Two different methods were used to analyze the impact on restoring force either by changing the beam length or by changing the elastic modulus.
- The studies show the reduction in the actuation voltage and restoring force for graphene/RGO and graphene/GO fixed-fixed beam structures when compared with the graphene beam. But this is observed at the expense of increase in

switching time and release time. However, graphene-based NEMS switches can be used when low switching time is required and graphene/GO NEMS switches can be used when low actuation voltage without much fall in restoring force is desired.

- The performance of NEMS switches highly rely on pull-in voltage and switching speed and can be further improved by using varying section composite beam structures.
- The successful implementation of the graphene cantilever based NEMS switches have been carried out as different digital logic gates. In this work, the simulated NEMS switch required very low actuation voltage.
- The proposed NEMS logic gates NAND and NOR are universal gate, using those any other gate can be implemented. The digital circuit like adders and multiplexers can be easily realized by the simulated digital logic gates.

Table 25 summarises the comparison between the results of proposed switches with the existing work. Based on the results, it can be concluded that GO can be a good choice as a suspended beam for RF NEMS switch. GO-based NEMS switches can be preferred in the application that requires low actuation voltage, high switching speed, and good RF performance. It can also be used for data storage and memory applications.

Table 25: Proposed switch comparison with existing work

References	**Beam Material/ Dielectric**	**Pull-in Voltage (V)**	**S-parameters** Isolation (S_{21}), Insertion loss (S_{21}')
Sharma at al. 2013	Graphene/HfO_2	< 2	Monolayer, S_{21}= >10 dB, S_{21}'= 0.01–0.3 dB @ 1-60 GHz. Multilayer, S_{21}= >20 dB, S_{21}'= 0.01–0.2 dB @ 1-60 GHz
Ma et al. 2016	Al/SiO_2	3.04	S_{21} = 24 dB S_{21}'= 5.65 dB @ 40 GHz
Zhao et al. 2017	Au/Si_3N_4	18.3	S_{21} = 20.5 dB S_{21}'= 0.29 dB @35
Angira et al. 2019	Au-Cr/HfO_2	12	S_{21} = -52.7 dB S_{21}'= 0.06 dB @9 GHz
Proposed work (Monolayer)	Graphene-GO/GO	7.5	S_{21} = >70 dB S_{21}'= 0.03-0.05 dB@1-60 GHz
Proposed work (Multilayer)	Graphene-GO/GO	9.8	S_{21} = >70 dB S_{21}'= 0.03-0.06 dB@1-60 GHz
Proposed work (Hinge Structure)	Graphene-GO/GO	1.5	S_{21} = >70 dB S_{21}'= 0.02-0.03 dB@1-60 GHz

9.2 Future scope

The work presented in this thesis have shown that how the limitations of RF MEMS switches can be addressed by taking a novel material as a suspended beam. Further work can be initiated in the broad areas given below:

- In the current study, the performance of designed switches has not considered the effect of intermolecular forces such as Casimir force and Van der Waals force. These studies can be carried out in future.
- The concept of implementing the high switching speed digital logic gates could be applied to realization of flip-flops.
- The design and modelling of the graphene derivative based NEMS switches as DRAM or SRAM memory cell can be implemented. Following the concept, the multiple memory cells, data storage registers can be designed. The implemented memory cells and registers could acquire high speed that can be used in communication systems and other applications.
- MEMS switches are used in the switching network of the communication systems for different frequency bands. MEMS phase shifters have low switching speed and the disadvantage can be overcome by using composite beam of graphene materials like GO/RGO.
- The work presented in this thesis can be extended to simulation, fabrication, and characterization of GO-NEMS switch for various configurations like SPST (single pole single throw), SPDT (single pole double throw), etc. These configurations could have low pull-in voltage, good RF performance and high switching speed.
- RF NEMS switches can be used in the switching network of transceivers applications for signal routing. The steps for the practical realization (figure 68) of the proposed RF NEMS switch are:

  (a). A low loss Silicon substrate is considered, (b). a cavity is formed by etching the substrate, (c). deposition of dielectric layer over the etched substrate, (d). deposition of CPW line over the dielectric layer, (e). sacrificial layer deposition to fabricate suspended beam at some gap over signal line, (f). deposit suspended beam over sacrificial layer, (g). sacrificial layer deposition and deposition of top

electrode over suspended beam, (h). remove sacrificial layer and hanging bridge structure is released.

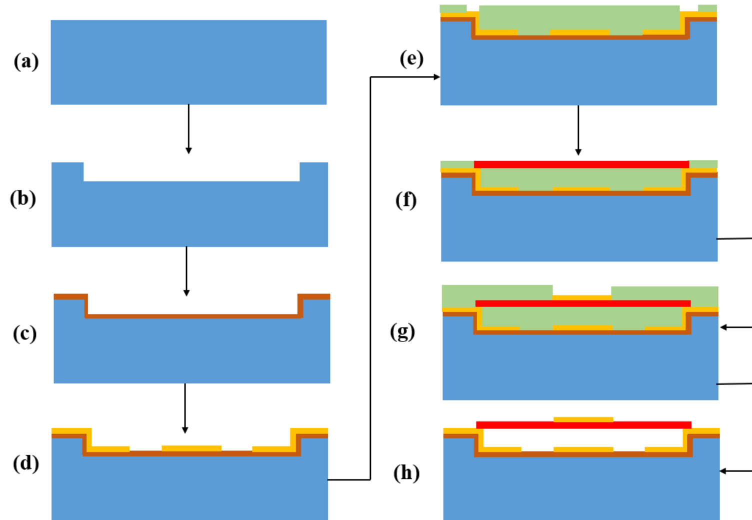

Figure 68: Fabrication Process flow of proposed RF NEMS switch

- Cantilever based NEMS switches (XOR gate) can be practical realized (figure 69) by using by two different process technologies:

(a). Si substrate (b). Growth of SiO_2 over the substrate. (c). Deposition and patterning of gold electrodes. (d). Deposition of amorphous SiO_2 as a sacrificial layer and Over sacrificial layer, mechanical exfoliation method is used to transfer graphene cantilever. By using Focused ion beam technique (FIB), the graphene layer can be placed on the middle part of the electrode in the vertical direction (e). Removal of sacrificial layer to get suspended cantilever structure (f). Top view of the fabricated structure.

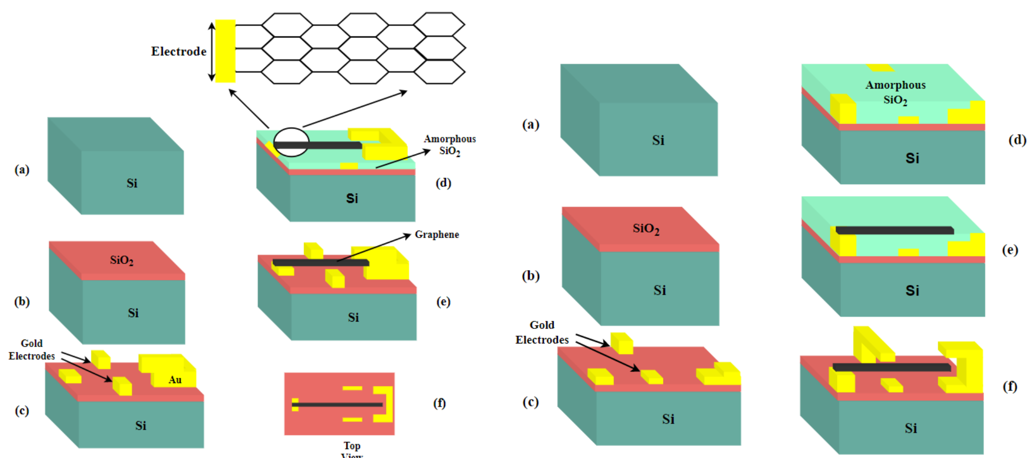

Figure 69: Fabrication Process flow of Cantilever NEMS shunt switch (XOR gate)

Bibliography:

[1] M. Lundstrom, “Is Nanoelectronics the Future of Microelectronics ?,” *Proceedings of the 2002 international symposium on Low power electronics and design*, pp. 172–177, 2002.

[2] A. D. Franklin, “Nanomaterials in transistors: From high-performance to thin-film applications,” *Science*, vol. 349, no. 6249, pp.1–9, Aug. 2015.

[3] S. M. Dubois, Z. Zanolli, X. Declerck, and J. C. Charlier, “Electronic properties and quantum transport in Graphene-based nanostructures,” *Eur. Phys. J. B*, vol. 72, no. 1, pp. 1–24, Nov. 2009.

[4] K. I. Bolotin et al., “Ultrahigh electron mobility in suspended graphene,” *Solid State Commun.*, vol. 146, no. 9–10, pp. 351-355, June 2008.

[5] K. B. K. Teo et al., “Uniform patterned growth of carbon nanotubes without surface carbon,” *Appl. Phys. Lett.*, vol. 79, pp. 1534, Sep. 2001.

[6] K. S. Yeo and K. Roy, *Low Voltage, Low Power VLSI Subsystems.* New York, McGraw-Hill, 2005.

[7] H. Jaafar, K. S. Beh, N. A. M. Yunus, W. Z. Hasan, S. Shafie, and O. Sidek, “A comprehensive study on RF MEMS switch,” *Microsyst. Technol.*, vol. 20, no. 12, pp. 2109–2121, Dec. 2014.

[8] O. Y. Loh and H. D. Espinosa, “Nanoelectromechanical contact switches,” *Nat. Nanotechnol.*, vol. 7, no. 5, pp. 283–295, May 2012.

[9] M. N. Lovellette et al., “Nanotube Memories for Space Applications,” *IEEE Aerospace Conference Proceedings*, vol. 4, pp. 2300–2305, Mar. 2004.

[10] T. H. Lee, S. Bhunia and M. Mehregany, “Electromechanical Computing at 500 ° C with Silicon Carbide,” *Science*, vol. 329, no. 5997, pp. 1316–1318, Sep. 2010.

[11] L. M. Jonsson, S. Axelsson, T. Nord, S. Viefers, and J. M. Kinaret, “High frequency properties of a CNT-based nanorelay,” *Nanotechonologynology*, vol. 15, no. 11, p. 1497, Sep. 2004.

[12] S. J. Choi et al., “Transformable Functional Nanoscale Building Blocks with Wafer-Scale Silicon Nanowires,” *Nano Lett.*, vol. 11, no. 2, pp. 854–859, Feb. 2011.

[13] H. F. Dadgour, M. M. Hussain, C. Smith, and K. Banerjee, “Design and Analysis of Compact Ultra Energy-Efficient Logic Gates Using Laterally-Actuated Double-Electrode NEMS,” *Proceedings of the 47th Design Automation Conference*, pp. 893–896, June 2010.

[14] P. Bhattacharya, C. K. Das, and S. S. Kalra, “Graphene and MWCNT: potential candidate for microwave absorbing materials.,” *J. Mater. Sci. Res.*, vol. 1, no. 2, pp. 126, Apr. 2012.

[15] M. Dragoman et al., “Graphene for Microwaves,” *Microw. Mag. IEEE*, vol. 11, no. 7, pp. 81–86, Nov. 2010.

[16] C. Lee, X. Wei, J. W. Kysar, and J. Hone, “Measurement of the elastic properties and intrinsic strength of monolayer graphene,” *Science*, vol. 321, no. 5887, pp. 385–388, July 2008.

[17] X. Du, I. Skachko, A. Barker, and E. Y. Andrei, “Approaching ballistic transport in suspended graphene,” *Nat. Nanotechnol.*, vol. 3, no. 8, pp. 491–495, Aug. 2008.

[18] A. A. Balandin *et al.*, “Superior Thermal Conductivity of Single-Layer Graphene 2008,” *Nano Lett.*, vol. 8, no. 3, pp. 902–907, Mar. 2008.

[19] R. Cheng et al., “High-frequency self-aligned graphene transistor with transferred gate stacks,” *Proc. Natl. Acad. Sci.*, vol. 109, no. 29, pp. 11588–11592, July 2012.

[20] S. J. Han, A. V. Garcia, S. Oida, K. A. Jenkins, and W. Haensch, “Graphene radio frequency receiver integrated circuit,” *Nat. Commun.*, vol. 5, no. 1, pp. 1–6, Jan. 2014.

[21] P. Sharma, J. Perruisseau-Carrier, C. Moldovan, and A. M. Ionescu, “Electromagnetic performance of RF NEMS graphene capacitive switches,” *IEEE Trans. Nanotechnol.*, vol. 13, no. 1, pp. 70–79, Nov. 2014.

[22] J. Sun, M. E. Schmidt, M. Muruganathan, H. M. Chong, and H. Mizuta, “Large-scale nanoelectromechanical switches based on directly deposited nanocrystalline graphene on insulating substrates,” *Nanoscale*, vol. 8, no. 12, pp. 6659–6665, Mar. 2016.

[23] S. Lucyszyn, “Review of radio frequency microelectromechanical systems technology,” *IEE*

Proceedings-Science, Meas. Technol., vol. 151, no. 2, pp. 93–103, Mar. 2004.

[24] P. Gammel, G. Fischer, and J. Bouchaud, “RF MEMS and NEMS Technology , Devices , and Applications,” *Bell Labs Tech. J.*, vol. 10 , no. 3, pp. 29–59, Oct. 2005.

[25] C. H. Fox, X. Chen, H. W. Jiang, P. B. Kirby, and S. McWilliam, “Development of micromachined RF switches with piezofilm actuation,” *Smart Struct. Mater. Smart Electron. MEMS, Nanotechnol. Int. Soc. Opt. Photonics.*, vol. 4700, pp. 40–49, July 2002.

[26] S. J. Gross, S. Tadigadapa, T. N. Jackson, S. Trolier-McKinstry, and Q. Q. Zhang, “Lead-zirconate-titanate-based piezoelectric micromachined switch,” *Appl. Phys. Lett.*, vol. 83, no. 1, pp. 174-176, July 2003.

[27] R. M. Proie, R. G. Polcawich, J. S. Pulskamp, T. Ivanov, and M. E. Zaghloul, “Development of a PZT MEMS switch architecture for low-power digital applications,” *J. Microelectromechanical Syst.*, vol. 20, no. 4, pp. 1032–1042, June 2011.

[28] I. J. Cho, T. Song, S. H. Baek, and E. Yoon, “A low-voltage and low-power RF MEMS series and shunt switches actuated by combination of electromagnetic and electrostatic forces,” *IEEE Trans. Microw. Theory Tech.*, vol. 53, no. 7, pp. 2450–2457, July 2005.

[29] I. J. Cho, and E. Yoon, “Design and fabrication of a single membrane push-pull SPDT RF MEMS switch operated by electromagnetic actuation and electrostatic hold,” *J. Micromechanics Microengineering*, vol. 20, no. 3, pp. 035028, Mar. 2010.

[30] Y. H. Zhang, G. Ding, X. Shun, D. Gu, B. Cai, and Z. Lai, “Preparing of a high speed bistable electromagnetic RF MEMS switch,” *Sensors Actuators A Phys.*, vol. 134, no. 2, pp. 532-537, Mar. 2007.

[31] E. Taati, "Analytical solutions for the size dependent buckling and postbuckling behavior of functionally graded micro-plates," *International Journal of Engineering Science*, vol. *100*, pp. 45-60, Mar. 2016.

[32] H. J. De los Santos, G. Fischer, H. A. C. Tilmans, and J. T. M. Van beek, “RF MEMS for ubiquitous wireless connectivity,” *Fabrication, Microwave Magazine, IEEE*, vol. 5, pp. 36–49, Dec. 2004.

[33] G. M. Rebeiz, *RF MEMS: theory design and technology*. John Wiley & Sons, 2004.

[34] J. K. Vijay, K. J. Varadan, and K. A. Jose, *RF MEMS and their applications*. Wiley, 2002.

[35] M. Pallay and S. Towfighian, “A reliable MEMS switch using electrostatic levitation,” *Appl. Phys. Lett.*, vol. 113, no. 21, pp. 213102, Nov. 2018.

[36] L. Mercado, S. M. Kuo, T. Y. T. Lee, and L. Liu, “A mechanical approach to overcome RF MEMS switch stiction problem.,” *Electronic components and Technology conference IEEE*, pp. 377–384, May 2003.

[37] O. Loh, X. Wei, C. Ke, J. Sullivan, and H. D. Espinosa, “Robust Carbon-Nanotube-Based Nano-electromechanical Devices : Understanding and Eliminating Prevalent Failure Modes Using Alternative Electrode Materials,” *Small*, vol. 7, no. 1, pp. 11–13, Jan. 2011.

[38] H. Dadgour, A. M. Cassell, and K. Banerjee, “Scaling and Variability Analysis of CNT-Based NEMS Devices and Circuits with Implications for Process Design,” *IEEE Int. Electron Devices Meet. IEEE*, pp. 1–4, Dec. 2008.

[39] Y. L. Lai, L. C. Chou, Y. Z. Juang, H. H. Tsai, S. C. Huang, and J. C. Chiou, “Development of a novel thermal switch through CMOS MEMS fabrication process,” *Micromach. Microfabr. Process Technol. XVI*, vol. 7926, pp. 79260J, Feb. 2011.

[40] G. F. Pedersen, K. Olesen, and S. L. Larsen, “Bodyloss for handheld phones,” *IEEE 49th Vehicular Technology Conference*, vol. 2, pp. 1580–1584, May 1999.

[41] G. K. Fedder, “MEMS fabrication,” *Proceedings of the IEEE international test conference,* pp. 691, Sep. 2003.

[42] R. Barretta, F. M. De Sciarra, and M. Marotti, “Small-scale effects in nanorods,” *Acta Mech.*, vol. 225, no. 7, pp. 1945–1953, July 2014.

[43] K. S. Rao, L. N. Thalluri, K. Guha, and K. G. Sravani, “Fabrication and Characterization of

Capacitive RF MEMS Perforated Switch," *IEEE Access*, vol. 6, pp. 77519-77528, Dec. 2018.
[44] M. Manivannan, R. J. Daniel, and K. Sumangala, "Low actuation voltage RF MEMS switch using varying section composite fixed-fixed beam.," *Int. J. Microw. Sci. Technol.*, vol. 2014, pp. 1-12, Sep. 2014.
[45] M. A. Zulkefli et al., "Stress analysis of perforated graphene nano-electro-mechanical (NEM) contact switches by 3D finite element simulation," *Microsyst. Technol.*, vol. 24, no. 2, pp. 1179–1187, Feb. 2018.
[46] W. C. Young, R. G. Budynas, and A. M. Sadegh, *Roark's formulas for stress and strain*. McGraw-Hill Education, 2012.
[47] S. K. Waghmare and D. D. Shah, "RF MEMS Capacitive Shunt Switch: A study based practical overview," *Int. J. Appl. Eng. Res.*, vol. 13, no. 15, pp. 11830–11838, 2018.
[48] D. Connelly and T. J. K. Liu, "Modeling Nanoelectromechanical Switches with Random Surface Roughness," *IEEE Trans. Electron Devices*, vol. 64, no. 5, pp. 2409–2416, Apr. 2017.
[49] T. Singh, "Design and finite element modeling of series-shunt configuration-based RF MEMS switch for high isolation operation in K–Ka band," *J. Comput. Electron.*, vol. 14, no. 1, pp. 167–179, Mar. 2015.
[50] A. Saxena and V. K. Aggarwal "Comparative study of perforated RF MEMS switch," *Procedia Comput. Sci*, vol. 57, pp. 139–145, Jan. 2015.
[51] S. P. Pacheco, L. P. Katehi, and C. C. Nguyen, "Design of low actuation voltage RF MEMS switch," *IEEE MTT-S Int. Microw. Symp. Dig.*, vol. 1, pp. 165–168, June 2000.
[52] K. Guha, M. Kumar, S. Agarwal, and B. Baishya "A modified capacitance model of RF MEMS shunt switch incorporating fringing field effects of perforated beam," *Solid. State. Electron.*, vol. 114, pp. 35–42, Dec. 2015.
[53] T. Hallam, C. F. Moldovan, K. Gajewski, A. M. Ionescu, and G. S. Duesberg, "Large area suspended graphene for nano-mechanical devices," *Phys. status solidi (b),* vol. 252, no. 11, pp. 2429–2432, Nov. 2015.
[54] O. Loh, X. Wei, J. Sullivan, L. E. Ocola, R. Divan, and H. D. Espinosa, "Carbon-carbon contacts for robust nanoelectromechanical switches," *Adv. Mater.*, vol. 24, no. 18, pp. 2463–2468, May 2012.
[55] P. Jhanwar, D. Bansal, S. Pandey, S. Verma, and K. J. Rangra, "Design aspect of high power handling applications: metal contact switches," *Microsyst. Technol.*, vol. 21, no. 10, pp. 2083–2087, Oct. 2014.
[56] K. M. Milaninia, M. A. Baldo, A. Reina, and J. Kong, "All graphene electromechanical switch fabricated by chemical vapor deposition," *Appl. Phys. Lett.*, vol. 95, no. 18, pp. 1–4, Nov. 2009.
[57] Z. Shi et al., "Studies of graphene-based nanoelectromechanical switches," *Nano Res.*, vol. 5, no. 2, pp. 82–87, Feb. 2012.
[58] M. Inagaki and F. Kang, "Graphene derivatives: graphane, fluorographene, graphene oxide, graphyne and graphdiyne," *J. Mater. Chem. A*, vol. 2, no. 33, pp. 13193–13206, June 2014.
[59] K. Krishnamoorthy, M. Veerapandian, K. Yun, and S. J. Kim, "The chemical and structural analysis of graphene oxide with different degrees of oxidation," *Carbon*, vol. 53, pp. 38–49, Mar. 2013.
[60] X. Shen, X. Lin, N. Yousefi, J. Jia, and J. K. Kim, "Wrinkling in graphene sheets and graphene oxide papers," *Carbon*, vol. 66, pp. 84–92, Jan. 2014.
[61] J. Wan, J. W. Jiang, and H. S. Park, "Negative Poisson's ratio in graphene oxide," *Nanoscale*, vol. 9, no. 11, pp. 4007–4012, Feb. 2017.
[62] C. Cao, M. Daly, C. V. Singh, Y. Sun, and T. Filleter, "High strength measurement of monolayer graphene oxide," *Carbon,* vol. 81, no. 1, pp. 497–504, Jan. 2015.
[63] P. Poulin et al., "Superflexibility of graphene oxide," *Proc Natl Acad Sci*, vol. 113, pp. 11088–11093, Oct. 2016.
[64] X. Huang et al., "Graphene-based materials: synthesis, characterization, properties, and

applications," *Small*, vol. 7, pp. 1876–1902, July 2011.

[65] Y. Liu, X. Dong, and P. Chen, "Biological and chemical sensors based on graphene materials," *Chem Soc Rev*, vol. 41, pp. 2283–2307, Dec. 2012.

[66] H. Wang et al., "Graphene-wrapped sulfur particles as a rechargeable lithium–sulfur battery cathode material with high capacity and cycling stability," *Nano Lett*, vol. 11, pp. 2644, July 2011.

[67] S. Wu, Z. Yin, Q. He, X. Huang, X. Zhou, and H. Zhang "Electrochemical deposition of semiconductor oxides on reduced graphene oxide-based flexible, transparent, and conductive electrodes," *J Phys Chem C*, vol. 114, pp. 11816–11821, July 2010.

[68] A. Agresti et al., "Efficiency and stability enhancement in perovskite solar cells by inserting lithium-neutralized graphene oxide as electron transporting layer," *Adv. Funct. Mater.*, vol. 26, no. 16, pp. 2686-2694, Apr. 2016.

[69] M. Zhang, N. Zhou, P. Yuan, Y. Su, M. Shao, and C. Chi, "Graphene oxide and adenosine triphosphate as a source for functionalized carbon dots with applications in pH-triggered drug delivery and cell imaging," *RSC Adv.*, vol. 7, no. 15, pp. 9284-9293, Jan. 2015.

[70] K. M. Kang et al., "Selective Molecular Separation on Ti_3C_2Tx–Graphene Oxide Membranes during Pressure-Driven Filtration: Comparison with Graphene Oxide and MXenes," *ACS Appl. Mater. Interfaces*, vol. 9, no. 51, pp. 44687-44694, Dec. 2017.

[71] X. Tian et al., "Graphene oxide nanosheets retard cellular migration via disruption of actin cytoskeleton," *Small,* vol. 13, no. 3, pp.1602133, Jan. 2017.

[72] L. C. Lin and J. C. Grossman, "Atomistic understandings of reduced graphene oxide as an ultrathin-film nanoporous membrane for separations," *Nat Commun*, vol. 6, pp.1-7, Sep. 2015.

[73] S. P. Surwade et al., "Water desalination using nanoporous single-layer graphene," *Nat Nanotechnol*, vol. 10, p. 459, May 2015.

[74] S. William, J. R. Hummers, and R. E. Offeman, "Preparation of graphitic oxide," *J. Am. Chem. Soc.*, vol. 80, no. 6, pp. 1339–1339, 1958.

[75] C. Y. Su, A. Y. Lu, Y. Xu, F. R. Chen, A. N. Khlobystov, and L. J. Li, "High-quality thin graphene films from fast electrochemical exfoliation.," *ACS Nano*, vol. 5, no. 3, pp. 2332–2339, Mar. 2011.

[76] R. Tarcan, O. Todor-Boer, I. Petrovai, C. Leordean, S. Astilean, and I. Botiz, "Reduced graphene oxide today," *J. Mater. Chem. C*, vol. 8, no. 4, pp. 1198–1224, July 2020.

[77] S. Pei and H. M. Cheng, "The reduction of graphene oxide," *Carbon*, vol. 50, no. 9, pp. 3210–3228, Aug. 2012.

[78] F. Iskandar, U. Hikmah, E. Stavila, and A. H. Aimon, "Microwave-assisted reduction method under nitrogen atmosphere for synthesis and electrical conductivity improvement of reduced graphene oxide (rGO)," *RSC Adv.*, vol. 7, no. 83, pp. 52391–52397, Nov. 2017.

[79] H. K. Jang et al., "Interfacial shear strength of reduced graphene oxide polymer composites," *Carbon*, vol. 77, pp. 390–397, Oct. 2014.

[80] A. Bhaumik and J. Narayan, "Conversion of p to n-type reduced graphene oxide by laser annealing at room temperature and pressure," *J. Appl. Phys.*, vol. 121, no. 12, pp. 125303, Nov. 2017.

[81] K. E. Petersen, "Micromechanical membrane switches on silicon," *IBM J. Res. Dev.*, vol. 23, no. 4, pp. 376–385, July 1979.

[82] J. J. Yao and M. C. Chang, "A surface micromachined miniature switch for telecommunications applications with signal frequencies from DC to 4 GHz," *International Conference on Solid State Sensors and Actuators Digest*, pp. 384–387, Dec. 1995.

[83] C. Goldsmith et al., "Characteristics of micromachined switches," *Microwave frequencies, IEEE MTT-S international microwave symposium digest, IEEE*, pp. 1141–1144, 1996.

[84] C. L. Goldsmith, Z. Yao, S. Eshelman, and D. Denniston, "Performance of low-loss RF MEMS capacitive switches," *IEEE Microw Guid Wave Lett*, vol. 8, no. 8, pp. 269, Aug. 1998.

[85] H. S. Newman, “RF MEMS switches and applications,”*IEEE International Reliability Physics Symposium. Proceedings*, pp. 111–115, 2002.
[86] C. Goldsmith et al., “Lifetime characterization of capacitive RF MEMS switches,” *IEEE MTT-S International Microwave Sympsoium Digest*, pp. 227–230, 2001.
[87] C. Chang and P. Chang, “Innovative micromachined microwave switch with very low insertion loss,” *Sensors Actuators A Phys.*, vol. 79, no. 1, pp. 71–75, Jan. 2000.
[88] B. Schauwecker, K. M. Strohm, W. Simon, J. Mehner, and J. F.Luy, “A new type of high bandwidth RF MEMS switch: toggle switch,” *J. Semicond. Technol. Sci.*, vol. 2, no. 4, pp. 237–245, Dec. 2002.
[89] N. Nishijima, J. J. Hung, and G. M. Rebeiz, “A low-voltage high contact force RF-MEMS switch,” *IEEE MTT-S International Microwave Symposium Digest*, pp. 577–580, 2004.
[90] M. Daneshmand, S. Fouladi, R. R. Mansour, M. Lisi, and T. Stajcer, “Thermally actuated latching RF MEMS switch and its characteristics,” *IEEE Trans. Microw. Theory Tech.*, vol. 57, no. 12, pp. 3229–3238, Nov. 2009.
[91] J. Park, E. S. Shim, W. Choi, Y. Kim, Y. Kwon, and D. I. Cho, “A non-contact-type RF MEMS switch for 24-GHz radar applications,” *J. Microelectromechanical Syst.*, vol. 18, no. 1, pp. 163-173, Jan. 2009.
[92] H. Nawaz, M. U. Masood, M. M. Saleem, J. Iqbal, and M. Zubair, “Surface roughness effects on electromechanical performance of RF-MEMS capacitive switches,” *Microelectron. Reliab.*, vol. 104, pp. 113544, Jan. 2020.
[93] J. B. Rizk, J. B. Muldavin, G. L. Tan, and G. M. Rebeiz, “Design of X-Band MEMS Microstrip Shunt Switches,” *European Microwave Conference*, pp. 1–4, Oct. 2000.
[94] R. G. Polcawich, J. S. Pulskamp, D. Judy, P. Ranade, S. T. McKinstry, and M. Dubey, “Surface micromachined microelectromechancial ohmic series switch using thin-film piezoelectric actuators,” *IEEE Trans. Microw. Theory Tech.*, vol. 55, pp. 2642–2654, Dec. 2007.
[95] M. Hoffmann et al., “Theoretical calculations and performance results of a PZT thin film actuator,” *IEEE Trans. Ultrason. Ferroelectr. Freq. Control*, vol. 50, pp. 1440–1446, Nov. 2003.
[96] H. A. Tilmans et al., “A fully-packaged electromagnetic microrelay,” *Int. Conf. Micrco Electr. Mech. Syst.*, pp. 25–30, Jan. 1999.
[97] Y. Wang, Z. Li, D.T. McCormick, and N. C. Tien, “A low-voltage lateral MEMS switch with high RF performance,” *J. MEMS*, vol. 13, no. 6, pp. 902–911, Dec. 2004.
[98] H. C. Lee, J. H. Park, and Y. H. Park, “Development of shunt type ohmic RF MEMS switches actuated by piezoelectric cantilever,” *Sensors and Actuators*, vol. 136, pp. 282–290, May 2007.
[99] J. B. Muldavin and G. M. Rebeiz, “30 GHz tuned MEMS switches,” *IEEE Microwave Theory and Techniques Symposium*, pp. 1511–1514, 1999.
[100] S. P. Pacheco, L. P. Katehi, and C. C. Nguyen, “Design of low actuation voltage RF MEMS switch,” *Microwave symposium digest,IEEE,* pp. 165–168, 2000.
[101] D. Peroulis, S. P. Pacheco, K. Sarabandi, and L. P. Katehi, “Electromechanical considerations in developing low-voltage RF MEMS switches,” *IEEE Trans. Microw Theory Tech*, vol. 51, no. 1, pp. 259–270, Jan. 2003.
[102] H. Jaafar, F. L. Nan, and N. A. M. Yunus, “Design and simulation of high performance RF MEMS series switch,” *IEEE Regional Symposium on Micro and Nano Electronics, IEEE*, pp. 349–353, 2011.
[103] D. Balaraman, S.K. Bhattacharya, F. Ayazi, and J. Papapolymerou, “Low-Cost low actuation voltage copper RF MEMS Switches,” *IEEE Microw. Theory Tech. Symp.*, vol. 2, pp. 1225–1228, June 2002.
[104] F. M. Guo et al., “Study on low voltage actuated RF MEMS capacitive switches,” *Sensors Actuators A Phys.*, vol. 108, no. 1–3, pp. 128–133, Nov. 2003.
[105] S. D. Lee, B. C. Jun, S. D. Kim, H. C. Park, J. K. Rhee, and K. Mizuno, “An RF-MEMS switch with low-actuation voltage and high reliability,” *J. Microelectromechanical Syst.*, vol. 15, pp.

1605-1611, Dec. 2006.

[106] J. Kim et al., "A stiff and flat membrane operated dc contact type RF MEMS switch with low actuation voltage," *Sensors and Actuators*, vol. 153, pp. 114–119, June 2009.

[107] A. Kundu, S. Sethi, N.C. Mondal, B. Gupta, S.K. Lahiri, and H. Saha, "Analysis and optimization of two movable plates RF MEMS switch for simultaneous improvement in actuation voltage and switching time," *Microelectronics J.*, vol. 41, pp. 257–265, May 2010.

[108] J. Y. Park, G. H. Kim, K. W. Chung, and J. U. Bu, "Monolithically integrated micromachined RF MEMS capacitive switches," *Sensors Actuators A Phys.*, vol. 89, no. 1–2, pp. 88–94, Mar. 2001.

[109] S. C. Shen, Caruth D, and M. Feng, "Broadband low actuation voltage RF MEMS switches," *IEEE GaAs IC symposium, IEEE*, pp. 161–164, 2000.

[110] K. Segueni et al., "A totally free flexible membrane for low voltage MEMS metal contact switch," *2nd European microwave integrated circuits conference*, pp. 355–358, Oct. 2007.

[111] K. G. Sravani and K. S. Rao, "Analysis of RF MEMS shunt capacitive switch with uniform and non-uniform meanders," *Microsyst. Technol.*, vol. 24, no. 2, pp. 1309–1315, Feb. 2018.

[112] K. G. Sravani, K. Guha, and K. S. Rao, "Design of a novel step structure RF MEMS switch for K-band applications," *Microsyst. Technol.*, pp. 1–9, July 2020.

[113] K. S. Rao et al., "Design, modeling and analysis of perforated RF MEMS capacitive shunt switch," *IEEE Access*, vol. 7, pp. 74869–74878, May 2019.

[114] R. Chan, R. Lesnick, D. Becher, and M. Feng, "Low-Actuation Voltage RF MEMS Shunt Switch With Cold Switching Lifetime of Seven Billion Cycles," *Journal of Microelectromechanical Systems,* vol. 12, no. 5, pp. 713–719, Oct. 2003.

[115] T. Kageyama, K. Shinozaki, L. Zhang, J. Lu, H. Takaki, and S. S. Lee, "Fabrication of an Au–Au/carbon nanotube-composite contacts RF-MEMS switch," *Micro Nano Syst. Lett.*, vol. 6, no. 1, pp. 1–8, Dec. 2018.

[116] H. R. Ansari and S. Khosroabadi, "Design and simulation of a novel RF MEMS shunt capacitive switch with a unique spring for Ka-band application," *Microsyst. Technol.*, vol. 25, no. 2, pp. 531–540, Feb. 2019.

[117] A. Attaran and R. Rashidzadeh, "Ultra low actuation voltage RF MEMS switch," *Micro Nano Syst. Lett.*, vol. 3, no. 1, pp. 7, Dec. 2015.

[118] M. Angira and D. Bansal, "Realization of a capacitive shunt RF-MEMS switch using straight flexure based non-uniform bridge structure-fabrication and characterization," *Microsyst. Technol.*, pp. 1–6, July 2020.

[119] Y. Zhang, G. Ding, H. Wang, S. Fu, and B. Cai, "Low-stress permalloy for magnetic MEMS switches," *IEEE Trans Magn*, vol. 42, no. 1, pp. 51–55, Dec. 2006.

[120] C. F. Herrmann et al., "Alternative dielectric films for RF MEMS capacitive switches deposited using atomic layer deposited Al_2O_3/ZnO alloys," *Sens Actuators A*, vol. 135, no. 1, pp. 262–272, Mar. 2007.

[121] J. Tsaur et al., "Broadband MEMS shunt switches using PZT/HfO_2 multi-layered high k dielectrics for high switching isolation," *Sens Actuators A*, vol. 121, no. 1, pp. 275–281, May 2005.

[122] Y. K. Yoon, E. Chen, M. G. Allen, and J. Laskar, "Embedded solenoid inductors for RF CMOS power amplifiers," *Transducers' 01 Eurosensors XV*, pp. 1086–1089, 2001.

[123] A. Persano, A. Cola, G. De Angelis, A. Taurino, P. Siciliano, and F. Quaranta, "Capacitive RF MEMS switches with tantalum-based materials," *Journal microelectromechanical Syst.*, vol. 20, no. 2, pp. 365–370, Feb. 2011.

[124] M. K. Bonthu and A. K. Sharma, "An investigation of dielectric material selection of RF-MEMS switches using Ashby's methodology for RF applications," *Microsyst. Technol.*, vol. 24, no. 4, pp. 1803–1809, Apr. 2018.

[125] K. Guha, M. Kumar, A. Parmar, and S. Baishya, "Performance analysis of RF MEMS capacitive

switch with non uniform meandering technique," *Microsyst. Technol.*, vol. 22, no. 11, pp. 2633–2640, Nov. 2016.

[126] M. Angira, "High performance capacitive RF-MEMS switch based on HfO2 dielectric," *Trans. Electr. Electron. Mater.*, vol. 20, no.1, pp. 52–59, Feb. 2019.

[127] T. L. Narayana, K. G. Sravani, and K. S. Rao, "Design and analysis of CPW based shunt capacitive RF MEMS switch," *Cogent Eng.*, vol. 4, no. 1, pp. 1363356, Jan. 2017.

[128] C. L. Dai, H. J. Peng, M. C. Liu, C. C. Wu, and L. J. Yang, "Design and fabrication of RF MEMS switch by the CMOS process," *Tamkang J Sci Eng*, vol. 8, no. 3, pp. 197–202, Sep. 2005.

[129] C. I. Lee, C. H. Co, and T. C. Huang, "A novel multi-actuation CMOS RF MEMS switch," *Smart Struct. Devices, Syst. IV*, vol. 7268, pp. 726804, Dec. 2008.

[130] M. Kaynak et al., "Characterization of an embedded RF-MEMS switch," *Topical Meeting on Silicon Monolithic Integrated Circuits in RF Systems IEEE*, pp. 144–147, 2010.

[131] D. Bansal, A. Kumar, A. Sharma, P. Kumar, and K. J. Rangra, "Design of novel compact anti-stiction and low insertion loss RF MEMS switch," *Microsyst. Technol.*, vol. 20, no. 2, pp. 337–340, Feb. 2014.

[132] A. Persano, F. Quaranta, M. C. Martucci, P. Siciliano, and A. Cola, "On the electrostatic actuation of capacitive RF MEMS switches on GaAs substrate," *Sensors Actuators A Phys.*, vol. 232, pp. 202–207, Aug. 2015.

[133] K. Mehta, D. Bansal, A. Bajpai, P. Kumar, A. Kumar, and K. J. Rangra, "Improved isolation RF MEMS switch with post release ashing," *Microsyst. Technol.*, vol. 24, no. 9, pp. 3863-3866., Sep. 2018.

[134] L. N. Thalluri et al., "Perforated serpentine membrane with AlN as dielectric material shunt capacitive RF MEMS switch fabrication and characterization," *Microsyst. Technol.*, vol. 26, no. 6, pp. 1–13, June 2020.

[135] A. Stehle et al., "High-power handling capability of low complexity RF-MEMS switch in Ku-band," *Electron. Lett.*, vol. 43, no. 24, pp. 1367–1368, Dec. 2007.

[136] T. M. Vu, G. Prigent, J. Ruan, and R. Plana, "Design and fabrication of RF-MEMS switch for V-band reconfigurable application," *Prog. Electromagn. Res.*, vol. 39, pp. 301–318, Mar. 2012.

[137] P. Jhanwar, D. Bansal, S. Pandey, S. Verma, and K. J. Rangra, "Design aspect of high power handling applications: metal contact switches," *Microsyst. Technol.*, vol. 21, no. 10, pp. 2083–2087, Oct. 2015.

[138] F. Quaranta et al., "Tailoring design and fabrication of capacitive RF MEMS switches for K-band applications," *Smart Sensors, Actuators, MEMS VII; Cyber Phys. Syst.*, vol. 9517, pp. 95170S, May 2015.

[139] E. A. Savin, K. A. Chadin, and R. V. Kirtaev, "Design and manufacturing of X-band RF MEMS switches," *Microsyst. Technol.*, vol. 24, no. 6, pp. 2783–2788, June 2018.

[140] M. B. Subramanian, C. Joshitha, B. S. Sreeja, and P. Nair, "Multiport RF MEMS switch for satellite payload applications.," *Microsyst. Technol.*, vol. 24, no. 5, pp. 2379–2387, May 2018.

[141] C. Chu, X. Liao, and H. Yan, "Ka-band RF MEMS capacitive switch with low loss, high isolation, long-term reliability and high power handling based on GaAs MMIC technology," *IET Microwaves, Antennas Propag.*, vol. 11, no. 6, pp. 942–948, Jan. 2017.

[142] S. M. Kim et al., "Suspended few-layer graphene beam electromechanical switch with abrupt on-off characteristics and minimal leakage current," *Appl. Phys. Lett.*, vol. 99, no. 2, pp. 023103, July 2011.

[143] Y. Mafinejad, M. Zarghami, A. Z. Kouzani, and K. Mafinezhad, "Impact of carbon material on RF MEMS switch," *Iranian Conference on Electrical Engineering IEEE*, pp. 1–4, May 2013.

[144] P. Li, G. Jing, B. Zhang, S. Sando, and T. Cui, "Single-crystalline monolayer and multilayer graphene nano switches," *Appl. Phys. Lett.*, vol. 104, no. 11, pp. 113110, Mar. 2014.

[145] P. Li, and T. Cui, "RF nano switch based on single crystalline graphene," *International Conference on Solid-State Sensors, Actuators and Microsystems , IEEE*, pp. 307–310, June 2015.

[146] C. F. Moldovan, W. A. Vitale, P. Sharma, L.S. Bernard, and A. M. Ionescu, “Fabrication process and characterization of suspended graphene membranes for RF NEMS capacitive switches,” *Microelectron. Eng.*, vol. 145, pp. 5–8, Sep. 2015.

[147] M. A. Zulkefli, M. A. Mohamed, K. S. Siow, and B. Y. Majlis, “Optimization of beam length and air gap of suspended graphene NEMS switch for low pull-in voltage application,” *IEEE International Conference on Semiconductor Electronics*, pp. 29–32, Aug. 2016.

[148] M. A. Zulkefli et al., “Three-dimensional finite element method simulation of perforated graphene nano-electro-mechanical (NEM) switches,” *Micromachines*, vol. 8, no. 8, pp. 1–16, Aug. 2017.

[149] A. Anjum, M. Madhewar, S. S. Mohite, and V. B. Sawant, “Graphene/MoS_2 Based RF-NEMS Switches for Low Actuation Voltage and Enhanced RF-Performance,” *9th International Conference on Computing, Communication and Networking Technologies IEEE*, pp. 1–7, July 2018.

[150] J. B. Ma, L. Jiang, and S. F. Asokanthan, “Influence of surface effects on the pull-in instability of NEMS electrostatic switches,” *Nanotechnology*, vol. 21, pp. 505708, Nov. 2013.

[151] Z. Zhang, M. Kamon, and L. Daniel, “Continuation-based pull-in and lift-off simulation algorithms for microelectromechanical devices,” *J. Microelectromechanical Syst.*, vol. 23, no. 5, pp. 1084–1093, Feb. 2014.

[152] W. B. Zimmerman, “Multiphysics modeling with finite element methods.,” *World Sci. Publ. Company.*, vol. 18, 2006.

[153] D. W. Pepper, and J. C. Heinrich, “The finite element method: basic concepts and applications with MATLAB, MAPLE, and COMSOL,” *CRC Press*, 2017.

[154] COMSOL MULTIPHYSICS 3.4 *AC/DC Module User‘s Guide*. COMSOL AB, 2007.

[155] L. Lin, H. Wu, S. J. Green, J. Crompton, S. Zhang, and D. W. Horsell, “Formation of tunable graphene oxide coating with high adhesion,” *Phys. Chem. Chem. Phys.*, vol. 18, no. 7, pp. 5086–5090, Jan. 2016.

[156] J. Liu, D. Galpaya, M. Notarianni, C. Yan, and N. Motta, “Graphene-based thin film supercapacitor with graphene oxide as dielectric spacer,” *Appl. Phys. Lett.*, vol. 103, no. 6, pp. 063108, Aug. 2013.

[157] A. Persano, J. Iannacci, P. Siciliano P, and F. Quaranta, “Out-of-plane deformation and pull-in voltage of cantilevers with residual stress gradient: Experiment and modelling.,” *Microsyst. Technol.*, vol. 25, no. 9, pp. 3581–3588, Sep. 2019.

[158] L. X. Zhang and Y. P. Zhao, “Electromechanical model of RF MEMS switches,” *Microsyst. Technol.*, vol. 9, no. 6–7, pp. 420–426, Sep. 2003.

[159] P. Li, Z. You, G. Haugstad, and T. Cui, “Graphene fixed-end beam arrays based on mechanical exfoliation,” *Appl. Phys. Lett.*, vol. 98, no. 25, pp. 2011–2014, June 2011.

[160] D. Lee, T. Osabe, and T. J. K. Liu, “Scaling limitations for flexural beams used in electromechanical devices,” *IEEE Trans. Electron Devices*, vol. 56, no. 4, pp. 688–691, Feb. 2009.

[161] Y.Qain, L. Lou, M. J. Tsai, and C. Lee, “A dual-silicon-nanowires based U-shape nanoelectromechanical switch with low pull-in voltage,” *Appl. Phys. Lett.*, vol. 100, no. 11, pp. 113-102, Mar. 2012.

[162] B. Liu et al., “From graphite to graphene oxide and graphene oxide quantum dots,” *Small*, vol. 13, no. 18, pp. 1601001, May 2017.

[163] K. Srinivasa Rao, K. Vasantha, and K. Girija Sravani, “Design and performance analysis of hybrid SPDT RF MEMS switch,” *Microsystem Technologies*, vol. 26, pp.1-8, May 2020.

[164] M. Tang et al., “An approach of lateral RF MEMS switch for high performance,” *Symposium on Design, Test, Integration and Packaging of MEMS/MOEMS*, pp. 99–102, 2003.

[165] C. D. Reddy, S. Rajendran, and K. M Liew, “Equilibrium configuration and continuum elastic properties of finite sized graphene,” *Nanotechnology*, vol. 17, no. 3, pp. 864, Jan. 2006.

[166] G. Cao, "Atomistic studies of mechanical properties of graphene," *Polymers*, vol. 6, no. 9, pp. 2404–2432, Sept. 2014.

[167] I. E. Lysenko, A. V. Tkachenko, E. V. Sherova and A. V. Nikitin, "Analytical approach in the development of RF MEMS switches," *Electronics*, vol. 7, no. 12, pp. 415, Dec. 2018.

[168] S. Shekhar, K. J. Vinoy, and G. K. Ananthasuresh, "Switching and release time analysis of electrostatically actuated capacitive RF MEMS switches," *Sensors & Transducers*, vol. 130, no. 7, pp. 77, July 2011.

[169] M. Dequesnes, Z. Tang and N. R. Aluru, "Static and dynamic analysis of carbon nanotube-based switches," *J. Eng. Mater. Technol.*, vol. 126, pp. 230–237, June 2004.

[170] J. Kulothungan , M. Muruganathan and H. Mizuta "3D finite element simulation of graphene nano-electro-mechanical switches," *Micromachines*, vol. 7, no. 8, pp. 143, Aug. 2016.

[171] V. M. Reddy , "Design and analysis of microcantilevers with various shapes using comsol multiphysics software," *Int. J. Emerg. Technol. Adv. Eng.*, vol. 3, no. 3, Mar. 2013.

[172] J. Sun , M. Muruganathan, N. Kanetake and H. Mizuta , "Locally-actuated graphene-based nano-electro-mechanical switch," *Micromachines*, vol. 7, no. 7, pp. 124, July 2016.

[173] A. Peschot, C. Qian, and T. K. Liu, "Nanoelectromechanical switches for low-power digital computing," *Micromachines*, vol. 6, no. 8, pp. 1046–1065, Aug. 2015.

[174] P. Pandiyan, G. Uma, and M. Umapathy, "Design and simulation of electrostatic NEMS logic gates," *COMPEL-The Int. J. Comput. Math. Electr. Electron. Eng.*, vol. 37, no. 1, pp. 2–28, Jan. 2018.

[175] H. F. Dadgour, M. M. Hussain, and K. Banerjee, "A new paradigm in the design of energy-efficient digital circuits using laterally-actuated double-gate NEMS," *ACM/IEEE International Symposium on Low-Power Electronics and Design IEEE*, pp. 7–12, 2010.

[176] P. Pai and M. Azar "Microplasma logic gates," *IEEE Trans. Plasma Sci.*, vol. 42, no. 8, pp. 1995–1998, July 2014.

[177] N. Sinha ,T. S. Jones , Z. Guo and G. Piazza, "Body-biased complementary logic implemented using AlN piezoelectric MEMS switches," *J. Microelectromechanical Syst.*, vol. 21, no. 2, pp. 484–496, Jan. 2012.

[178] A. Seyedi, V. Karakostas , S. Cosemans, A. Cristal, M. Nemirovsky, and O. Unsal, "NEMsCAM: a novel CAM Cell based on Nano-electro-mechanical switch and CMOS for energy efficient TLBs," *Proceedings IEEE/ACM International Symposium on Nanoscale Architectures*, pp. 51–56, 2015.

[179] A. Politano, "Spectroscopic investigations of phonons in epitaxial graphene," *Crit. Rev. Solid State Mater. Sci.*, vol. 42, pp. 99–128, Mar. 2016.

[180] D. Garcia-Sanchez, A. M. Zande, A. S. Paulo, B. Lassagne, P. L. McEuen, and A. Bachtold, "Imaging mechanical vibrations in suspended graphene sheets," *Nano Lett.*, vol. 8, pp. 1399, Apr. 2008.

[181] Y. Zhou, H. Bi, X. Xie, and L. Sun, "Fabrication of graphene based electrothermal cantilever actuator," *International Conference on Nano/Micro Engineered and Molecular Systems IEEE*, pp. 911–914, July 2013.

[182] P. Li , Z. You, and T. Cui, "Graphene cantilever beams for nano switches," *Appl. Phys. Lett.*, vol. 101, no. 9, pp. 093111, July 2012.

[183] M. Orlita, C. Faugeras, P. Plochocka, P. Neugebauer, G. Martinez, and D. K. Maude, "Approaching the dirac point in highmobility multilayer epitaxial graphene," *Phys Rev Lett*, vol. 101, no. 26, pp. 267601, Dec. 2008.

[184] L. Jasulaneca, J. Kosmaca, R. Meija, J. Andzane, and D. Erts, "Electrostatically actuated nanobeam-based nanoelectromechanical switches–materials solutions and operational conditions," *Beilstein J. Nanotechnol.*, vol. 9, pp. 271–300, Jan. 2018.

List of Publications:

Published:

[1] Rekha Chaudhary, Prasantha R. Mudimela (2020) “3D Modelling of Graphene Oxide Based Nanoelectromechanical Capacitive Switch” Microsystem Technologies, vol. 26, pp. 2931-2937.

[2] Prasantha R. Mudimela, Rekha Chaudhary (2020) “Graphene based digital logic gates”, Journal of Computational Electronics, pp.1-7. https://doi.org/10.1007/s10825-020-01545-y.

[3] Rekha Chaudhary, Prasantha R. Mudimela (2020) “Pull-in response and Eigen frequency analysis of Graphene oxide-based NEMS switch” Materials Today: Proceedings, vol. 28, pp. 196-200.

[4] Rekha Chaudhary, Prasantha R. Mudimela, “Electrostatically Actuated Graphene NEMS Switch with Different Bridge Structures” ICICS-2020, (Accepted).

[5] Rekha Chaudhary, Prachi Jhanwar, Prasantha R. Mudimela (2020) “Finite Element Analysis of Graphene Oxide Hinge Structure-based RF NEM Switch” IETE Journal of Research.doi.org/10.1080/03772063.2020.1844078.

Communicated:

[6] Rekha Chaudhary, Prasantha R. Mudimela, “Comprehensive Study RF Analysis of G/GO based NEMS Shunt Switch” (Under review).

[7] Rekha Chaudhary, Prasantha R. Mudimela, “Performance Analysis of NEMS switch using Graphene Derivative based Composite Beam” (Under review).